



8-2000

High resolution photonic analysis with scanned probes

Andrew G. Wig

Follow this and additional works at: https://trace.tennessee.edu/utk_graddiss

Recommended Citation

Wig, Andrew G., "High resolution photonic analysis with scanned probes. " PhD diss., University of Tennessee, 2000.
https://trace.tennessee.edu/utk_graddiss/8439

This Dissertation is brought to you for free and open access by the Graduate School at TRACE: Tennessee Research and Creative Exchange. It has been accepted for inclusion in Doctoral Dissertations by an authorized administrator of TRACE: Tennessee Research and Creative Exchange. For more information, please contact trace@utk.edu.

To the Graduate Council:

I am submitting herewith a dissertation written by Andrew G. Wig entitled "High resolution photonic analysis with scanned probes." I have examined the final electronic copy of this dissertation for form and content and recommend that it be accepted in partial fulfillment of the requirements for the degree of Doctor of Philosophy, with a major in Physics.

Thomas L. Ferrell, Major Professor

We have read this dissertation and recommend its acceptance:

Robert Compton, Marianne Breinig, Thomas Callcott

Accepted for the Council:

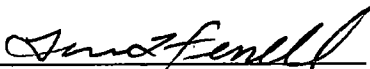
Carolyn R. Hodges

Vice Provost and Dean of the Graduate School

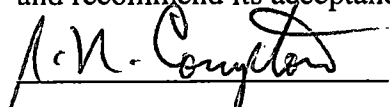


(Original signatures are on file with official student records.)

To the Graduate Council:

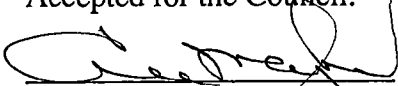
I am submitting herewith a dissertation written by Andrew Gustaf Wig entitled "High Resolution Photonic Analysis with Scanned Probes". I have examined the final copy of this dissertation for form and content and recommend that it be accepted in partial fulfillment of the requirements for the degree of Doctor of Philosophy, with a major in Physics.


Thomas L. Ferrell, Major Professor

We have read this dissertation
and recommend its acceptance:

Accepted for the Council:


Interim Vice Provost and
Dean of The Graduate School

High Resolution Photonic Analysis with Scanned Probes

A Dissertation
Presented for the
Doctor of Philosophy
Degree
The University of Tennessee, Knoxville

Andrew Gustaf Wig
August 2000

Copyright © Andrew Gustaf Wig, 2000
All rights reserved

To Nancy
for
whom my love and appreciation
grows deeper every day.

Acknowledgments

I would like to thank my research advisor, Dr. Tom Ferrell, for his help and guidance throughout my dissertation endeavor. I would also like to express my thanks to Dr. Marianne Breinig, Dr. Thomas Callcott, and Dr. Robert Compton for taking the time to serve on my committee. Furthermore, I would like to thank Dr. Ed Arakawa, Dr. Bruce Warmack, Dr. Fabrice Meriaudeau, and Todd Downing.

Special thanks goes to David Hedden for his mastery of all things electronic and to Dr. Ali Passian for his constant optimism, intellectual discussions, and his inspiring "word of the day".

Lastly, an enormous debt of gratitude and appreciation goes to my beautiful and lovely wife without whose support and extreme patience this endeavor could not have been completed.

Abstract

Absorption spectroscopy is demonstrated to be feasible using a photon scanning tunneling microscope (PSTM) combined with a spectroscope. Methods of improving the spatial resolution and spectroscopic capabilities are studied in order to determine their potential practicability. Analysis of the photon scanning tunneling microscope (PSTM) and modifications made to the microscope are included with experimental results demonstrating certain image and spectral resolution capabilities. Results showing both the PSTM absorption spectra of gold island films and their independently acquired PSTM images are presented. An alternative scanning probe method involving photons is additionally examined. The new method is demonstrated to require specific improvements in order that it might provide a distinct improvement in resolution. The new type of scanning probe microscope is one utilizing nonlinear photonics: the nonlinear scanning tunneling microscope (NSTM). Basic results are described and two-photon fluorescence measurements are presented to demonstrate the principle of operation. In any scanned probe microscope or spectroscope, resolution is strongly dependent upon the characteristics of the signal as a function of distance to the sample and knowledge of these characteristics. The NSTM functionality is most dependent upon the sample-probe gap, but the gap also determines resolution in the PSTM. Hence measurements and calculations showing an analysis of the characteristics of the separation between the probe and sample surface are also presented.

Table of Contents

Chapter 1	Introduction	1
1.1	Background	1
1.1.1	Origins of Microscopy and Optical Microscopes.....	1
1.1.2	Recent Forms of Classical Microscopy	2
1.1.3	Electron Microscopy.....	3
1.2	Scanning Probes	4
1.2.1	Origins	4
1.2.2	Resolution	5
1.2.3	Types of SPMs	6
1.3	The PSTM Concept.....	9
1.3.1	Basic Operating Concept	9
1.3.2	PSTM Resolution	14
1.3.3	PSTM Spectroscopy	15
1.3.4	Samples for the PSTM in the Present Work	15
1.3.4.1	Metal Island Films	15
1.3.4.2	Fluorophores.....	16
1.4	The Nonlinear Tunneling Microscope (NSTM)	17
1.4.1	Motivation.....	17
1.4.2	Operational Principle of the Nonlinear Scanning Probe Microscope (NSPM).....	18
1.4.3	Introduction of Distance to Surface.....	20
1.5	Scope of Present Research.....	21
Chapter 2	Theory	23
2.1	Photon Scanning Tunneling Microscope (PSTM)	23
2.1.1	Reflection and Transmission.....	25
2.1.2	Frustrated TIR	32
2.1.3	Truncated Cone Approximation.....	37

2.2	Absorbance for Gold Islands	42
2.2.1	Oblate Spheroid Theory	42
2.2.2	Gaussian Distribution of Particles	52
2.3	NSPM (Nonlinear Scanning Probe Microscope)	54
2.3.1	Interaction of Light with Molecules.	55
2.3.2	Fluorophores	56
2.3.3	Two-Photon Excitation	56
2.4	Distance to Surface Calculations	62
2.4.1	Calculation for General Function.	62
2.4.2	Theoretical Predictions of Distance to Surface	63
2.4.3	Paraboloidal Probe Approximation	71
2.5	Probe Measures the Electro-Magnetic Cross Section.	75
2.5.1	Summary of Theory	76
Chapter 3	Experimental Description	77
3.1	Probe Positioning	77
3.1.1	Piezoelectric Scanner Construction	79
3.2	Microscope	84
3.2.1	Stand and Scan Head	84
3.2.2	Nanoscope Controller	84
3.3	Signal Detection/Analysis	88
3.3.1	Probe Creation	88
3.3.2	Spectrometer	92
3.3.3	PMT and Diode Array	92
3.4	Illumination	95
3.4.1	Rotational Mirror Assembly	95
3.4.2	Lasers	95
3.4.3	Standard Imaging Setup	98
3.4.4	Two-Photon Light Delivery	100
3.4.4.1	Power Meter Conversion for Two-Photon System	100

3.4.5	White Light Source and Delivery System	103
3.5	Sample Preparation and Characterization.....	104
3.5.1	Sample Cleaning.....	104
3.5.2	Vacuum evaporation process	105
3.5.3	Description of the Shimadzu® (model UV-250).....	105
3.5.4	Spectrometer Set up for Fluorescent Measurements	106
Chapter 4	Results.....	107
4.1	Imaging with the PSTM	107
4.2	Imaging of Metal Island Films.....	109
4.2.1	Gold Islands ---Experiments	110
4.2.1.1	Gold Islands on Mica	110
4.2.1.2	Gold islands on Quartz.....	120
4.3	Spectroscopy of Gold Islands	131
4.3.1	Spectroscopy of Gold Islands on Mica	131
4.3.1.1	Gold Islands on Mica Data Set "A"	133
4.3.1.2	Gold Islands on Mica Data Set B	139
4.3.2	Spectroscopy of Gold Islands on Quartz	147
4.4	Two-Photon Excitation Experiment.....	151
4.4.1	Characterization of Yellow Dye.....	151
4.4.2	Two-Photon Data Sets	155
4.5	Distance to Surface.....	167
Chapter 5	Conclusions and Future Possibilities	170
5.1	Conclusions.....	170
5.2	Future Possibilities	171
5.3	Discussion of Technologies	172

Works Consulted	173
Reference	174
Bibliography	178
Appendices	181
Appendix: A. Components of the Piezoelectric Scanning Tube	182
Appendix: B. Mechanical structures	185
Appendix: C. Scattering of TIR light experiment	188
Appendix: D. Images obtained with the PSTM.....	191
Appendix: E. Images of Gold Islands using plasmon field.	195
Vita.....	197

List of Figures

Figure 1.1: Process of tunneling from an optically coupled surface.	12
Figure 2.1: Light under TIR is frustrated by the introduction of a fiber probe into the evanescent field.	24
Figure 2.2: Refraction of light according to Snell's law.	26
Figure 2.3: Illustration of the critical angle in TIR.....	27
Figure 2.4: Evanescent field intensity as a function of distance to surface for different angles of incidence.	29
Figure 2.5: The evanescent field intensity for as a function of distance to the to surface for different wavelengths.	30
Figure 2.6: Illustration of the transmission across an air gap for planer surfaces of two identical materials.....	33
Figure 2.7: Transmission for a plane-air-plane interface for different angles of incidence	35
Figure 2.8: Transmission in the plane-air-plane interface for different wavelengths of light.	36
Figure 2.9: Diagram of the steps and areas used to calculate transmission for the truncated cone approximation.	38
Figure 2.10: Transmission vs. distance for the stepping approximation of a truncated cone above a planner surface.	39
Figure 2.11: Percent signal transmission as a function of the radius of the tip for the plane-air-truncated cone approximation.	41
Figure 2.12: Shape of gold islands on a substrate.	43
Figure 2.13: Absorption modes for gold particles along the minor and major axis. ...	46
Figure 2.14: The scattering cross sections for two particles embedded in a dielectric with a major axis length of 30 nm for light incident at an angle of 50°.	50

Figure 2.15: The total cross section for different wavelength of s-polarized light is given as a function of the shape parameter η	51
Figure 2.16: Absorption peak for a "Gaussian" distribution of gold island particles embedded in a dielectric.	53
Figure 2.17: Diagram of the excitation of an electron from a ground state to an excited state for one-photon and two-photon absorption.	58
Figure 2.18: Example of the field enhancement due to a sharpened metal probe tip.	61
Figure 2.19: Distance to the surface calculation results that are based on unnormalized theoretically generated data sets for 633 nm and 544 nm.	64
Figure 2.20: Distance to the surface calculation results that are based on normalized theoretically generated data sets for 633 nm and 544 nm. ..	65
Figure 2.21: Distance to the surface calculation results that are based on unnormalized theoretically generated data sets for 630 nm and 620 nm.	67
Figure 2.22: The percent difference between the actual distance from the surface and the approximated value for the 633 nm and 544nm case and the 630nm and 620 nm case.	68
Figure 2.23: Distance to the surface calculation results that are based on data normalized at a point below the maximum for 633 nm and 544 nm. ...	69
Figure 2.24: Distance to the surface calculation results that are based on data with a constant scatter term added normalized for 633 nm and 544 nm.	70
Figure 2.25: Distance to the surface calculation results that are based on data with a constant scatter term added normalized at a point below the maximum for 633 nm and 544 nm.	72
Figure 3.1: Data acquisition system for the PSTM.....	78
Figure 3.2: Diagram of the x-y piezoelectric scan tube as it flexes.....	81
Figure 3.3: Diagram of the piezoelectric scanner.....	83

Figure 3.4: Picture of the stand with rotating mirror assembly.....	85
Figure 3.5: Rotational mirror assembly, stand, and scan head.....	86
Figure 3.6: An example of a typical raster scan pattern used in the imaging of the surface of a sample with a SPM.....	89
Figure 3.7: Picture of the P-2000 CO ₂ laser based tip puller.	90
Figure 3.8: SEM Picture of a pulled fiber tip coated with 6nm of gold and palladium.	91
Figure 3.9: Grating parameters for the Jobin Yvon® CP200.....	93
Figure 3.10: Schematic of ISA Jobin Yvon® CP 200 Spectrometer used in gold island spectroscopy experiment.	94
Figure 3.11: Schematic of HR-640 monochromator used for the two-photon experiment.	94
Figure 3.12: Spectrum of HG pen lamp placed in front of the CP- 200 spectrometer.....	96
Figure 3.13: Rotational arm for mirror assembly.....	97
Figure 3.14: Diagram of the piezoelectric drive which rotates the mirror assembly as it is attached to the base.....	97
Figure 3.15: Schematic of the light delivery system for standard imaging purposes...99	
Figure 3.16: Schematic of the light delivery system for two-photon excitation purposes.....	101
Figure 4.1: A 550 nm image of gold islands on mica under s-polarization with a 632.8 laser incident at 50°.....	111
Figure 4.2: A 1.25 μm scan of gold islands on mica under s-polarization with a 632.8 laser incident at 50°.....	112
Figure 4.3: A 1.2 μm scan of gold islands on mica under s-polarization with a 632.8 laser incident at 50°.....	113
Figure 4.4: A 3 μm scan of gold islands on mica under s-polarization with a 632.8 nmlaser incident at 50°.....	114

Figure 4.5: A 1.5 μm PSTM image of clean mica.....	115
Figure 4.6: An 2.5 μm AFM image of gold islands on mica of 4.1 nm of gold heat-treated for 3 minutes @ 150° C.....	116
Figure 4.7: A 3-D 0.4 μm AFM image of gold islands on mica of 4.1 nm of gold heat-treated for 3 minutes @ 150° C.....	117
Figure 4.8: An 0.42 μm AFM image of gold islands on mica of 4.1 nm of gold heat-treated for 3 minutes @ 150° C.....	118
Figure 4.9: An 1.0 μm AFM image of gold islands on mica.	119
Figure 4.10: A 1.1 μm PSTM image of gold islands on a quartz substrate under s polarization with a 632.8 laser at 50° angle of incidence.	121
Figure 4.11: A 5.5 μm PSTM image of gold islands on a quartz substrate under s- polarization with a 632.8 nm laser at a 50° angle of incidence.....	122
Figure 4.12: PSTM image of gold islands on quartz as imaged with a 544 nm laser and 440 nm laser.	123
Figure 4.13: PSTM image made with a 544 nm laser in current mode and height mode.	125
Figure 4.14: PSTM image of gold islands with a 440 nm laser in constant current mode and constant height mode.....	126
Figure 4.15: A 0.9 μm PSTM image of gold islands on quartz with a 440 nm laser in height mode.	127
Figure 4.16: A 1.0 μm PSTM image of gold islands on quartz with a 440 nm laser in current mode.	128
Figure 4.17: A SEM image at 30K magnification of gold islands on a quartz substrate annealed for 4 minutes @ 800° C.....	129
Figure 4.18: An AFM tapping mode image of gold particles on quartz 4.6 nm heated for 6 minutes @ 800° C.	130
Figure 4.19: Absorption data for gold islands on Quartz and on Mica.....	132

Figure 4.20: Plot of the evanescent signal intensity vs. distance for different locations of the sample.	134
Figure 4.21: Scaled transmission intensity values for the gold islands on mica data set of gold islands on a mica substrate.	136
Figure 4.22: Absorption data for gold islands on mica data set "A".	137
Figure 4.23: Absorption results for the gold islands on mica data set "A" compared with theoretical calculations.	138
Figure 4.24: Scaled transmission intensity values for the "B1" data set of gold islands on a mica substrate.	140
Figure 4.25: Absorption data for data set "B1" of a sample of gold islands on mica.	141
Figure 4.26: Absorption results for the "B1" data set compared with theoretical calculations.	142
Figure 4.27: Plot of the evanescent signal intensity vs. distance for different locations of the sample for the "B2" data set.	143
Figure 4.28: Scaled transmission intensity values for the "B2" data set of gold islands on a mica substrate.	144
Figure 4.29: Smoothed absorption curves for the "B2" data set for different location of the sample of gold islands on mica.	145
Figure 4.30: Absorption results for the "B2" data set compared with theoretical calculations.	146
Figure 4.31: Tunneling intensity of the gold island over quartz data.	148
Figure 4.32: Absorption spectrum for 4.0 nm of gold heat-treated for 5 minutes at 500° C on a quartz substrate.	149
Figure 4.33: Absorption spectrum with theoretical overlays for 4.0 nm of gold heat-treated for 5 minutes at 500° C on a quartz substrate.	150
Figure 4.34: Fluorescence of the yellow dye when illuminated with a 366 nm light source.	152

Figure 4.35: Spectral distribution of the UV lamp used to excite the dye during initial testing.	153
Figure 4.36: Absorption of the yellow dye over the visible spectrum of light.....	154
Figure 4.37: Plot of the intensity as a function pump intensity for a probe held at a fixed distance from the surface of the sample.....	156
Figure 4.38: Log plot of the intensity as a function of the pump intensity for a probe held at a fixed distance from the surface of the sample which has the data separated into two sections.....	157
Figure 4.39: Log-log plot of two-photon fluorescence signal as a coated probe tip is held at a fixed position above the sample surface.....	158
Figure 4.40: Intensity of fluorescence as a function of piezo movement.....	160
Figure 4.41: This graph shows the intensity of an uncoated fiber near and far to the surface.....	162
Figure 4.42: Log-Log plots of the uncoated fiber data.....	163
Figure 4.43: Plot of the fluorescent signal for different fixed positions above the sample surface.....	164
Figure 4.44: Log-Log plot of the Far field signal of a coated fiber and the near field signal.....	165
Figure 4.45: Image taken of the surface of the yellow dye with a 632.8 nm laser.....	166
Figure 4.46: Calculated distance to the surface from the distance data set.....	168
Figure 4.47: Normalized tunneling signal for the distance data set with a theoretical approximation.....	169

Nomenclature

Å	Angstrom
AFM	Atomic Force Microscope
DI	Digital Instruments
nm	Nanometer
NSOM	Near Field Scanning Optical Microscopy
NSPM	Nonlinear Scanning Probe Microscopy
PSTM	Photon Scanning Tunneling Microscopy
SEM	Scanning Electron Microscope
SPM	Scanning Probe Microscopy
STM	Scanning Tunneling Microscopy
SHG	Second Harmonic Generation
TEM	Transmission Electron Microscopy

Chapter 1 Introduction

1.1 Background

1.1.1 Origins of Microscopy and Optical Microscopes

The field of modern microscopy began with the invention of the compound optical microscope in 1595 by Zacharias Jansen.¹ Prior to this simple lenses had been used as magnifying glasses but their resolving power was insufficient to observe the truly microscopic. In 1674 Antonie van Leeuwenhoek² constructed small polished spheres and conducted the first detailed microscopic studies and hence he is regarded as the father of microscopy.

Early compound microscopes suffered from problems in lens design and construction. However, the basic concept of using lenses to focus light that is reflected from or transmitted through an object's surface remains in modern "classical" microscopes. Since compound microscopes depend on far field optical effects their resolution is limited by diffraction and is determined by λ , where λ is the wavelength of the light used for imaging. (This is referred to as the Abbe³ barrier or the diffraction limit.) With diffraction being the limiting factor the resolution for optical microscopes is defined by the condition in which the central diffraction peak of one point source lies upon the first diffraction minimum of a second point source. This is the basis of the Rayleigh criterion which states that for a circular aperture of diameter d , the least resolvable separation is obtainable from the zero of a Bessel function and the angular resolution is approximately $1.22\lambda/d$.⁴

1.1.2 Recent Forms of Classical Microscopy

In the historical development of "classical" optical microscopes many ideas, technological advances, have been implemented in an effort to improve resolution. Oil immersion microscopes, where the sample is placed in oil with a high index of refraction, use the increased index of the oil to improve the resolution by effectively reducing the wavelength. Shorter wavelengths of light may also be used. However, there is a limit to the improvements possible due to the increasing cost of materials and fabrication as the wavelength is reduced. Moreover, fluorescence, optical absorption, source availability, and many other effects severely limit the ability to use ever smaller wavelengths. Phase contrast microscopes and confocal microscopes are another example of methods that allow a significant degree of improvement, and are widely used today.

Resolution continues to improve as alternative methods of imaging and spectroscopy are developed through the use of newer technologies (described below). These new technologies do not make confocal microscopy obsolete because recent improvements have been made through the use of two-photon⁵ and three-photon⁶ fluorescence which retain much of the operational advantages of classical microscopy. Therefore, it is expected that newer technologies will continue to provide a more diverse set of tools that supplement the older tools and provide for specialized work. A good example lies in the discussion immediately below.

1.1.3 Electron Microscopy

During its lifetime the field of microscopy has undergone three major phases in its development. The first phase, previously mentioned, is optical microscopy, the second is electron microscopy (which includes scanning (SEM) and transmission electron microscopy (TEM)), and the most recent phase is scanning probe microscopy (SPM). Each phase adds to the available tools for microscopy.

In TEM electrons scatter through the sample while in SEM electrons scatter from the surface of the sample. In both microscopes electrons are accelerated and focused onto a sample surface where they backscatter and also produce secondary electrons. A pattern reflecting the sample geometry is thereby created and focused onto an imaging plate where the image is recorded. Using electrons instead of light improves the spatial resolution of the microscope by reducing the wavelength, $\lambda = h/mv$ (the DeBroglie relation for momentum p), used to image the sample. However, electron microscopes are hampered in general by the need for extensive sample preparation methods such as metal coatings, working in vacuum, and creating thin slices (for TEM). It has recently become possible to use scanning electron microscopy to image samples at atmospheric pressure, but the difficulties of charging effects and the need for more intense beams are well known. Another drawback is that these microscopes are all diffraction limited.

1.2 Scanning Probes

1.2.1 Origins

Scanning probe microscopy is revolutionary in the analysis and imaging of small objects. This field started in 1982 with the development of the Scanning Tunneling Microscope (STM) by G. Binnig and H. Rohrer⁷. SPMs step away from the diffraction limited microscopes of the past. The method for scanning probe microscopes were first developed in the early 20th century by E.H. Synge⁸ but the potential of the process was not realized. Also, the technical ability needed to construct and operate SPMs efficiently was not possible until the advent of modern piezoelectric positioning crystals and other factors, including computer controlled data collection.

All forms of SPMs involve a probe being moved very close to a sample surface in a predetermined linear scanning pattern, normally called a raster pattern, which covers all of the area to be imaged. The probe is moved by a relatively hard piezoelectric crystal that is controlled by a computer and feedback electronics. In feedback mode the electronics maintain a constant current while a constant height mode keeps the probe at a set separation from the surface. At each point along the scan path measurements are taken, recorded and displayed on the computer screen. The composite image of the measured values at different points represents a topographical image map of the surface.

Computers opened the door for SPMs to flourish by allowing many measurements made across the surface of a sample to be displayed as a digital composite picture in a

short period of time. Piezoelectric positioners with a resolution of a small fraction of a Ångstrom were also a key development.

The development of SPMs has greatly changed the imaging process, but will not replace traditional microscopes because traditional microscopes are easy to use, have a low cost of maintenance, and image large areas of objects simultaneously (in parallel).

1.2.2 Resolution

As mentioned above, typical resolution in an optical system is defined using far field optics and is governed by diffraction effects. Resolution is determined by the ability to separate the central peak in a diffracted image of two point sources.

Resolution must be redefined for Scanning Probe Microscopes because the diffraction limitation concept is no longer valid. The limits of resolution for SPMs are governed by different parameters such as the probe size, probe shape, sample preparation, sample roughness, and sampling rate of the computer. All SPMs are limited by the response time of the piezoelectric controllers and feedback mechanism that are used. If the piezo does not react fast enough to changing conditions the probe tip can contact the surface during a scan. Many times resolution in SPM papers is listed as a wavelength fraction, but this is just a historical reference. The smallest discernable feature in an image determines the resolution. In general, the resolution must be defined in three dimensions--one normal to the surface and two lateral to the surface where the normal resolution and lateral resolution are rarely identical.

1.2.3 Types of SPMs

Today there are many forms of SPMs that are briefly described in the next section. In this work only those which use photons are discussed in detail. A major benefit of the use of photons is the very high spectroscopic resolution attainable relative to that of other SPMs and the fact that sample charging effects do not occur. Near-field optical SPMs, that rely upon an apertured probe, are not discussed in detail in this work due to the unknown qualities of the signal dependence upon the probe-to-sample gap.

The STM is the most widely known and developed of these microscopes and it is capable of subatomic-scale resolution in imaging conductive or semiconductive samples. STMs can obtain subatomic resolution by using the process of electron tunneling. A bias voltage between a sample and a metal tip is created, the tip is then scanned across the surface, and the current that tunnels across the gap between the sample and the surface is measured. This gives a high-resolution image of the electronic distribution at the surface, or the surface electron cloud, because the current density of electrons that tunnel across the gap is exponentially related to the distance between the gap and the surface. The resolution is only limited by the size of the atom, located at the end of the probe tip, to which tunneling occurs. The biggest disadvantage of the STM comes from difficulties with imaging insulators or rough samples.

Another form of SPM is the Atomic Force Microscope (AFM) which consists of a small cantilever that is rastered across the surface of the sample. This rastering may be

done while the cantilever is in constant contact, intermittent contact, or in close proximity of the surface. As the cantilever is scanned across the surface it deflects depending on the surface forces that are present. A laser reflected off the top of the cantilever is used to determine the amount of deflection, which is then recorded and displayed to give a representation of the surface topography. An AFM can also measure temperature gradients and magnetic forces. AFM images routinely magnify to varying degrees depending upon probe dimensions and sample roughness but only a very limited spectroscopic resolution is possible.

The next SPM microscope is the Near Field Scanning Optical Microscope (NSOM) which was theoretically proposed by Synge in 1928⁸ and demonstrated experimentally by Ash and Nicholles through the use of microwaves in 1972⁹. The NSOM did not move to the visible region of the radiation spectrum until 1984¹⁰. It was through the work of D. Pohl and M. Isaacson that the NSOM has developed into a practical form of SPM.

In NSOM a small aperture (much smaller than the wavelength of the illuminating light) in the scanning probe is used to gather light from the surface of a sample. It may also deliver the illumination and the sample then reradiates the light back to the aperture. A shear force feedback mechanism¹¹, where the tip is vibrated above the surface and the fundamental resonance of the fiber is observed and is proportional to the distance from the surface, is used to conduct surface topography and to keep the tip at a uniform distance from the surface. The diffraction limit can be broken because

the small aperture acts like a dipole antenna and converts the electric field in the near zone to a radiation signal. The resolution is governed by the size of the aperture.

Limitations of the NSOM come from the feedback mechanism used, the difficulty of making durable small apertures in the probe tips, and its difficulty in imaging transparent samples. There is no reliable and definitive variation in signal strength relative to the surface of the sample so that additional methods for determining the probe distance must be employed. Typically a shear force method is used, but artifacts of this method pose difficulties that make the technique unreliable in many cases.

PSTM microscopy is the form of scanning probe microscopy that will be the focus of this thesis. It was developed by T.L. Ferrell, R.J. Warmack, and R. Reddick in 1989^{12,13}. The PSTM operates by locally frustrating the evanescent field of totally internally reflected (TIR) light above the surface of a sample (engendering photon tunneling) using a tapered probe. It is analogous to the STM, although the tunneling signal arises from a beam of photons rather than from particles with a significant momentum distribution. Additionally, of course, the photon wave function is a vector wavefunction (having the orthogonal s and p polarization), and the equations for the transmission coefficient for an incident plane wave are identical for the two types of particles only for the case of s-polarized photons and electron tunneling in which spin is not important.

1.3 The PSTM Concept

1.3.1 Basic Operating Concept

Total internal reflection (TIR) and refraction have been observed for many years and were studied by Isaac Newton in 1665¹⁴. When light is incident upon a surface or there is a change in dielectric constant it undergoes reflection, refraction, absorption, and transmission, which can be described by the Fresnel relationships.

The angle of refraction of light from one medium to another is given by Snell's law,

$$n_0 \sin \theta_0 = n_1 \sin \theta_1 \quad [1.3.1]$$

where θ_0 is the angle of incidence relative to the surface normal, θ_1 is the angle of refraction relative to the normal, n_0 is the index of refraction of the incident medium (the ratio of momentum of a propagating photon in vacuum to its momentum when freely propagating in the medium), and n_1 is the index of refraction of the second medium. Snell's law is thus equivalent to conservation of the lateral component of momentum.

When the angle of the incident light reaches a critical angle it undergoes total internal reflection whereby the refracted beam lies in the refracting surface ($\theta_1 = \pi/2$). While studying TIR Newton noted that the reflected wave appears as if it penetrates into the second medium before being reflected¹⁴. That is, the reflection vertex lies beyond the boundary (now known to be at one wavelength). The associated wave is called the evanescent wave and has an electric field that falls off as $\exp[-\kappa z]$ where κ is a function of angle and relative index of refraction, and z is the distance from the interface. The evanescent wave can be frustrated by moving a third medium very close

to the first medium so that the virtual photons of the evanescent wave are converted into real photons by interaction with the third medium. This causes part of the nominally TIR incident light to transmit into the third medium. Turner in 1947 called this "frustrated" TIR¹⁵, in modern terminology it is called "tunneling".

The phenomenon of quantum mechanical tunneling occurs for both bosons and fermions. Common to both is the Debroglie relation $p = h/\lambda$, where h is Planck's constant and p is momentum. At any boundary surface the quantum form of Snell's law results for both bosons and fermions as a result of conservation of the lateral component of momentum. The index of refraction is thus generalized as described above, but remains defined in terms of the ratio of momenta of free particles in the two media. The Fresnel equations are modified in accordance with the value of the spin or polarization, but are formally identical, for example, for electrons and photons provided the electron spin has no role in the tunneling and provided the photons are polarized perpendicular to the plane of incidence. This follows immediately from the conservation of probability. The tunneling barrier is of different physical nature for electrons and photons, but this is well known.

The PSTM microscope operates by frustrating the TIR light in a sample with a scanned probe that is typically a sharpened optical fiber or pipette. The probe is scanned across the surface of the sample engendering tunneling locally at each point and captures and transmits the tunneling photons within the optical fiber or pipette to a photomultiplier tube where the photons are converted into an electrical signal. Measurements of the current for each position on the sample's surface are recorded

and displayed as a graph on which the strength of the current is proportional to the square of the electric field present at each point. The electric field strength depends on the distance between the probe and the sample, the dielectric constant ϵ or optical index n ($\epsilon = n^2$) of the sample, and the wavelength of the incident light. The point of initiation of the signal occurs at the sample surface and has nearly identical characteristics to those of a flat surface so long as the mean square roughness height is much less than the wavelength. The features are distinguished only because the signal changes dramatically across a distance of one wavelength. The main difference between a rough and flat surface is simple dipole scattering where the scattering signal varies much more slowly with distance than the tunneling signal.

Scattering represents a relatively constant background that can be removed if it is not overwhelmingly large (as can be the case in the vacuum ultraviolet). The scattering can be delineated and used to garner additional information about the sample. For example, one can use the scattered light for spectroscopic purposes or one can measure near-zone scattering patterns. By moving the beam to an angle just slightly below the critical angle, all of the tunneling signal will vanish and the scattering and real transmission are then sampled in the near zone.

The internally reflecting sample surface spawns the evanescent field at each point and the sample is coupled to the prism by an optically continuous path provided by an index matching gel. (Fig. 1.1) The distance between the tip and sample is thus measured from the top surface of the sample at each point and not from the surface of the prism. Negligible light is reflected by the prism surface because this surface is

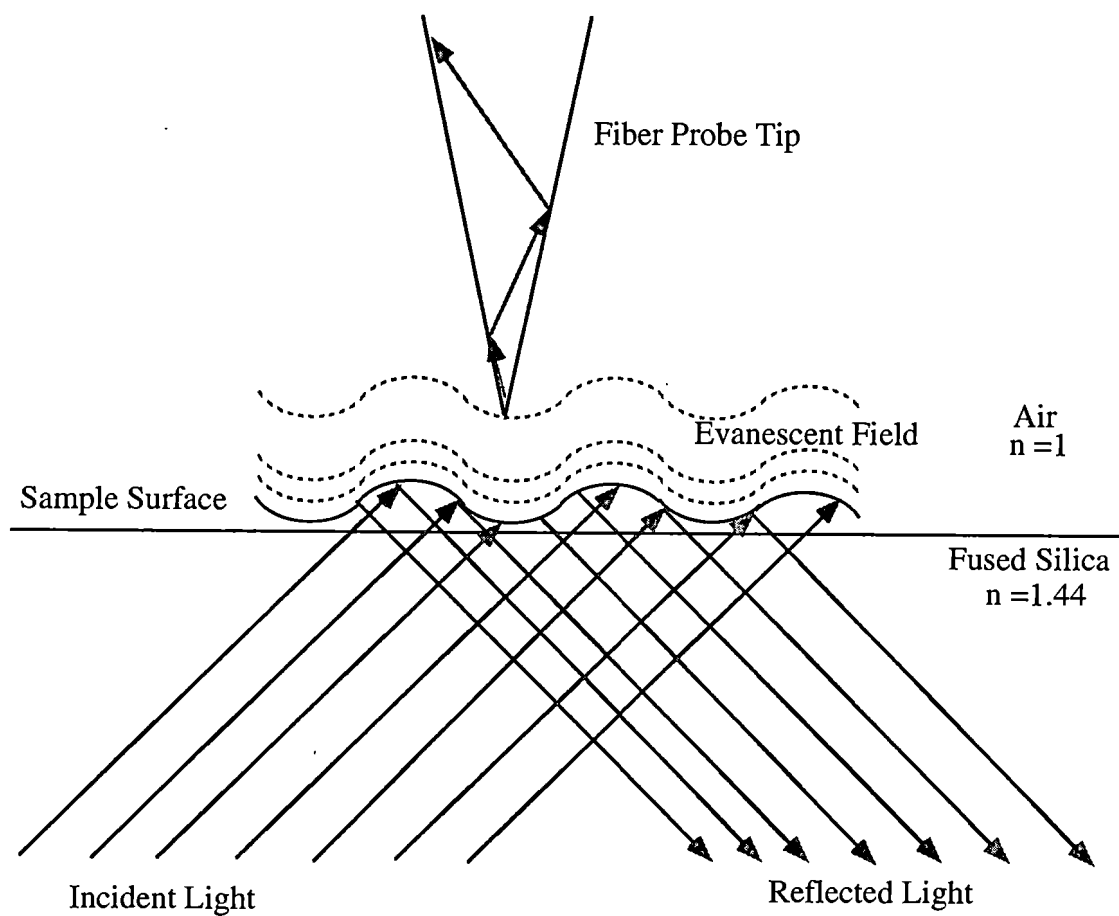


Figure 1.1: Process of tunneling from an optically coupled surface. The point of initiation of the signal occurs at the sample surface and has nearly identical characteristics to those of a flat surface so long as the mean square roughness height is much less than the wavelength.

coupled with an index matching gel to the sample mount (typically a fused silica slide). The characteristics of the reflection from the sample surface depend on the surface features. If they are small compared to the size of the light being used, their main effect in addition to the usual internal reflection is dipole scattering, or Rayleigh scattering, as mentioned earlier. For larger particles or microstructures there is higher-order scattering, however for thin samples or for samples that are transparent at the wavelength of the photons used, the scattering is not so large. If the scattering signal were large it would preclude observation of the tunneling signal that on average starts at the effective surface plane (the plane of symmetry in the normal direction). In essence, features small relative to the wavelength and which present negligible scattering into the acceptance angle of the probe are not "seen" by the light as far as leakage out of the TIR condition is concerned. By judicious choice of polarization the scattering pattern can be controlled---more can be directed into the probe if desired by using s-polarized light, while less is typically expected for p-polarized light. The conditions are altered if the sample has different polarizabilities in different directions.

This work examines one particular type of sample that has different polarizabilities along two directions. The sample consists of metal island films (Section 1.3.3.1) consisting of roughly oblate spheroidal particles with minor axis normal to the surface. The polarizability for these particles is smaller in the normal direction than in the lateral direction relative to the surface. S-polarized light scattering is associated with the lateral dimension and starts to become significant relative to absorption at a size on

the order of 120 nm for gold islands. Smaller lateral dimensions produce more absorption and less scattering. The scattering pattern is that of a typical dipole and is therefore a “doughnut” (square of cosine theta) that protrudes normal to the surface. The scattering of p-polarized light is due to a combination of the lateral and normal polarizabilities and the electric dipole induced is thus not parallel to the incident field. Therefore, the pattern for p-polarization scatters less light into the probe.

1.3.2 PSTM Resolution

A PSTM is like all SPMs in that the smallest discernable feature in an image determines the resolution. In general, the resolution is defined in three dimensions—one normal to the surface and two lateral to the surface. Since the normal resolution in the PSTM is essentially limited only by noise, it can be a very small fraction of the wavelength. It is the lateral resolution that is to be compared with that of traditional microscopies. In general, the resolution needs to be determined for each sample examined and a standard is very helpful for accomplishing this task. Assuming some knowledge of the order of magnitude of the mean square roughness height of a sample, a reference object can be obtained with well-known dimensions and imaged in like manner to the sample. The error in determining the reference dimensions is then comparable to the error involved in imaging the sample. In the case of samples with changes in optical index on the scale of these dimensions, it is necessary to use multiple incident wavelengths in order to distinguish index changes using prior measurements of dispersion in the sample. That is, the optical properties of constituents must be known if the sample has strong variations in optical density.

1.3.3 PSTM Spectroscopy

Spectroscopy has been an important part of scientific study for many years. It has been widely used to study the chemical constitution of materials. Star structure, DNA mapping, and hosts of other quantities are investigated spectroscopically. Recent developments of tags for making biological samples and the importance of properties of photoresists put on CHGD-silicon disks lead, for example, to a need for a method of studying small systems spectroscopically. Previous research has focused on using the PSTM to study a specialized case of photoluminescence from a sample. Fluorescence from stress patterns in chromium-ion-implanted sapphire along with the shift in the Cr⁺ doublet as a function of the stress pattern was studied¹⁶. Measurements were also made of Surface-Enhanced Raman Scattering (SERS) of cobalt phthalocyanine and SERS studies of benzoic acid were also conducted¹⁷.

1.3.4 Samples for the PSTM in the Present Work

1.3.4.1 Metal Island Films

In this experiment a thin film of small metal islands was used as a sample. Metal island films have been studied for many years^{18,19} because they possess many interesting optical properties and because they are easy to produce. Another motivation for studying metal island films derives from computer chip production where the limitation on how thin one can make wires, on the natural oxide that forms on silicon, is very important. When copper is below a certain thickness islands are formed.

Typically islands can be produced by a slow evaporation of metal, less than a 100 nm thick, in a vacuum evaporator. The result is an electrically and physically discontinuous metal film that self-anneals at room temperature²⁰. When the metal film is heated it allows the metal to migrate around the surface so that it pools into larger particles around surface defects as oblate spheroids of nanometer scale depending upon the evaporated thickness. The pooling occurs at temperatures well below the melting point of the material. As the temperature of heating is increased the distribution of particle shapes becomes more uniform and the particles become more like spheres.

It is the shape of the particle that leads to the unique optical properties. Plasmon oscillations along the axis of the particles govern absorption and scattering from the particle. An excellent model of these oscillations was developed by Kennerly, *et.al.*²⁰ and is discussed in more detail in the theory section.

1.3.4.2 Fluorophores

Fluorophores are molecules that undergo fluorescence and are commonly used as probes in biological experiments. In biology fluorophores are used to stain or mark specific parts of a cell (sample) or process so that they can be easily seen in optical microscopy.

Fluorescence is a process in which a photon is absorbed and then excites an electron from the ground state of a molecule to an excited state where the electron remains temporarily ($\sim 10^{-9}$ sec)²¹ before returning to the ground state. When the electron returns to the ground state a photon, corresponding to the energy difference

($E=h\nu$) between the states, is emitted. The emitted energy is normally less than the energy of the absorbed photon because of energy lost due to vibration/rotation of the molecule and to collisions with other molecules while in the excited state. This energy loss is called the Stokes shift. The Stokes shift is advantageous in studying cells, or other materials, which have been marked with fluorophores because the excitation and fluorescence peaks do not overlap in the spectrometer.

1.4 The Nonlinear Tunneling Microscope (NSTM)

1.4.1 Motivation

The resolution of any SPM is improved if the rate of change of the signal is stronger as a function of the distance z between the sample and the probe. Thus, for example, the STM obtains subatomic resolution normal to the surface because the electron-tunneling signal changes by an order of magnitude for each 0.1 nm change in z . The difficulty encountered is that the probe must be placed within a few tenths of a nanometer from the surface in order to acquire the signal. To gain an improvement in resolution, over that attainable with a PSTM while retaining the use of photons, it is clear that one must devise a method that provides a more rapidly changing signal and a method of quantitatively situating the probe closer to the surface. The resolution attained by STM is not likely to be reached by any photonic method, but a movement toward atomic resolution is desirable. The use of photons is equally desirable due to the fact that spectral resolution with photons far surpasses that which is possible with electrons. A potential solution to this is offered below.

1.4.2 Operational Principle of the Nonlinear Scanning Probe Microscope (NSPM)

If a molecule is placed in a sufficiently intense uniform electric field \mathbf{E} then the induced dipole moment \mathbf{p} is no longer simply proportional to \mathbf{E} . Rather there is also a quadratic dependence upon the electric field. The quadratic term coefficients are small relative to the value of the coefficient of the linear term (linear polarizability). The value of at least one component of \mathbf{E} must therefore be sufficiently large so as to compensate for the smallness of the quadratic coefficients. The electromagnetic radiation emitted as a result of a significant nonlinear polarizability has a portion that has twice the frequency of the incident field \mathbf{E} . This occurs in classical terms because of the influence of a quadratic upon the Fourier components of the field. In quantum terms, two photons are absorbed in an electronic transition to produce emission of a single photon of equal *total* energy upon de-excitation of the electron.

As mentioned in the discussion of confocal microscopy, two-photon processes are already noted to be useful in microscopy. A fluorescent molecule can be induced to fluoresce using photons of much lower frequency than ordinarily is required by using a high intensity and thereby causing a nonlinear coupling. In the highest intensity region of a beam, the intensity may be set so that only a very small beam cross section produces the effect. In this manner the fluorophore can be located with high resolution. The primary drawback is that a fluorophore will chemically decay following emission of approximately one million photons and the image might not be acquired before the decay. It would be desirable to stimulate the nonlinear process only at the moment of signal acquisition.

A metal-coated probe can be used to stimulate the high field intensities needed for generating second harmonic effects. It is well known that a sharpened metal probe concentrates charges near the metallic tip, which is sometimes called "the lightning rod effect". This effect has been used by researchers to conduct SERS experiments and surface-plasmon-based field amplification²²⁻²⁶. This enhancement has also recently been demonstrated using a solid gold probe that was fixed very close to a sample's surface²⁷. Unfortunately, the investigation was carried out in the far zone and no attempt was made to use the effect for an improved method of SPM. Nevertheless, the effect was demonstrated to occur in line with an early work by Wetzel²⁸.

As the metal coated probe tip moves across a sample surface only the sections of the sample directly underneath the tip will experience field enhancement. The increased strength will be highly localized. This means that fluorophores on the surface of the sample will only be excited when the probe is directly overhead which will decrease the effects of photo-bleaching. Ordinarily, the presence of a metal can at least partially quench fluorescence as excitation produce energy delivered to the free electrons of the metal. However, the frustrated TIR geometry offers the advantage of circumventing the nonfluorescent energy transfer mechanism and instead enhances the fluorescence. Therefore, the fluorophore need last for only as long as the signal is engendered by the probe that simultaneously detects it. The fact that the fluorescent signal is the most intense, or perhaps only present, when the probe is immediately located to collect the signal improves the effectiveness of the device.

The enhancement effect only occurs to a significant degree within a few tens of nanometers of the probe tip and increases with decreasing distance with the typical dipole-dipole interaction distance dependence of distance to the inverse sixth power.

1.4.3 Introduction of Distance to Surface

One aspect of the field enhancement is that it is greatest very close to the apex of the probe tip which means that the distance between the sample and the probe tip is very important. A method of determining how close the probe is to the surface becomes very important. It can also be useful in fluorescence and any other PSTM research. The absolute distance to the surface would allow for more direct comparisons of experimental results. Of particular note is that the absolute distance need only be determined infrequently since the piezoelectric scanner has fractional Ångstrom resolution. By knowing the absolute distance, collisions with the surface can often be avoided as the probe is approached in order to attain better resolution. Additionally, the scattering pattern can be measured at known distances and unfavorable effects can be delineated. An example of the latter might be effects due to electrostatic charging in a dry atmosphere. These effects can cause the probe to actually bend if the sample is similarly charged. A reliable method of distance determination is also essential to the development of scanners that can more easily be placed close to a rough surface without colliding laterally during a raster.

A method for determining the distance to the surface has been developed and is presented in this work. An approximation based on the difference between tunneling signals at different wavelengths and polarizations has been theoretically and

experimentally tested. The basic idea of distance to the surface calculations is to develop a quantitative model of signal strength versus distance.

1.5 Scope of Present Research

A Photon Scanning Tunneling Microscope (PSTM) was used to examine the possibilities and difficulties associated with optical scanning probe analysis.

Improvements were made in the physical design of the microscope through the addition of a rotating mirror assembly and a set up for performing spectroscopic work was developed.

Incorporating absorption spectroscopy into the design is an improvement in the capabilities of the PSTM microscope because all previous spectroscopic work dealt with fluorescent samples²⁹. Results showing the absorption spectra of gold island films are presented which demonstrate the ability of the PSTM to obtain localized absorption spectroscopy data. Absorption studies open up a new area of research for the PSTM by expanding the capabilities of the microscope to do spectroscopic work on small sample areas while imaging the surface. Gold island absorption is important to different types of sensor work. As physics pushes the boundaries of nano-technology the ability to characterize localized surfaces area will play a much greater role.

Images of gold island films are presented that demonstrate resolution possibilities. These images highlight the ability of the microscope to measure and map the electromagnetic topography of a sample.

Another growing area of research and development is the NSPM. The NSPM is used to study compounds that undergo two-photon fluorescence. Two-photon compounds have recently been studied in many biological systems from cancer research to DNA characterization³⁰. The PSTM is ideally suited to help in this field of study. This paper shows that the detection of the two-photon signal with the PSTM is possible. An experiment is also presented which attempts to demonstrate that a metal coated fiber probe could be used to enhance the field strength of the pumping laser. The results do not conclusively demonstrate tip enhancement effects but do demonstrate the ability to measure two-photon excitation with the coated probe.

One of the problems in determining if two-photon enhancement occurs is a lack of accurate knowledge of the distance between the probe and the sample surface. Enhancement effects are only expected to occur when the probe to sample separation is very small. A theory is presented and tested that allows the absolute distance to surface to be measured. Different wavelengths of light are used to determine the absolute distance to the surface.

Finally, the complete work presents a better understanding of how the tip interacts with the sample substrate for different wavelengths of incident light. This improves the possibility for the effective and improved use of optical probe analysis.

Chapter 2 Theory

In this chapter the theory of the PSTM is developed starting from the basics of light reflecting and refracting at an interface and then is developed to a model for the probe tip as a truncated, and then parabolic cone. The theoretical aspects of gold islands are presented along with a discussion on the effects of scattering in the formation of an image with the PSTM. This section is then followed by a discussion on two-photon fluorescence. Finally, a calculation is presented which will allow the distance between a probe tip and the surface to be determined.

2.1 Photon Scanning Tunneling Microscope (PSTM)

The PSTM operates by frustrating the evanescent field of TIR light above the surface of a sample with a sharpened fiber probe. (Fig. 2.1) In modern language, the probe induces tunneling of the photons, converting the virtual photons into real photons. The amount of light that tunnels through the air gap, between the sample and a sharpened fiber probe, is monitored as the probe tip is moved above the surface of the sample. Measurements of the tunneling current, which is proportional to the magnitude of the Poynting vector³¹ within the probe, are recorded for each position on the sample's surface and are displayed as a graph. The electric field strength depends strongly on the distance between the probe and the sample, the dielectric constant ϵ or optical index n ($\epsilon = n^2$) of the sample, and the wavelength of the incident light.

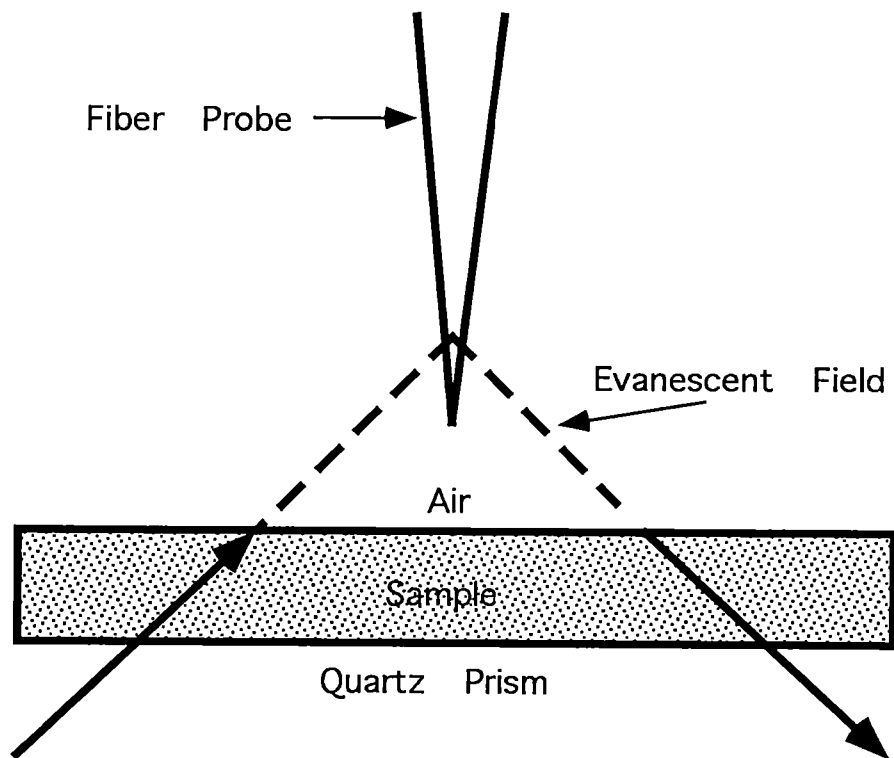


Figure 2.1: Light under TIR is frustrated by the introduction of a fiber probe into the evanescent field. The vertex of the reflection (evanescent field decay length) is on the order of one wavelength, of the incident light, from the surface.

2.1.1 Reflection and Transmission

When light is incident upon an interface or change in dielectric constant it undergoes reflection, absorption, and refraction. Refraction of the transmitted light as it passes from one medium (n_0) to another (n_1) is described by Snell's law³² (Fig. 2.2) which is produced from the conservation of the lateral component of momentum and is rewritten here as

$$n_0 \sin \theta_0 = n_1 \sin \theta_1 \quad [2.1.1]$$

where n_0 and n_1 are the indices of refraction for the first and second medium while θ_0 and θ_1 are the incident and refracted angles of light with respect to the normal of the interface. When absorption is significant one can introduce complex angles in Snell's law or more physically use complex momenta.

When the angle of the incident light reaches a critical angle (θ_c) it undergoes total internal reflection (Fig. 2.3) whereby the refracted beam lies in the refracting surface ($\theta_1 = \pi/2$). The critical angle is defined by

$$\sin \theta_c = \frac{\sin\left(\frac{\pi}{2}\right)}{n_0} = \frac{1}{n_0} \quad [2.1.2]$$

Once the critical angle is reached light no longer propagates through the second medium but propagates along the interface between the two mediums and the total

Snell's Law

$$n_o \sin \theta_o = n_1 \sin \theta_1$$

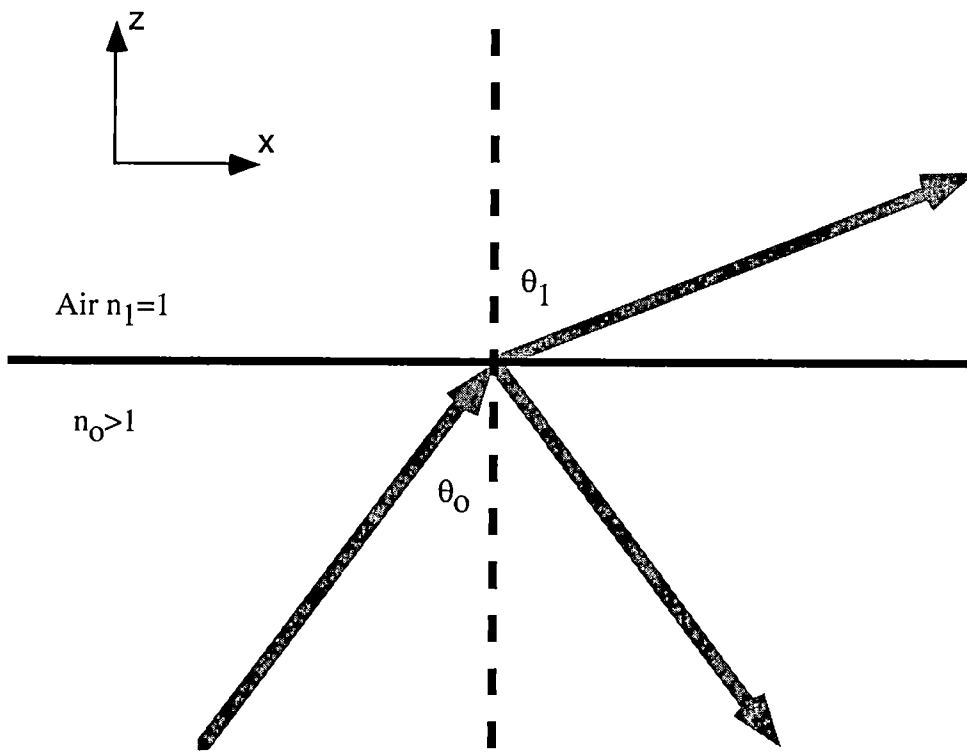


Figure 2.2: Refraction of light according to Snell's law.

$$n_0 \sin \theta_0 = 1$$

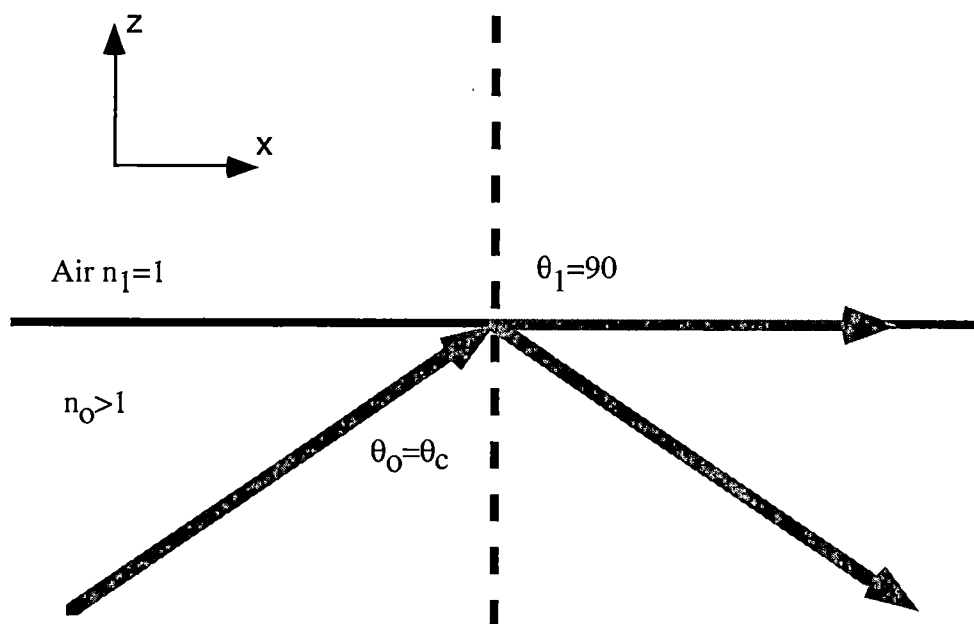


Figure 2.3: Illustration of the critical angle in TIR.

energy of the light is reflected back into the medium of incidence. As it propagates along the interface it has an exponentially decaying field strength in the direction normal to the interface (surface) called the evanescent wave. The electric field in the second medium is given for angles less than the critical angle by

$$E_t = E_o e^{-i\omega t} e^{ik_x x + ik_z z} \quad [2.1.3]$$

$$k_x = \frac{\omega}{c} \sin \theta_o \quad k_{zt} = \left[\left(\frac{\omega^2}{c^2} \right) \left[1 - n_o^2 (\sin \theta)^2 \right] \right]^{\frac{1}{2}} \quad [2.1.4]$$

where ω is the frequency of the incident light, θ is the angle of incidence and n_o is the index of refraction of the substrate. When the critical angle is exceeded k_{zt} becomes imaginary and the electric field has a real, decreasing exponential dependence normal to the surface. A plot of the intensity ($|E|^2$) of the field for different angles of incidence and a wavelength of 633 nm is given in Fig. 2.4. As the angle of incidence, θ , is increased the fall off (decay) in the intensity of the evanescent field as a function of distance from the surface becomes more rapid. In Fig. 2.5 the field intensity for different incident wavelengths (700, 600, 500, and 400 nm) of light, at the same angle of incidence, are shown. In this case one can see that intensity, as a function of distance from the surface, for different wavelengths of light decreases more rapidly for shorter wavelengths.

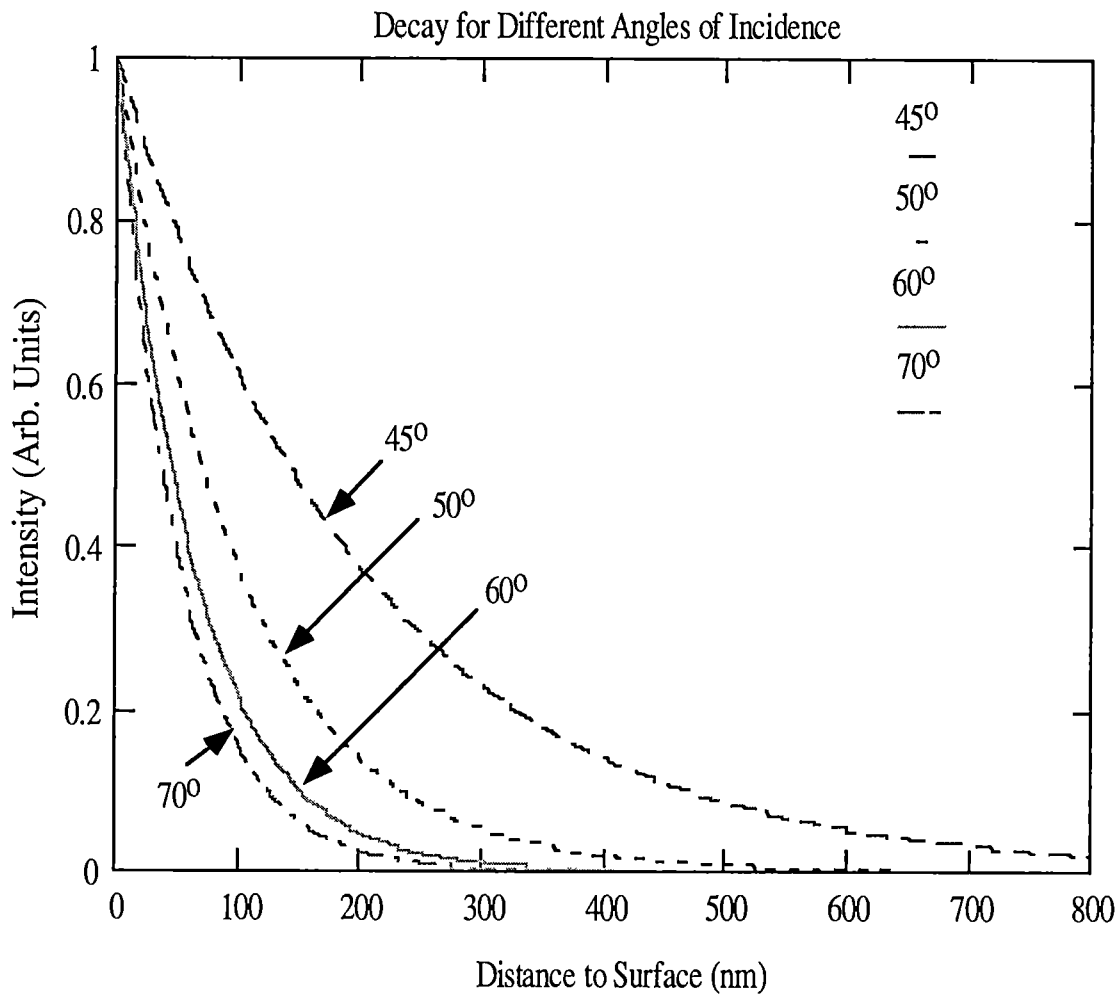


Figure 2.4: Evanescent field intensity as a function of distance to surface for different angles of incidence (45° , 50° , 60° , 70°). The wavelength of the light was 633 nm incident on a quartz-air interface ($n_{\text{quartz}} = 1.457$).

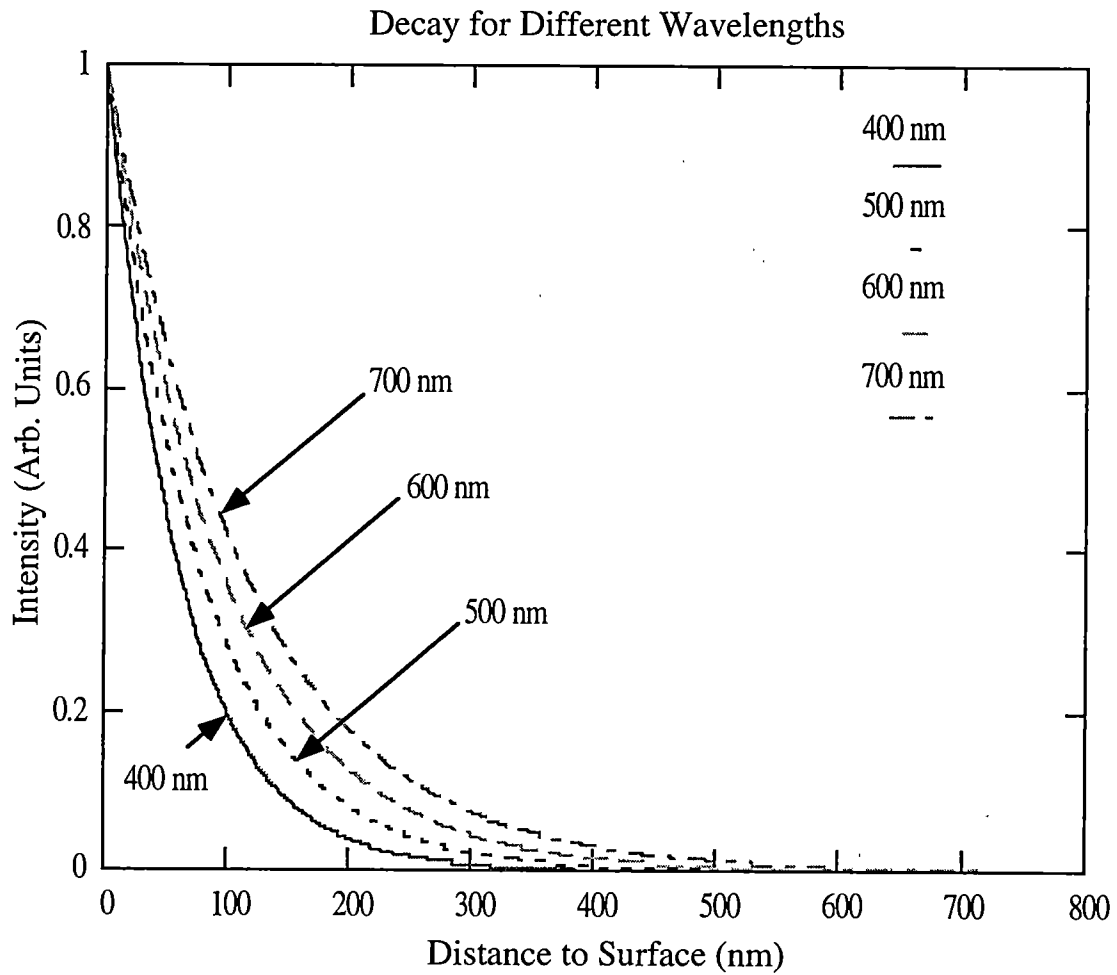


Figure 2.5: The evanescent field intensity for as a function of distance to the to surface for different wavelengths (400, 500, 600, and 700 nm). S-polarized light, incident at an angle of 50° on a quartz-air-quartz interface, are plotted vs. the distance between the probe and the surface. Here $n = 1.452$ for 700 nm light, $n=1.457$ for 600 nm light, $n = 1.462$ for 500 nm light, and $n = 1.470$ for 400 nm light.

To further develop the theory of reflection and transmission the Fresnel relationships,³³ that give the ratio of the reflected and transmitted electric field amplitudes to the incident electric field amplitude, are presented. These relationships, which are polarization dependent, can be derived from Maxwell's³⁴ equations by meeting the boundary conditions at the interface.

Fresnel relationships for s-polarization (light polarized perpendicular to the plane of incidence) are given by

$$r_s = \frac{n_o \sin \theta_o - n_1 \sin \theta_1}{n_1 \cos \theta_1 + n_o \cos \theta_o} \quad [2.1.5]$$

$$t_s = \frac{2n_o \cos \theta_o}{n_1 \cos \theta_1 + n_o \cos \theta_o} \quad [2.1.6]$$

and for p-polarization (light polarized parallel to the plan of incidence) are given by

$$r_p = \frac{n_1 \cos \theta_o - n_o \cos \theta_1}{n_1 \cos \theta_o + n_o \cos \theta_1} \quad [2.1.7]$$

$$t_p = \frac{2n_o \cos \theta_o}{n_1 \cos \theta_o + n_o \cos \theta_1} \quad [2.1.8].$$

where θ_o is the angle of incidence relative to the surface normal, θ_1 is the angle of refraction relative to the normal, n_o is the index of refraction of the incident medium (the ratio of momentum of a propagating photon in vacuum to its momentum when freely propagating in the medium), and n_1 is the index of refraction of the second medium.

Once the critical angle has been reached (TIR conditions) Snell's law indicates that

$$n_1 \cos \theta_1 = i \sqrt{n_o^2 \sin^2 \theta_o - n_1^2} \text{ for } n_1 > n_o. \quad [2.1.9].$$

Under TIR conditions the reflectivity,

$$R = r^2, \quad [2.1.10].$$

becomes 1 and the transmittance,

$$T = \frac{n_1 \cos \theta_1}{n_o \cos \theta_o} t^2, \quad [2.1.11].$$

becomes imaginary which indicates that all of the incident light is reflected, assuming a non-absorbing material. The reflectivity and transmittance are ratios of the transmitted and reflected flux with respect to the incident flux on the interface.

2.1.2 Frustrated TIR

When a third medium is moved very close to the first medium the evanescent wave becomes frustrated so that the virtual photons of the evanescent wave are converted into real photons and propagate in the third medium as shown in Fig. 2.6.

The frustration of the signal modifies the transmission and reflection of the light and can be represented by Fresnel coefficients that are modified for the three-layer system (Quartz-Air-Quartz). If the third medium has the same index as the first

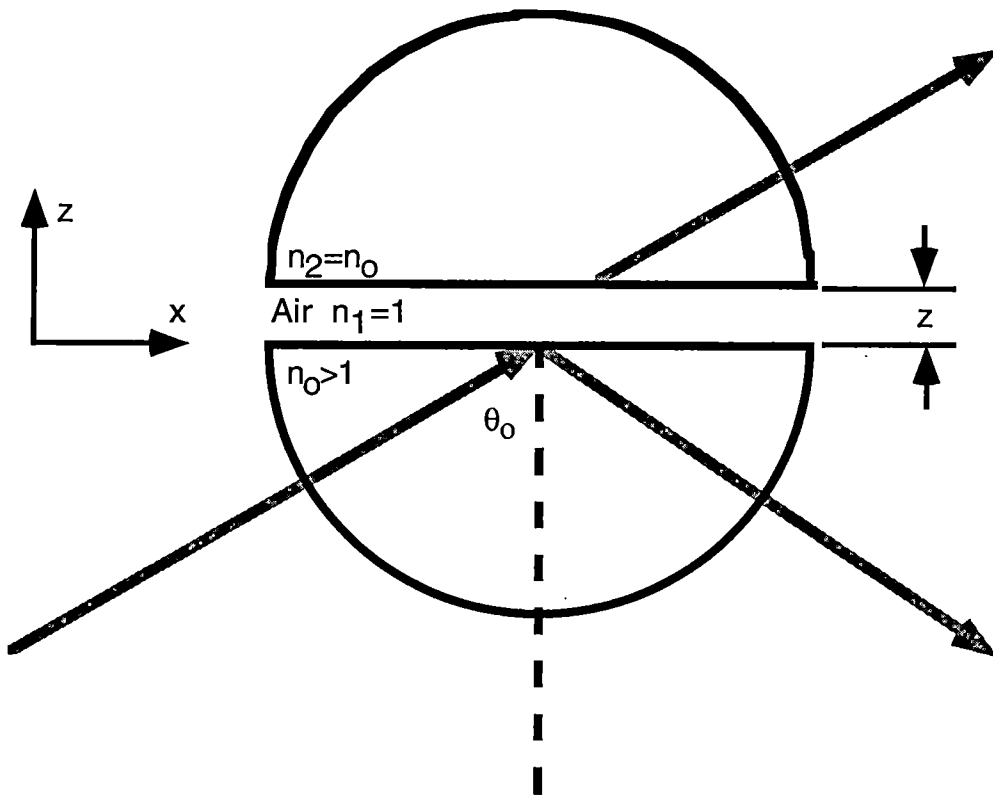


Figure 2.6: Illustration of the transmission across an air gap for planer surfaces of two identical materials.

then the Fresnel transmission and reflection coefficients for s-polarization are given by

$$t_s = \frac{1 - \cos \alpha}{\cosh 2b - \cos \alpha} \quad [2.1.12]$$

$$r_s = \frac{\cosh 2b - 1}{\cosh 2b - \cos 2\alpha} \quad [2.1.13]$$

and p-polarization are given by

$$t_p = \frac{2 \sin^2 \bar{\alpha}}{\cosh 2b - \cos 2\bar{\alpha}} \quad [2.1.14]$$

$$r_p = \frac{\cosh 2b - 1}{\cosh 2b - \cos 2\bar{\alpha}} \quad [2.1.15]$$

where

$$b = \frac{2\pi z s}{\lambda} \text{ with } s = (n_o^2 \sin^2 \theta_o - 1)^{\frac{1}{2}} \text{ and } (\theta_o > \theta_c) \quad [2.1.16]$$

$$\cos \frac{\alpha}{2} = \frac{\cos 2\theta_o + n_o^2}{1 - n_o^2} \text{ and } \cos \bar{\alpha} = \frac{\cos^2 \theta_o - n_o^2 s^2}{\cos^2 \theta_o + n_o^2 s^2} \quad [2.1.17]$$

This is the solution for two planar interfaces. The transmission function for the planar case is plotted as a function of the separation h for different angles of incidence in Fig. 2.7 and for different wavelengths at a fixed angle in Fig. 2.8. These graphs show a flattening of the transmission intensity, as the separation distance approaches zero, that is different from the single interface effect shown previously. (Fig. 2.4, Fig. 2.5) The transmission differences caused by different wavelengths and angles of incidence are still present in the figures. (Fig 2.7, Fig. 2.8)

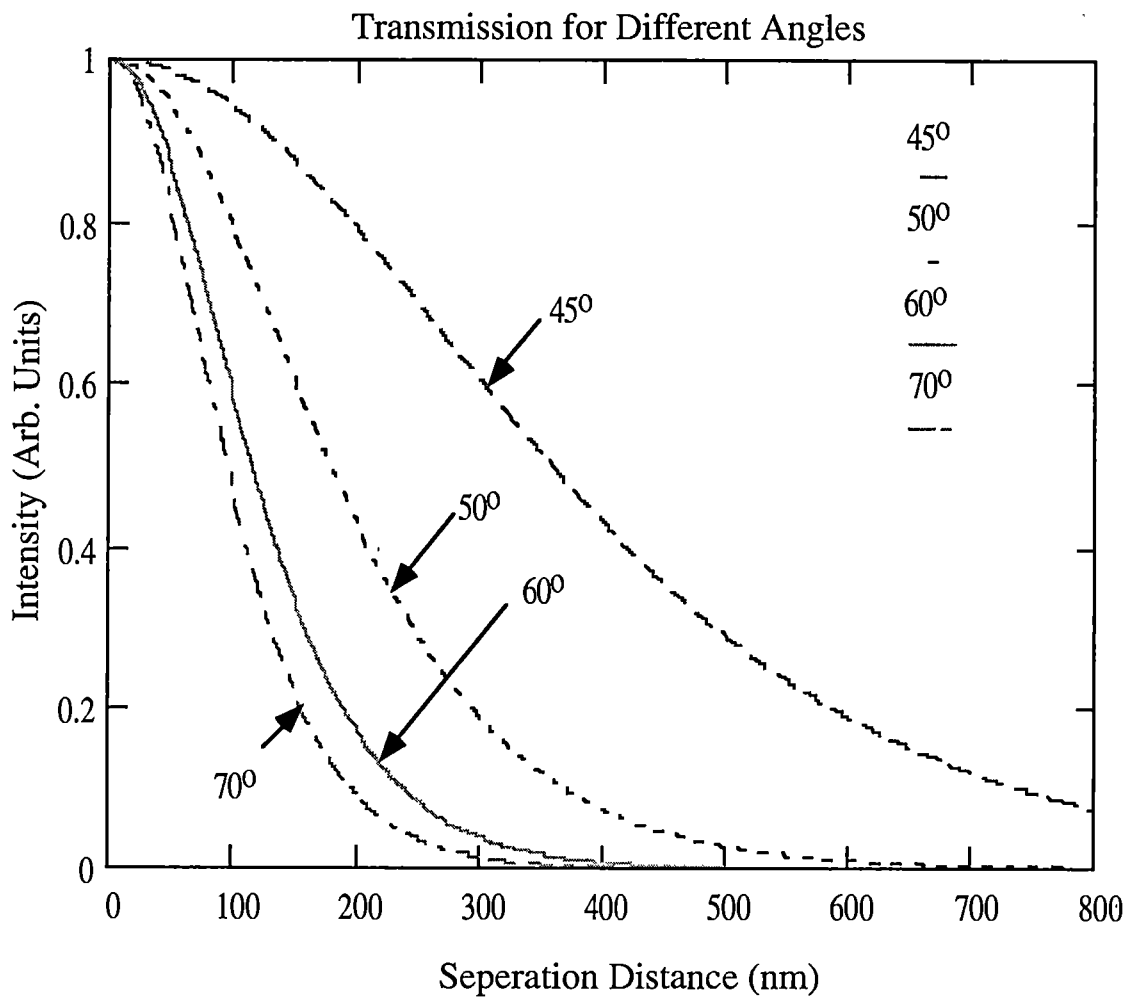


Figure 2.7: Transmission for a plane-air-plane interface for different angles of incidence (45°, 50°, 60°, 70°). S-polarized 633 nm light is plotted vs probe sample separation distance. The index of refraction was set to $n = 1.457$.

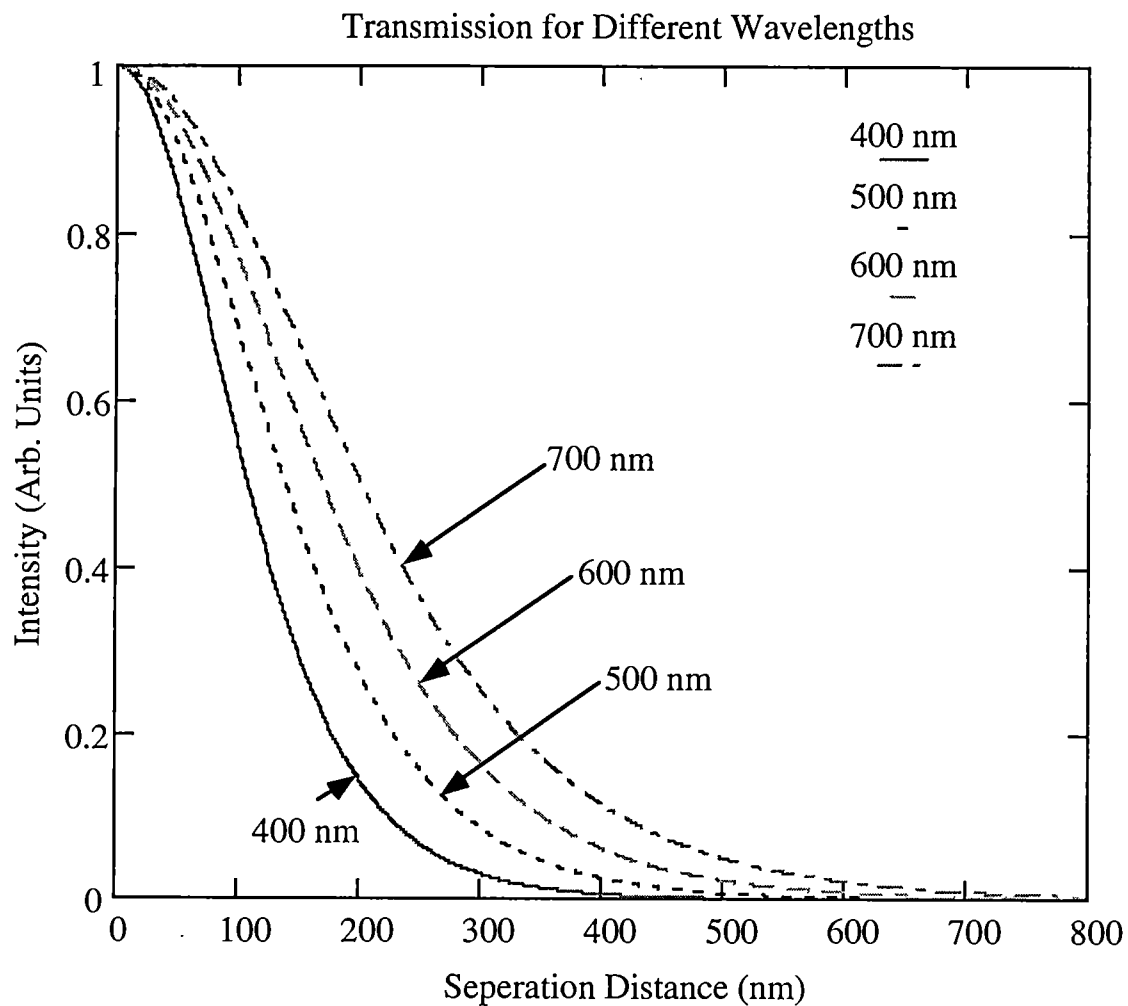


Figure 2.8: Transmission in the plane-air-plane interface for different wavelengths (400, 500, 600, and 700 nm) of light. The light has s-polarization and a 50° angle of incidence. ($n = 1.452$ for 700 nm light, $n = 1.457$ for 600 nm light, $n = 1.462$ for 500 nm light, $n = 1.470$ for 400 nm light)

2.1.3 Truncated Cone Approximation

The planer solution for photonic tunneling is a good description of the tunneling process but does not model the working conditions of the PSTM, which uses a sharpened fiber probe instead of a plane. Therefore, a better approximation for the PSTM models the probe as a truncated cone where the probe shape looks like a flat stair surface as seen in Fig. 2.9. In this way the probe is modeled as a collection of planar surfaces that step away from the interface. (A one nm step size is used for all of the calculations in this paper.)

It is assumed that the transmission to each point along the probe's surface is proportional to the transmission for a planar surface located at the same separation h . The planar transmission for each step is multiplied by the area of the step, at that separation from the surface, then the sum of the transmissions is calculated and divided by the total surface area of the probe to give the transmission for a plane-air-cone interface.

$$T_{\text{tot}} = \frac{T_1 A_1 + T_2 A_2 + T_3 A_3 + \dots}{A_1 + A_2 + A_3 + \dots} \quad [2.1.18]$$

In Fig. 2.10 the transmission intensities for 600 nm and 500 nm light in the planer-air-truncated cone approximation are presented. The transmission intensities in this figure differ from the plane-air-plane case (Fig. 2.8) in that the transmission intensity, between wavelengths, remains different even when the probe is touching the

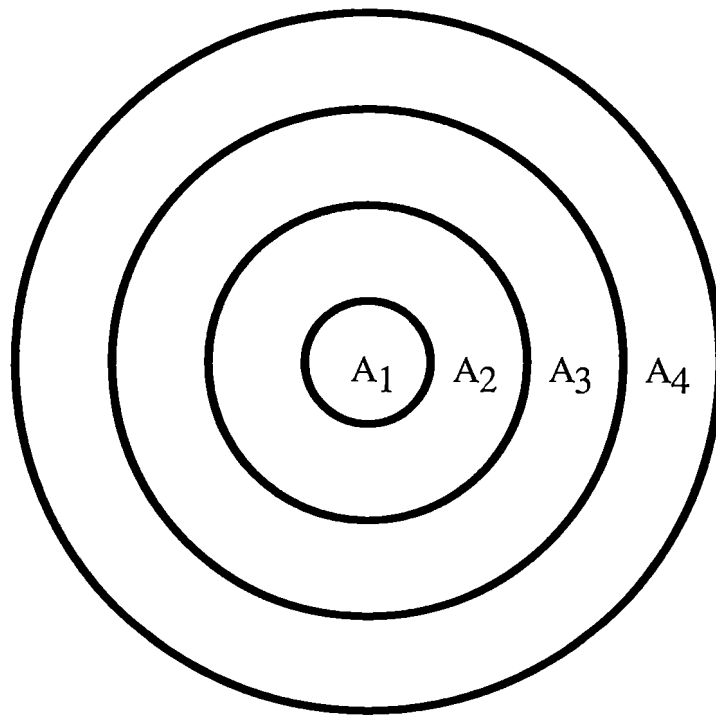
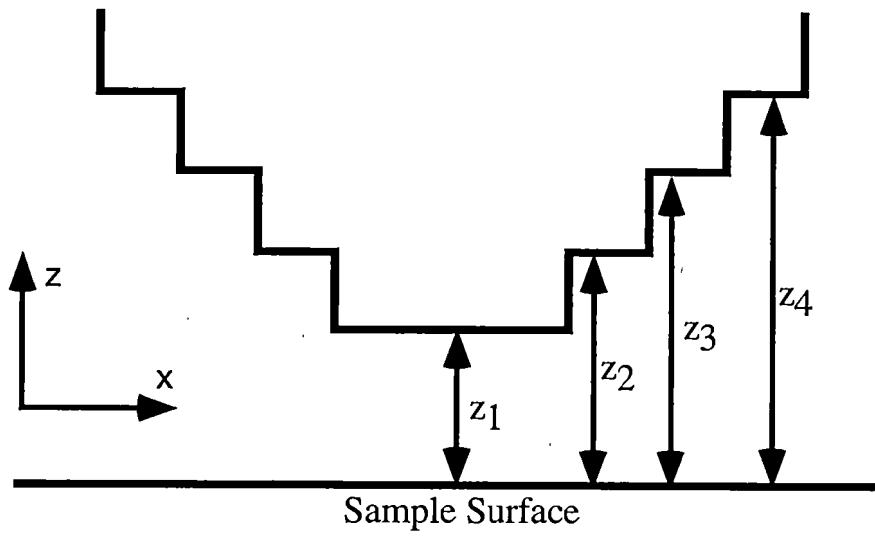


Figure 2.9: Diagram of the steps and areas used to calculate transmission for the truncated cone approximation. The distance between the probe surface area, A_i , for each step is shown as z_i .

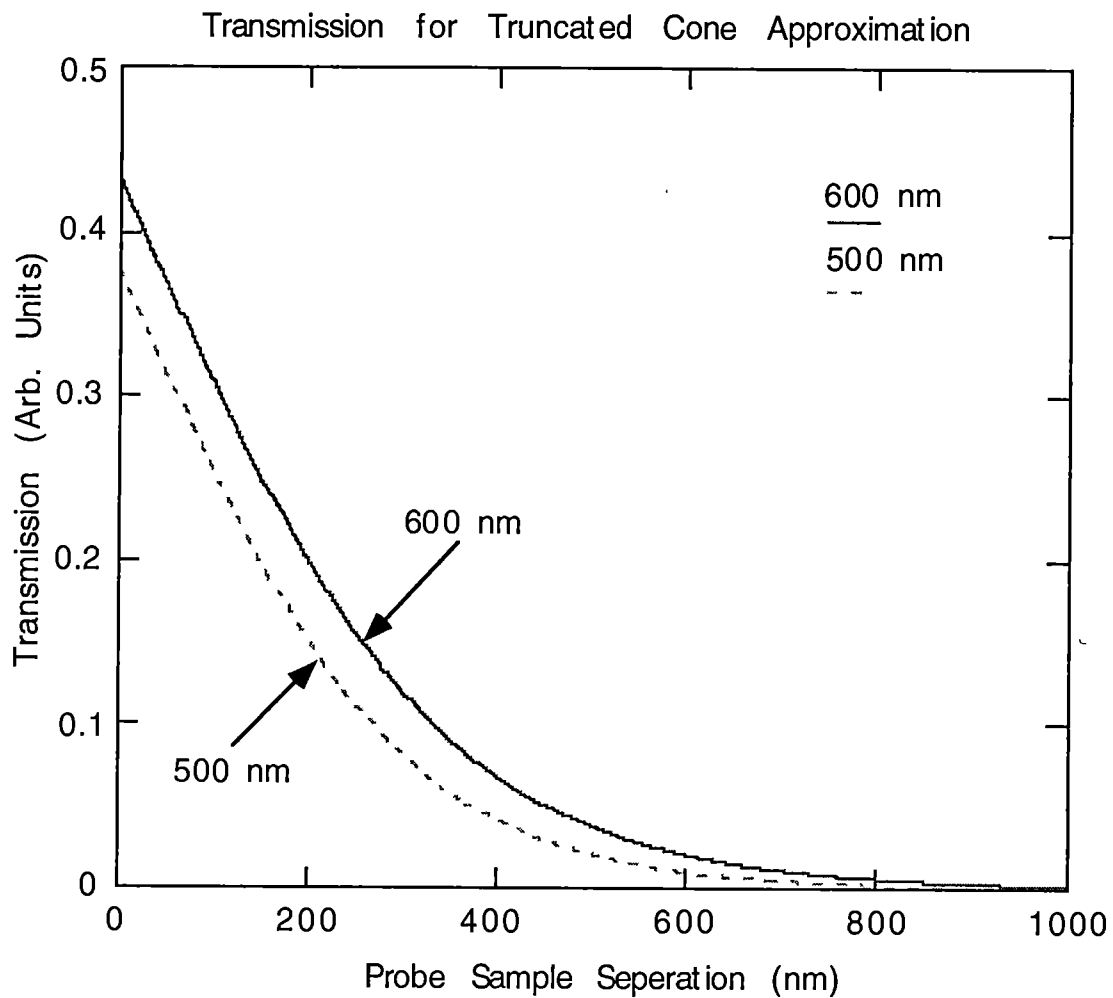


Figure 2.10: Transmission vs. distance for the stepping approximation of a truncated cone above a planner surface. The s-polarization case for 600 nm (solid line) and 500 nm (dashed line) light are shown for a fixed angle of incidence (50°). ($n=1.457$ for 600 nm, $n=1.462$ for 500 nm) The truncated section of the probe is 100 nm wide and the $1/2$ angle of probe is 20° .

surface. In the plane-air-plane case the intensities for different wavelengths go to unity when the surfaces are touching. The difference in intensities develops because light with a longer wavelength has higher tunneling intensities for any given probe sample separation. Since the truncated cone approximation sums over areas of the probe at different distances from the surface the longer wavelengths end up with larger tunneling intensities than shorter wavelengths.

The difference in tunneling intensities can also be used to enhance the resolution of the microscope. The resolution is enhanced due to an effective tip sharpening effect. Since the evanescent field falls off exponentially the closest part of the probe collects the dominant part of the tunneling signal. The effective tip radius calculated using the truncated cone model is shown in Fig. 2.11, which plots the percent of signal transmission as a function of the tip radius. This graph shows that 90 percent of the signal comes from a tip with a radius of less than 205 nm for 600 nm light and 181 nm for 500 nm light. Therefore, a shorter wavelength (which means faster intensity decay) leads to a smaller sampling probe and a smaller sampling area on the surface of the sample. Tip enhancement (or resolution improvements) is also affected by increasing the angle of incidence. In Fig. 2.7, from section 2.1.2, the decay rate is shown to increase as the angle of incidence increases which effectively sharpens the probe tip in the same manner as decreasing the wavelength.

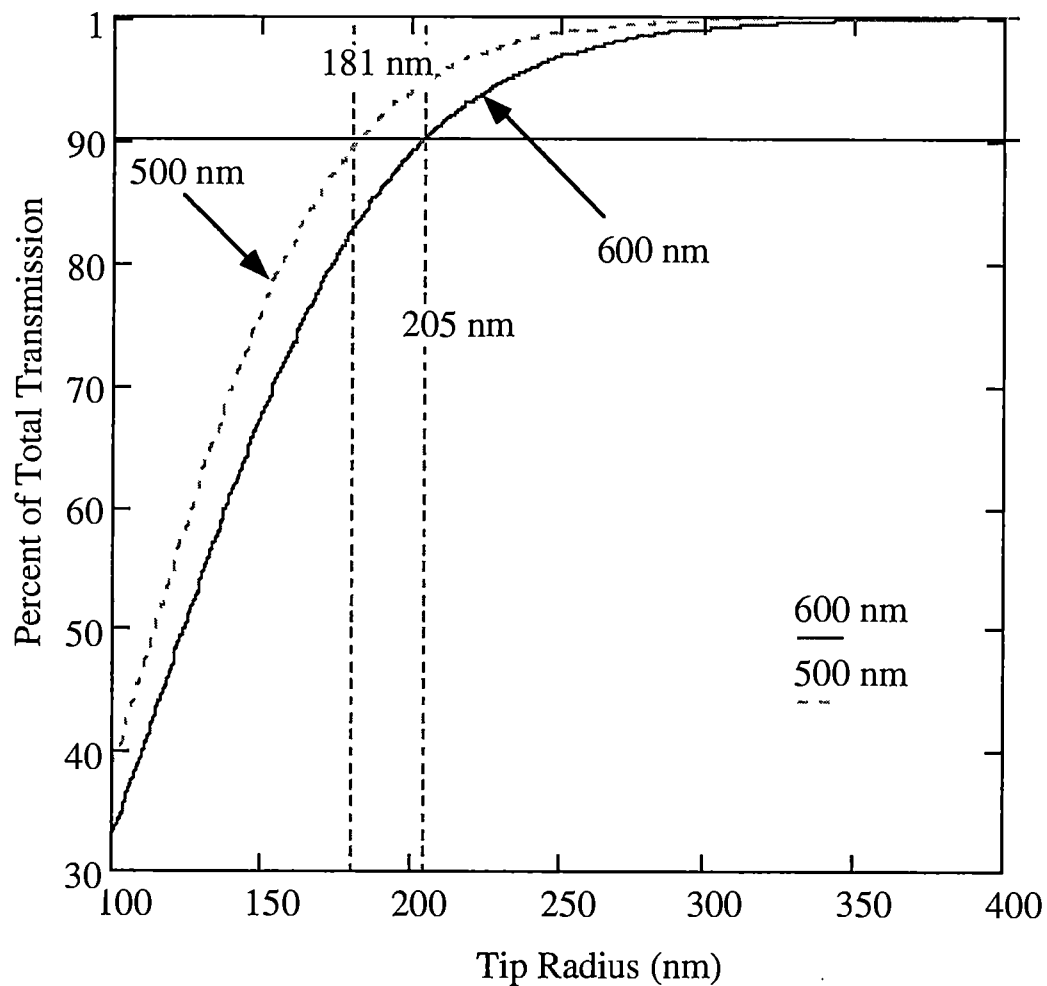


Figure 2.11: Percent signal transmission as a function of the radius of the tip for the plane-air-truncated cone approximation. The s-polarization case for 600 nm (solid line) and 500 nm (dashed line) light at a fixed angle of incidence (50°). ($n=1.457$ for 600 nm, $n=1.462$ for 500 nm) The flat section of the tip is 100 nm and $1/2$ angle of tip is 20° .

2.2 Absorbance for Gold Islands

In this experiment a thin film of small metal islands is created and used as a sample. Metal island films have been studied for many years because of their many interesting optical properties. Production of metal island films involves a slow deposition of metal in a vacuum evaporator to produce a thin layer, less than 100 nm, of discontinuous metal film^{18,20,35}. After deposition the sample is heated, which allows the metal to migrate around on the surface where it will pool around defects, causing small particles to be formed. Pooling occurs at temperatures well below the melting point of the material but higher heating or increased heating time leads to more uniformly shaped particles on the surface.

2.2.1 Oblate Spheroid Theory

The theory that best describes the absorption and scattering of gold metal islands uses oblate spheroidal coordinates and the excitation of surface plasmons along major and minor axis of the spheroid as seen in Fig. 2.12. This theory of small metal particles has been developed previously by many researchers³⁶⁻³⁹.

First, Laplace's equation $\bar{\nabla}^2 V = 0$ is solved and the solution in oblate spheroidal coordinates (η, θ, ϕ) is given by

$$V_{in} = \sum_{l=0}^{\infty} \sum_{m=0}^l \sum_{p=\pm 1} A_{lmp} Q_{lm}(i\eta_o) P_{lm}(i\eta_o) Y_{lmp}(\theta, \phi) \quad [2.2.1]$$

$$V_{out} = \sum_{l=0}^{\infty} \sum_{m=0}^l \sum_{p=\pm 1} B_{lmp} P_{lm}(i\eta_o) Q_{lm}(i\eta_o) Y_{lmp}(\theta, \phi) \quad [2.2.2]$$

The arrows in each particle indicate the direction of the electric field oscillations.

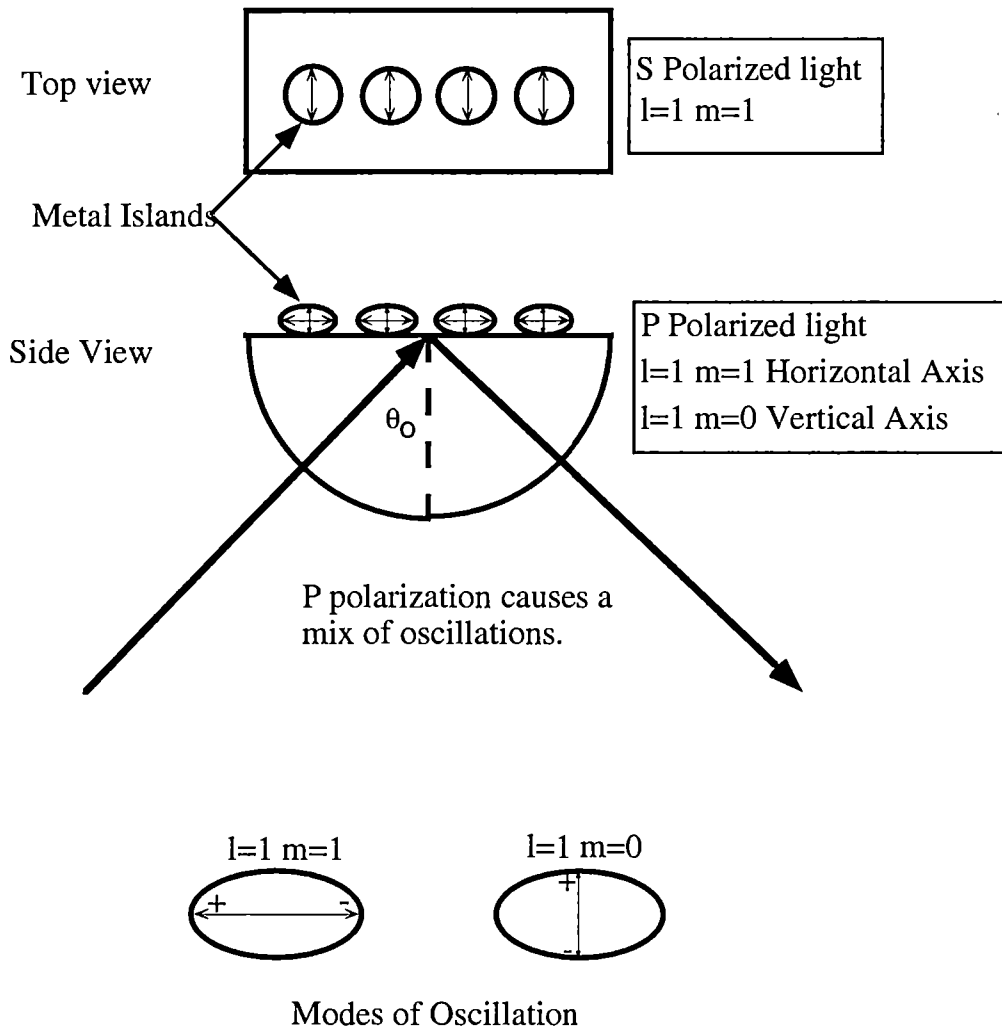


Figure 2.12: Shape of gold islands on a substrate. The $l=1$, $m=1$ case refers to the oscillations along the horizontal axis while the modes corresponding to $l=1$, $m=0$ case are oscillations along the vertical axis.

where P_{lm} , Q_{lm} , are Legendre functions, Y_{lm} are spherical harmonics and A_{lm} , B_{lm} are coefficients determined from the boundary conditions.

In solving this problem it is assumed that the spheroid is much smaller than the wavelength of the incident light. By making this assumption a dipole approximation can be used which means that the problem becomes a dielectric oblate spheroid in a time varying but uniform electric field. This small size also means that non-retarded, static electrodynamics can be used to solve the problem.

Next the boundary condition, inside and outside

$$V_{in, \eta=\eta_0} = V_{out, \eta=\eta_0} \quad [2.2.3]$$

$$\epsilon(\omega)\vec{n} \cdot \vec{\nabla}V_{in} |_{\eta=\eta_0} = \epsilon_{out}\vec{n} \cdot \vec{\nabla}V_{out} |_{\eta=\eta_0} \quad [2.2.4]$$

the spheroid must be met, where η_0 is the surface of the spheroid, ϵ_{out} is the dielectric function around the spheroid, and $\epsilon(\omega)$ is the dielectric function inside the spheroid.

Solving this equation and matching the boundary conditions leads to the dipole resonance condition given by

$$\frac{\epsilon_{1,m}}{\epsilon_{out}} = \frac{P_{1,m}(i\eta_0)}{Q_{1,m}(i\eta_0)} \frac{\left[\frac{dQ_{1,m}(i\eta)}{d\eta} \right]_{\eta=\eta_0}}{\left[\frac{dP_{1,m}(i\eta)}{d\eta} \right]_{\eta=\eta_0}} \quad [2.2.5]$$

where

$$\eta_0 = \frac{R}{\sqrt{1-R^2}} \quad [2.2.6]$$

is the shape parameter and R is the ratio of the minor to major axis length.

$$\epsilon_{11} = \epsilon_{\text{out}} \left(1 - \frac{2}{\eta_o(1 + \eta_o^2) \cot^{-1} \eta_o - \eta_o^2} \right) \quad [2.2.7]$$

$$\epsilon_{10} = \epsilon_{\text{out}} \left(1 - \frac{1}{(1 + \eta_o^2)(\eta_o \cot^{-1} \eta_o - 1)} \right) \quad [2.2.8]$$

There are two resonance modes for the shape dependent dielectric function, which correspond to excitations along the major and minor axes of the spheroid. In the dipole approximation only the $l=0$ and $l=1$ terms are important. The $m=0$ mode corresponds to a dipole resonance along the minor axis while $m=1$ corresponds to a resonance along the major axis and $l=1$ for both cases.

Peaks (resonance) in the absorption for a particle will be located where the real part of the experimentally determined dielectric function⁴⁰ (for gold in this case) equals the theoretical predictions.

$$\text{Re } \epsilon(\omega) = \epsilon_{\text{im}}(i\eta_o) \quad [2.2.9]$$

Resonance positions are displayed in Fig. 2.13 as a function of R , the ratio of the minor to major axis length, versus wavelength. The real parts of the dielectric response function are determined from bulk optical data⁴¹. The figure (Fig. 2.13) shows a branch for the minor axis ($l=1$ $m=0$) and a branch for the major axis ($l=1$ $m=1$) that converge as the ratio approaches one. This indicates that the absorption spectrum should contain two absorption peaks that will converge as the particle's shape becomes more spherical.

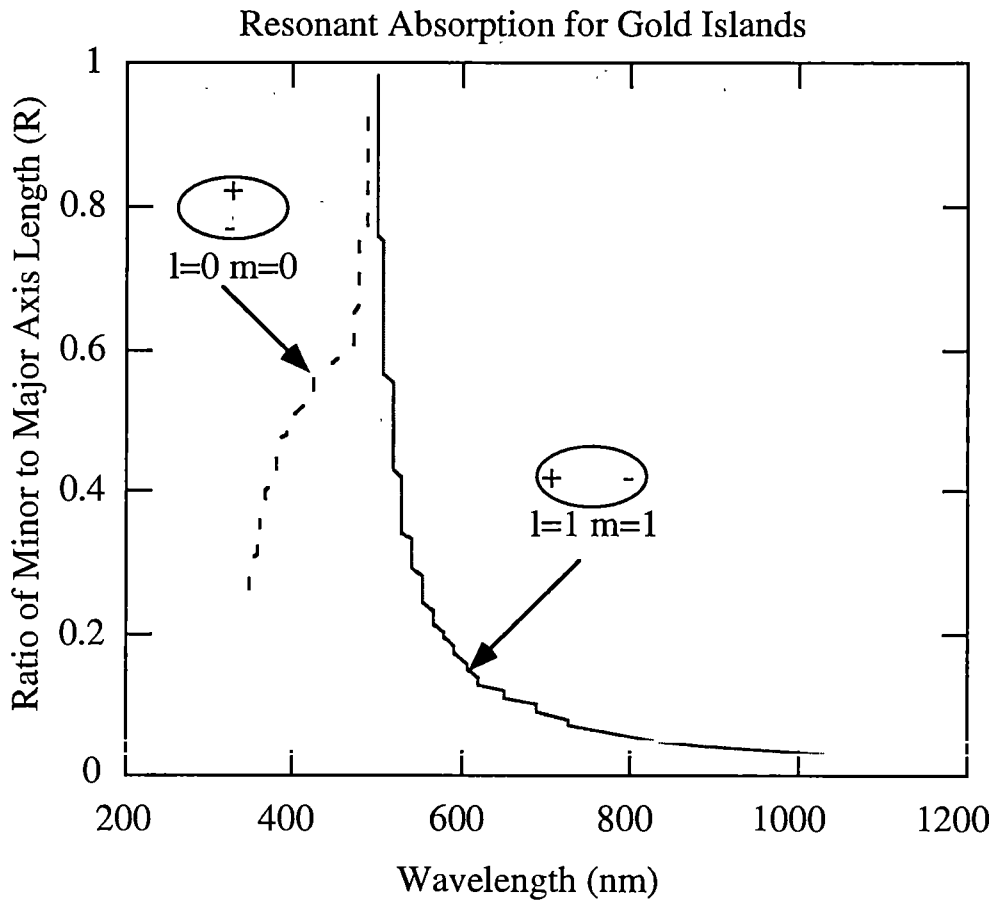


Figure 2.13: Absorption modes for gold particles along the minor and major axis. The solid line plots the resonance condition for the $l=1, m=1$ mode and the dashed line is for the $l=1, m=0$ mode. The position for the peak absorbance for each shape is shown. Dielectric function = 1, Angle of Incidence = 47°

The dipole moments for the spheroids can also be found from the solution to Laplace's equation and can be shown to be

$$\tilde{p}_x = \frac{2a^3(1 + \eta_0^2)^{1/2}[\epsilon(\omega) - 1]}{3Q_{11}(i\eta_0)[\epsilon(\omega) - \epsilon_{11}(i\eta_0)]} \tilde{E}_x(\omega) = \alpha_x \tilde{E}_x \quad [2.2.10]$$

$$\tilde{p}_y = \frac{2a^3(1 + \eta_0^2)^{1/2}[\epsilon(\omega) - 1]}{3Q_{11}(i\eta_0)[\epsilon(\omega) - \epsilon_{11}(i\eta_0)]} \tilde{E}_y(\omega) = \alpha_y \tilde{E}_y \quad [2.2.11]$$

$$\tilde{p}_z = \frac{-a^3\eta_0[\epsilon(\omega) - 1]}{3Q_{10}(i\eta_0)[\epsilon(\omega) - \epsilon_{10}(i\eta_0)]} \tilde{E}_z(\omega) = \alpha_z \tilde{E}_z \quad [2.2.12]$$

where α_x , α_y , α_z are the polarizabilities of the spheroid along the three different axes.

The total cross sections for p and s polarization are given by

$$\sigma_{\text{tot},s} = \frac{4\pi\omega}{c} \text{Im}(\alpha_x) \quad [2.2.13]$$

$$\sigma_{\text{tot},p} = \frac{4\pi\omega}{c} \text{Im}(\alpha_y \cos^2 \theta + \alpha_z \sin^2 \theta) \quad [2.2.14]$$

The scattering cross section is given by

$$\sigma_{\text{scatt},s} = \frac{8\pi\omega^4}{3c^4} |\alpha_x|^2 \quad [2.2.15]$$

$$\sigma_{\text{scatt},p} = \frac{8\pi\omega^4}{3c^4} (|\alpha_y|^2 \cos^2 \theta + |\alpha_z|^2 \sin^2 \theta) \quad [2.2.16]$$

and the absorption cross section (σ_a) is defined as total cross section minus the scattering cross section.

Light incident (I_o) upon a spheroid can be transmitted (I_t), scattered (I_{scatt}), or absorbed (I_a). Therefore,

$$I_o = I_t + I_{scatt} + I_a \quad [2.2.17]$$

which can be algebraically converted into

$$\frac{I_o}{I_t} = \frac{1}{1 - \left(\frac{I_{scatt}}{I_o}\right) - \left(\frac{I_a}{I_o}\right)} \quad [2.2.18]$$

where this is related to the single spheroid cross sections by

$$\frac{I_{scatt}}{I_o} = N\sigma_{scatt,p} \quad \frac{I_a}{I_o} = N\sigma_{a,p} \quad [2.2.19]$$

where N is the number of spheroids per unit area. This leads to

$$\frac{I_o}{I_t} = \frac{1}{1 - N\sigma_{tot}} \quad [2.2.20]$$

Since absorption is defined as $-\log(I_t/I_o)$, absorption as a function of the total cross section and density of particle is given as

$$ABS = \log\left[\frac{1}{1 - N\sigma}\right] \quad [2.2.21]$$

These equations combined with the experimental bulk dielectric for gold can be used to calculate the absorption peak for the islands. The Mathcad^{®42} Program was used to produce plots for different shapes of particles and for different dielectrics.

An example of the scattering cross section for gold islands of different shapes is given in Fig. 2.14. The p-polarization and the s-polarization are shown for both shapes and the cross section for the s-polarization is always larger. This is expected because the variation in the angle of incidence does not affect the effective size of the particle observed by the s-polarized light. The effective size of the particles for p-polarized light depends on the angle of incidence.

When the scattering cross section is compared to the absorption cross section one finds that the scattering cross section is proportional to the volume of the particle squared divided by the wavelength, of the incident light, to the fourth power while the absorption is proportional to volume of the particle divided by the wavelength of the incident light.²⁰ For particles with a major axis of 100nm the absorption cross section is on the order of 100 times larger than the scattering cross section. This is important to note because it indicates that the scattering signal from a sample's surface should be much less than the tunneling signal.

In Fig. 2.15 the scattering cross-section for s-polarized light is given as a function of the shape parameter, η . As η goes to infinity the particle approaches that of a sphere. The cross sections are for specific wavelengths of light. It is important to note that the particle's major axis length does not change, therefore as the particle approaches a sphere its volume increases.

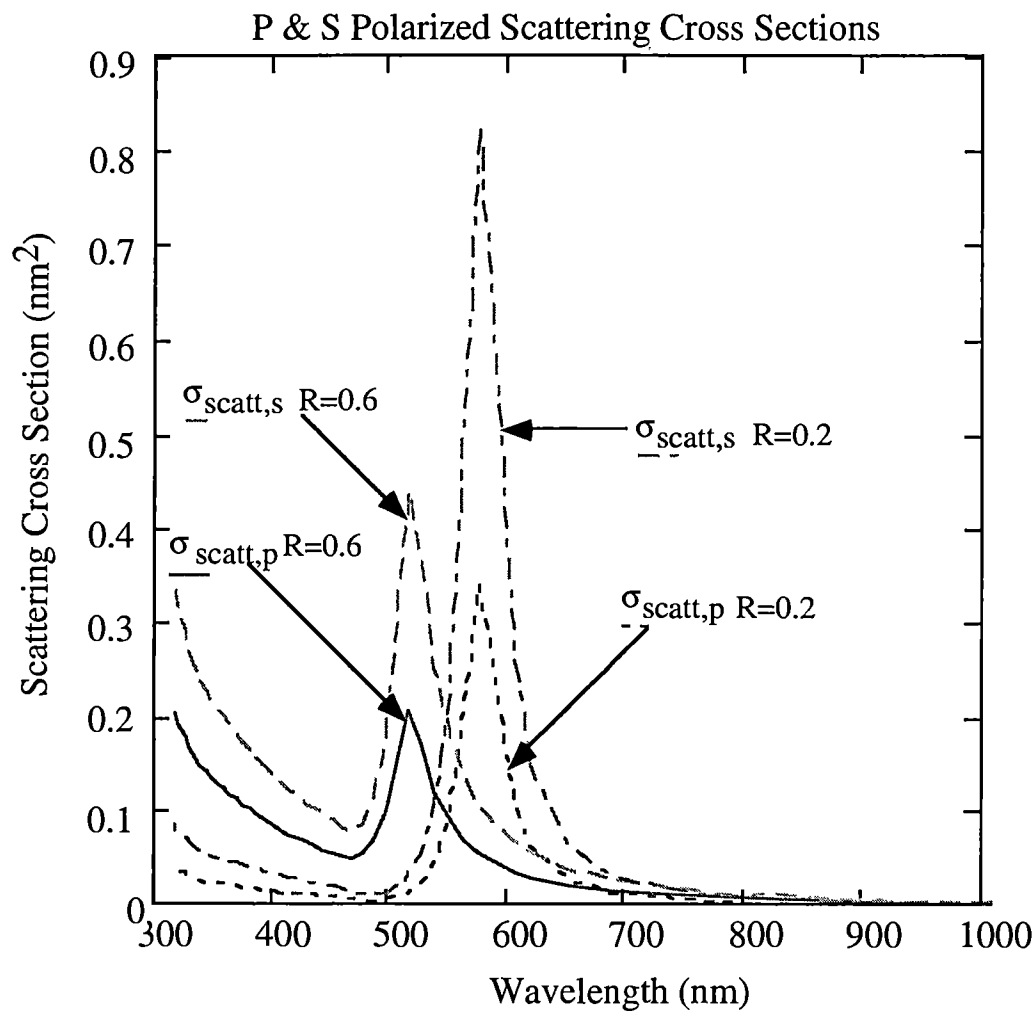


Figure 2.14: The scattering cross sections (nm²) for two particles (shapes R=0.2 and 0.6) embedded in a dielectric ($\epsilon=1.0$) with a major axis length of 30 nm for light incident at an angle of 50°. The s-polarization scatter cross section (subscript s) is larger than the p-polarization cross section (subscript p).

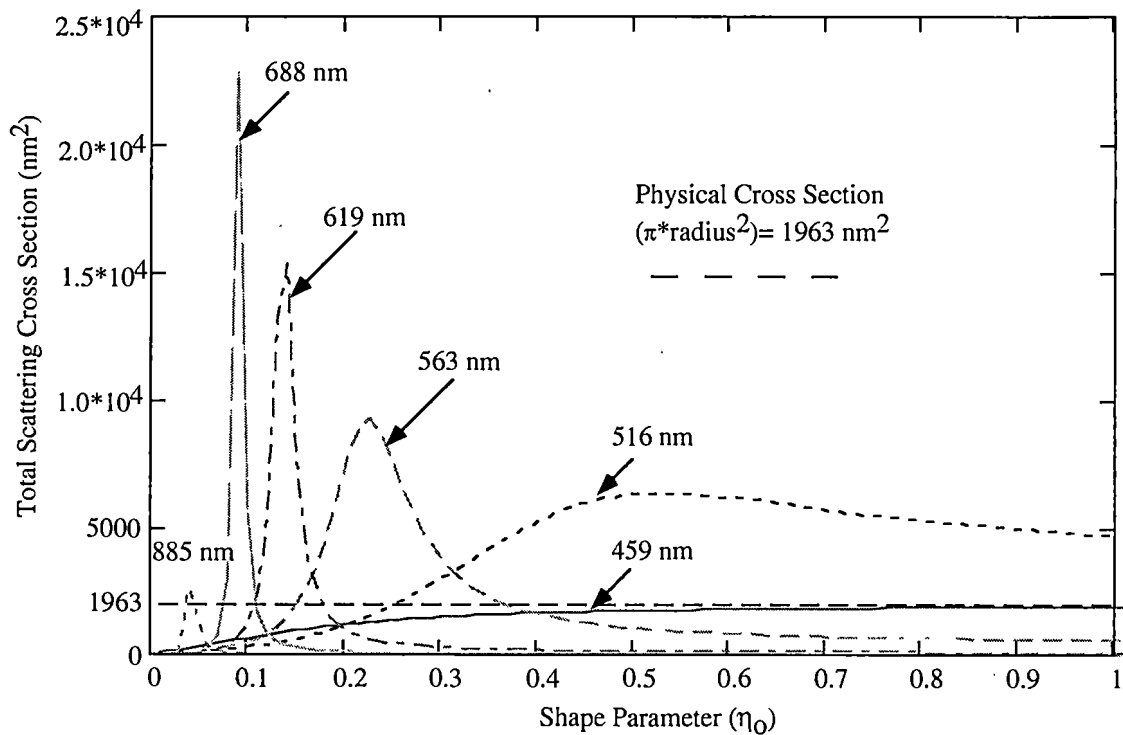


Figure 2.15: The total cross section for different wavelength of s-polarized light is given as a function of the shape parameter η . As η goes to infinity the particle approaches that of a sphere. The cross sections are for specific wavelengths of incident light. One thing to note is that the particle's semi-major axis length does not change, therefore as the particle approaches a sphere it's volume increases. Dielectric Constant (ϵ) = 1, Angle of Incidence (θ) = 47° , Semi-major axis length = 50 nm

2.2.2 Gaussian Distribution of Particles

It has been demonstrated through experimental imaging of gold islands and through previous experiments⁴³ that the particles created on the substrate have an approximately "Gaussian" distribution of particle shapes that are centered on a particular particle shape (R_0). Thus far the theory only describes the absorption and scattering for a single particle. This single particle theory needs to be modified to take into account multiple scattering centers. To accomplish this modification the absorption for all of the particle shape parameters is calculated and applied to a "Gaussian" distribution that is centered on a particular particle shape (R_0). Absorption is given by

$$\text{Abs} = - \sum_{R=0}^1 \log_{10}[1 - N\sigma f(R)] \quad [2.2.22]$$

$$\text{where } N = \frac{N_0 f(R)}{\cos\theta} \text{ and } f(R) = \frac{\exp\{-[\frac{(R_0 - R)^2}{2R_s^2}]\}}{\sum_{R=0}^1 f(R)}. \quad [2.2.23]$$

N_0 is the number of particles per unit area at normal incidences to the surface while N is the number of particles at a given angle of incidence. $f(R)$ is a "Gaussian" distribution of particle shapes centered at R_0 , with the distribution around R_0 determined by R_s . The absorption for a "Gaussian" distribution of gold particles with different shapes is shown in Fig. 2.16.

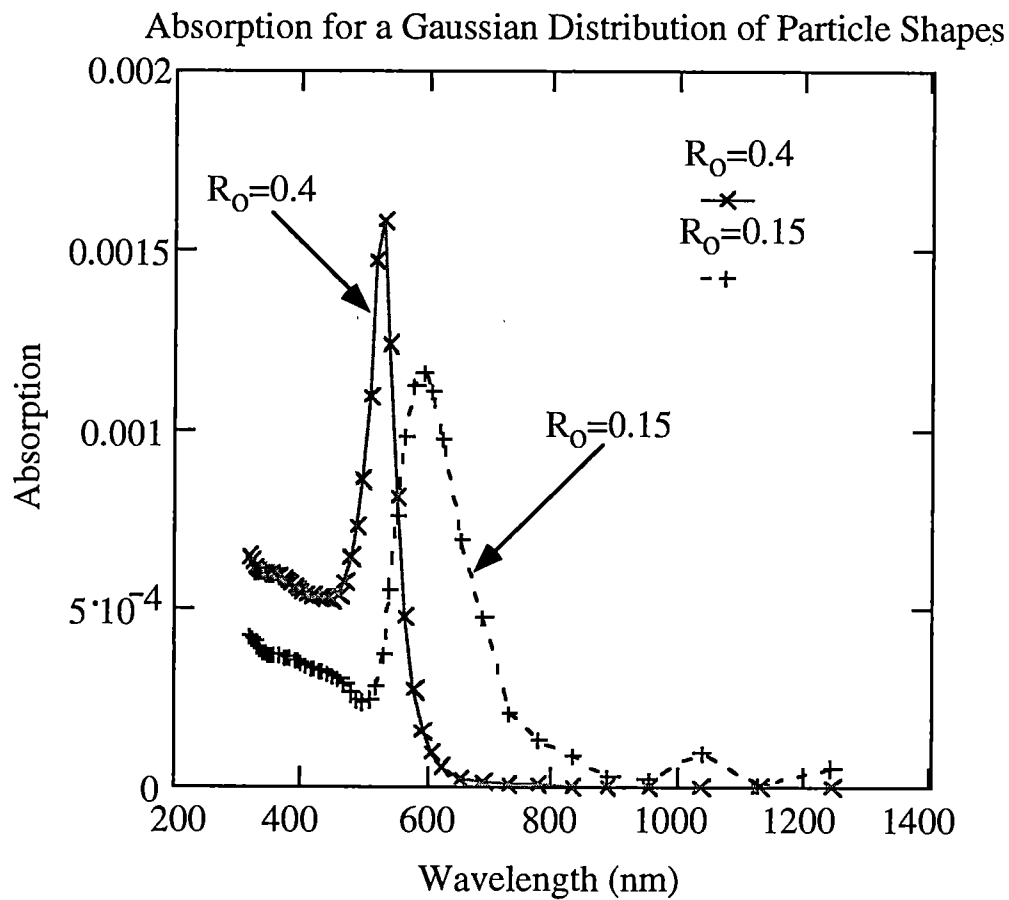


Figure 2.16: Absorption peak for a "Gaussian" distribution of gold island particles embedded in a dielectric ($\epsilon=1.3$). The major axis length of the particles is 30 nm and the light is incident from an angle of 50° . ($R_o=0.4$ and 0.15), $R_s=0.1$, $N_o=10^4$)

The substrate and dielectric around the particle will also affect the absorption peak by causing a red shift in the surface-plasmon energy.⁴⁴ If the substrate causes a shift in the absorption peak, then the presence of the tip should also distort the peak in the red direction contributing to the approximate dielectric function around the island. Red shifting from the presence of the tip is much smaller than the affect of the substrate. The presence of the tip also distorts the electric field by causing tunneling to occur.

In the figures and calculations dielectric constants were chosen to take into account the substrate affect. For simplicity, the dielectric used is assumed to be an average of the dielectric constant of the substrate and air.

2.3 NSPM (Nonlinear Scanning Probe Microscope)

While a NSPM incorporates many of the same theoretical models as the PSTM it is quite different due to the use of two-photon sensing in the near zone of a sample. In NSPM the excitation light is incident upon the sample under TIR conditions and the topographical imaging works via the tunneling process. The difference occurs in the fluorescence excitation process. In NSPM a metal-coated fiber probe is used to enhance the electric field of the incident field so that the fluorophore is excited by a two-photon absorption. In this way a photon of energy much lower than the energy level difference can be used to move an electron from the ground state of a fluorophore molecule to an excited state.

2.3.1 Interaction of Light with Molecules.

When a photon of light is incident upon a molecule it can be absorbed or scattered. Scattering involves the photon being emitted from the molecule almost immediately with little change to the incident beam. During absorption the photon energy is held in the molecule for a period of time before it is released, if it is released. Light will only be absorbed by a molecule if the energy of the photon corresponds to the energy needed to change the electronic configuration of the molecule, the vibrational energy, or the rotational energy. The vibrational energy is related to changes in the average internuclear distances while rotational energy is a change in the way the molecule rotates about its center of gravity. These energy states are normally activated by energy levels in the infrared region of the spectrum and are much lower in energy than the change in electron configuration. The change in electron configuration corresponds to the transition of an electron from a ground state to an excited state. The electronic energy levels are divided into many sub levels that correspond to vibrational and rotational energy changes.

When energy is lost from absorption much of it is lost in the form of heat. Some of it will be emitted through radiated energy. Luminescence is a general term used to describe the loss of absorbed energy through the emission of a photon. Fluorescence and phosphorescence are two types of luminescence. The difference between them is the time the energy is stored. In fluorescence the transition back to the ground state energy occurs after a nanosecond or a microsecond while phosphorescence has a delay of 10^{-4} to 10 seconds or longer in some cases.

2.3.2 Fluorophores

As previously mentioned fluorophores are molecules that undergo fluorescence and are commonly used as probes in biological experiments. Fluorescence is a process in which a photon is absorbed and excites an electron from the ground state of a molecule to a real excited state where the electron remains temporarily ($\sim 10^{-9}$ sec) before returning to the ground state. When the electron returns to the ground state a photon is emitted with an energy corresponding to the energy difference ($E=h\nu$) between the states. The emitted energy is normally less than the energy of the absorbed photon because of energy lost to vibration/rotation of the molecule and energy lost in collisions with other molecules while in the excited state. This energy loss is called the Stokes shift. The Stokes shift is advantageous in studying cells, or other materials, which have been marked with fluorophores because the excitation and fluorescence peaks do not overlap in the spectrometer.

2.3.3 Two-Photon Excitation

The process of two-photon excitation is a type of nonlinear process in which the electric field intensities of higher orders play a dominant role. Many applications are starting to use nonlinear optical effects⁴⁵. Spectroscopists use this effect to double the frequency of lasers, biologist use it to look at tagged biological samples, and others use it in developing medical applications⁴⁶.

In this experiment the two-photon effect was used in the excitation of fluorophores. A fluorescent molecule was induced to fluoresce using photons of much lower

frequency than is ordinarily required by using a high intensity and thereby causing a nonlinear coupling. One photon of the excitation light is not energetic enough to raise a molecule from its ground state to an excited state. Two excitation photons must be absorbed and the electron passes through a virtual state. (Fig. 2.17) The energy of the two separate photons equals the energy of the difference between the energy states. This only occurs in the highest intensity region of a beam.

Electromagnetic theory demonstrates that polarization is related to the electric field

$$\mathbf{P} = \epsilon_0 \chi \mathbf{E} \quad [2.3.1]$$

where ϵ_0 is the dielectric constant and χ is the dimensionless electric susceptibility.

If a molecule is placed in a sufficiently intense uniform electric field \mathbf{E} then the induced dipole moment \mathbf{P} is no longer simply proportional to \mathbf{E} . Rather, there is also a quadratic dependence upon the electric field. This can be seen by expanding the polarization in a series expansion.

$$\mathbf{P} = \epsilon_0 (\chi \mathbf{E} + \chi_2 \mathbf{E}^2 + \chi_3 \mathbf{E}^3 + \dots) \quad [2.3.2]$$

The linear susceptibility (χ) is much larger than the coefficients of the nonlinear terms (χ_2, χ_3, \dots). Only at higher electric field strength do the nonlinear terms come into play. The value of at least one component of \mathbf{E} must therefore be sufficiently large so as to compensate for the smallness of the quadratic coefficients. The

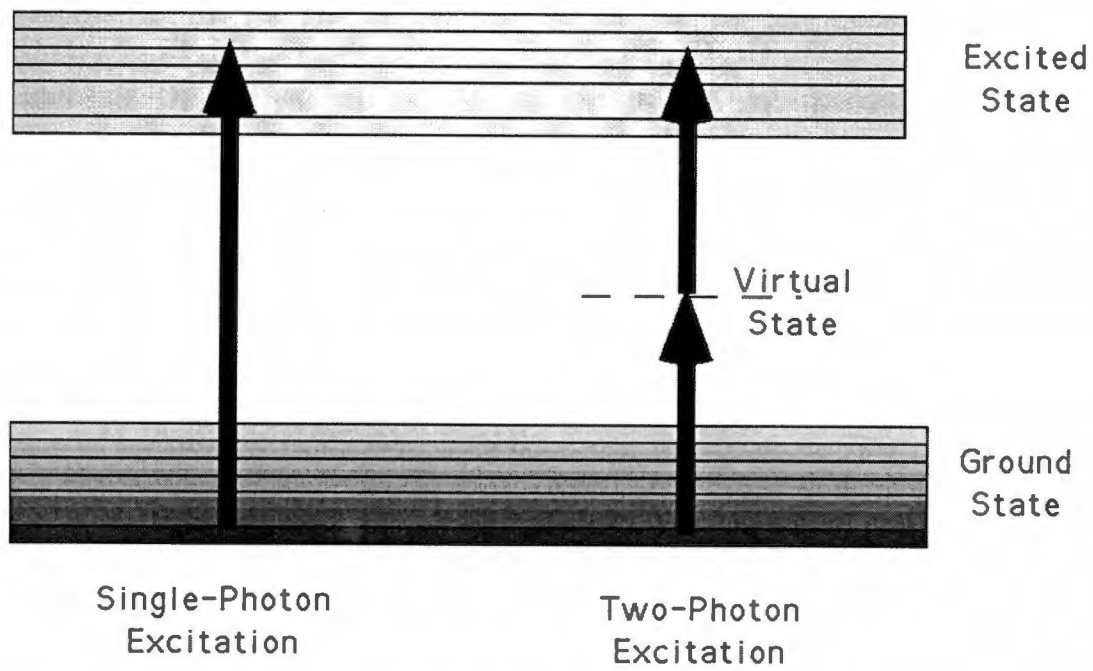


Figure 2.17: Diagram of the excitation of an electron from a ground state to an excited state for one-photon and two-photon absorption.

electromagnetic radiation emitted as a result of a significant nonlinear polarizability has a portion that has twice the frequency of the incident field \mathbf{E} .

Assume light takes the form of

$$\mathbf{E} = E_0 \sin \omega t \quad [2.3.3]$$

Then the polarization takes the form

$$P = \epsilon_0 \chi E_0 \sin \omega t + \epsilon_0 \chi_2 E_0^2 \sin^2 \omega t + \epsilon_0 \chi_3 E_0^3 \sin^3 \omega t + \dots \quad [2.3.4]$$

which can be rewritten as

$$P = \epsilon_0 \chi E_0 \sin \omega t + \frac{\epsilon_0 \chi_2}{2} E_0^2 (1 - \cos 2\omega t) + \frac{\epsilon_0 \chi_3}{4} E_0^3 (3 \sin \omega t - \sin 3\omega t) + \dots \quad [2.3.5]$$

The second term in this equation shows higher order frequencies--doubled light (2ω). This occurs in classical terms because of the influence of a quadratic upon the Fourier components of the field. In quantum terms, two photons are absorbed in an electronic transition to produce emission of a single photon of equal *total* energy upon de-excitation of the electron. This term indicates that the charges in the substance are being driven at twice the frequency and will reradiate at this frequency. This reradiated, doubled light, is defined as Second Harmonic Generation (SHG).

"In terms of the photon representation we can envision two identical photons of energy $\hbar\omega$ coalescing within the medium to form a single photon of energy $\hbar 2\omega$. Peter A Franken and several coworkers at the University of Michigan in 1961 were the first to observe SHG experimentally. They focused a 3-kW pulse of red (694.3nm) rube laser light onto a quartz crystal. Just about one part in 10^8 of this incident wave was converted to the 347.15 nm ultraviolet second harmonic." ⁴⁷

Pulsed light is more effective for generating SHG signals because the short pulse length increases the intensity of the light delivered. Since power is energy divided by time, as the time frame decreases the power level delivered increases.

A metal-coated probe can be used to stimulate the high field intensities needed for generating SHG affects. SHG needs a threshold of incident intensity and a metal-coated probe will help concentrate the electric field effectively. It is well known that a sharpened metal probe concentrates charges near the metallic tip, which is sometimes called " the lightning rod effect". A schematic of this effect is shown in Fig. 2.18.

By using this field enhancement effect fluorophores can be excited and located with high resolution. The primary drawback is that a fluorophore will chemically decay following emission of approximately one million photons and the image might not be acquired before the decay. It would be desirable to stimulate the nonlinear process only at the moment of signal acquisition. The field enhancement effect will allow this by only exciting the fluorophore directly beneath the probe tip.

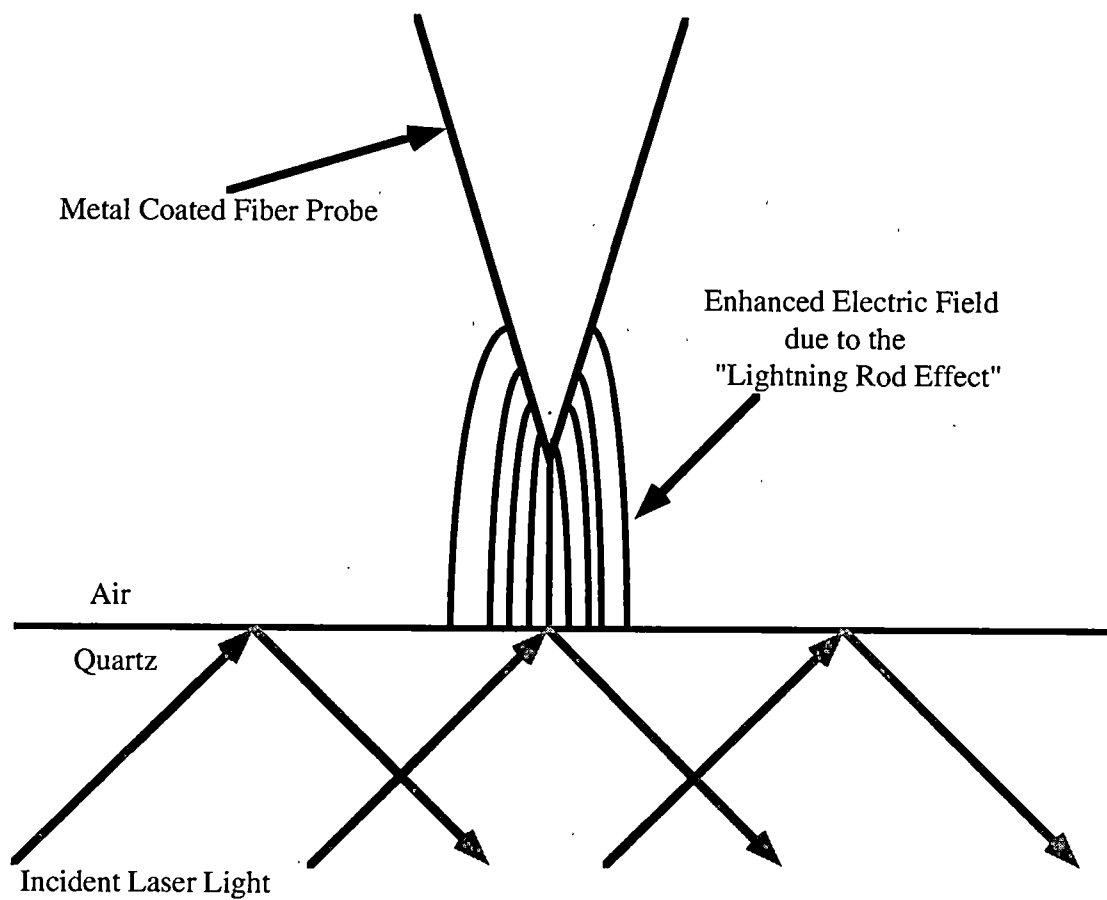


Figure 2.18: Example of the field enhancement due to a sharpened metal probe tip.

2.4 Distance to Surface Calculations

2.4.1 Calculation for General Function.

The ability to calculate the distance from the surface in optical probe microscopy is very important. It is possible to determine this distance from a calculation that involves the transmission functions of different wavelengths of light incident at the same angle. In Fig. 2.10 the tunneling signal for different wavelengths of light is shown to vary as a function of the sample to probe separation distance.

To calculate the distance to the surface one first assumes a general transmission function that takes the form

$$T = T(\xi) \quad \text{where} \quad \xi = \frac{2\pi}{\lambda}z \quad \text{and } \lambda \text{ stands for wavelength.}$$

The chain rule is used to calculate the derivative of the transmission function with respect to wavelength (λ) and then with respect to distance (z) from the surface.

$$\frac{dT}{d\lambda} = \frac{dT}{d\xi} \frac{d\xi}{d\lambda} = \frac{dT}{d\xi} \left(-\frac{2\pi z}{\lambda^2} \right) \quad [2.4.1]$$

$$\frac{dT}{dz} = \frac{dT}{d\xi} \frac{d\xi}{dz} = \frac{dT}{d\xi} \left(\frac{2\pi}{\lambda} \right) \quad [2.4.2]$$

The results of these derivatives can be combined to give

$$\frac{\frac{dT}{d\lambda}}{\frac{dT}{dz}} = -\frac{z}{\lambda} \quad [2.4.3]$$

This can then be approximated as

$$z = -\frac{\Delta I_{\lambda}}{\Delta \lambda} \frac{\Delta z}{\Delta I_z} \lambda \quad [2.4.4]$$

where Δ stands for differences in measurements and the intensity of light measured and (I) replaces the transmission function. The above neglects the probe curvature effects that cause an additional z dependence of the signal as one moves laterally.

2.4.2 Theoretical Predictions of Distance to Surface

Predictions of the distance to surface were calculated from theoretically generated data sets based on the truncated cone approximation transmission data for different wavelengths of light. The intensities were put into the delta I, delta lambda, delta z positions of the distance to surface formula (Eq. [2.4.4]).

In Fig. 2.19 the distance calculations for theoretically generated data are shown for the difference in intensity between a 633 nm beam and a 544 nm beam. The data set uses λ as 633 nm and λ as 544 nm for the different calculations. The calculated distance is not very accurate close to the surface because of the difference in transmission to a cone for different wavelengths. These differences in transmission are due to the shape of the tip and cause an offset in the distance calculation.

Fig. 2.20 shows the results of the same calculation after the intensities have been normalized to the intensity closest to the surface for each wavelength. The normalization removes the differences in transmission that are caused by the shape of

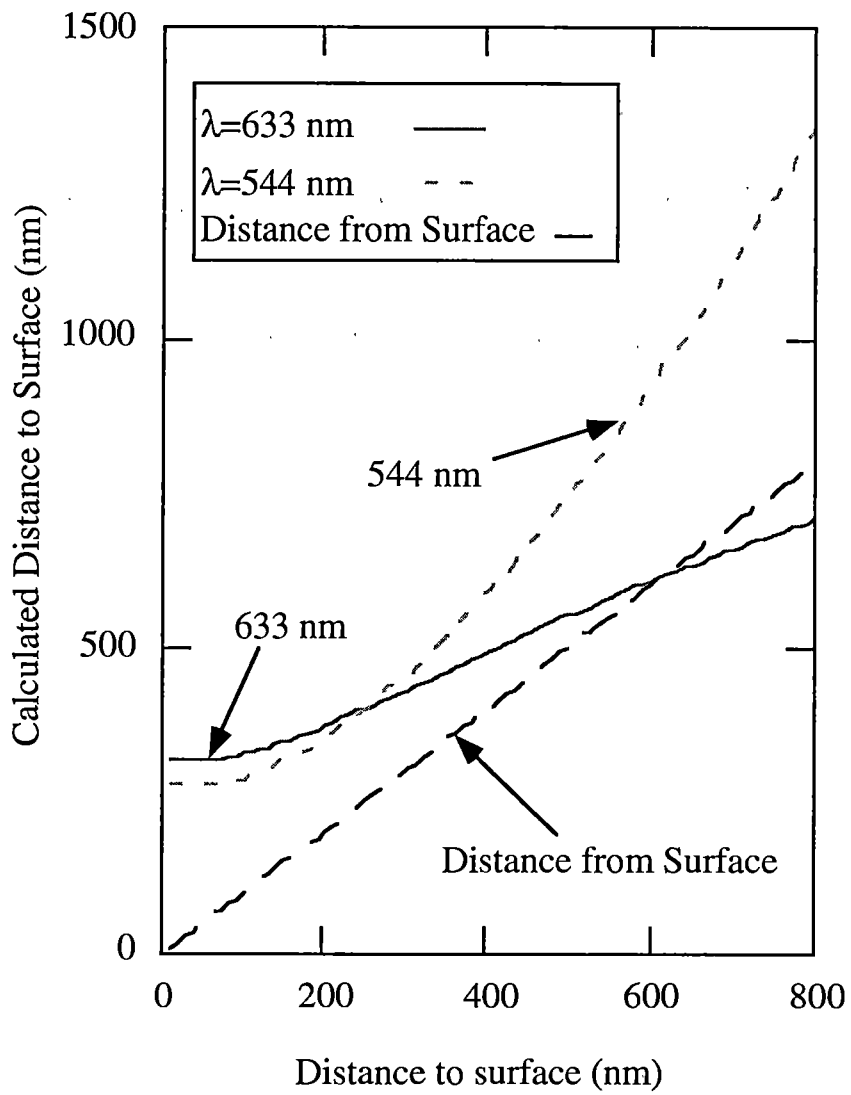


Figure 2.19: Distance to the surface calculation results that are based on unnormalized theoretically generated data sets for 633 nm and 544 nm.

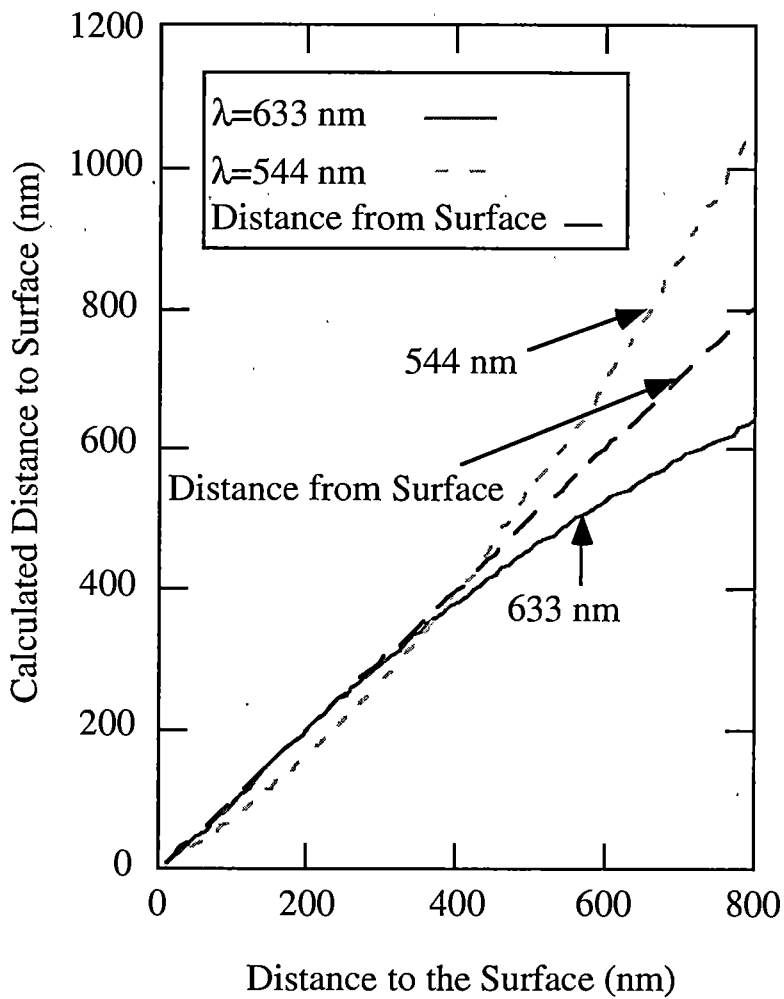


Figure 2.20: Distance to the surface calculation results that are based on normalized theoretically generated data sets for 633 nm and 544 nm.

the probe. The differences in transmission are now only due to the differences in the tunneling signal as the probe is moved toward the surface. Under this approximation the calculated values are a more accurate representation of the actual distance to the surface very close to the surface and then start to diverge at larger distances. The divergence at larger distances is probably due to the large $\Delta\lambda$ used in the approximation, which causes the approximation to breakdown. When a smaller wavelength differential is used the divergence becomes much smaller as seen in Fig. 2.21 where the wavelengths are 620 nm and 630 nm. A comparison of the percent difference between the actual distance to the surface and the calculated distance for the 633 nm, 544 nm case and the 620 nm, 630 nm case are shown in Fig. 2.22. The high percent differences near the surface are a result of the small values and in absolute distance terms would not be very high.

The next case shown in Fig. 2.23 is that of data being normalized to a point (100 nm from the surface) that is not the maximum possible intensity. These are the same conditions as for Fig. 2.20 except for a change in the normalization point. Changing the normalization point shifts the distance calculations causing the distance to the surface approximation to be smaller than the actual values. The position where the calculated values cross zero is equal to the offset used for the normalization point. In Fig. 2.24 a constant term was added to the intensity values. This was done to simulate a constant scattered light background that exists in real data sets. The data was normalized to the highest intensity for each case and then the distance calculation

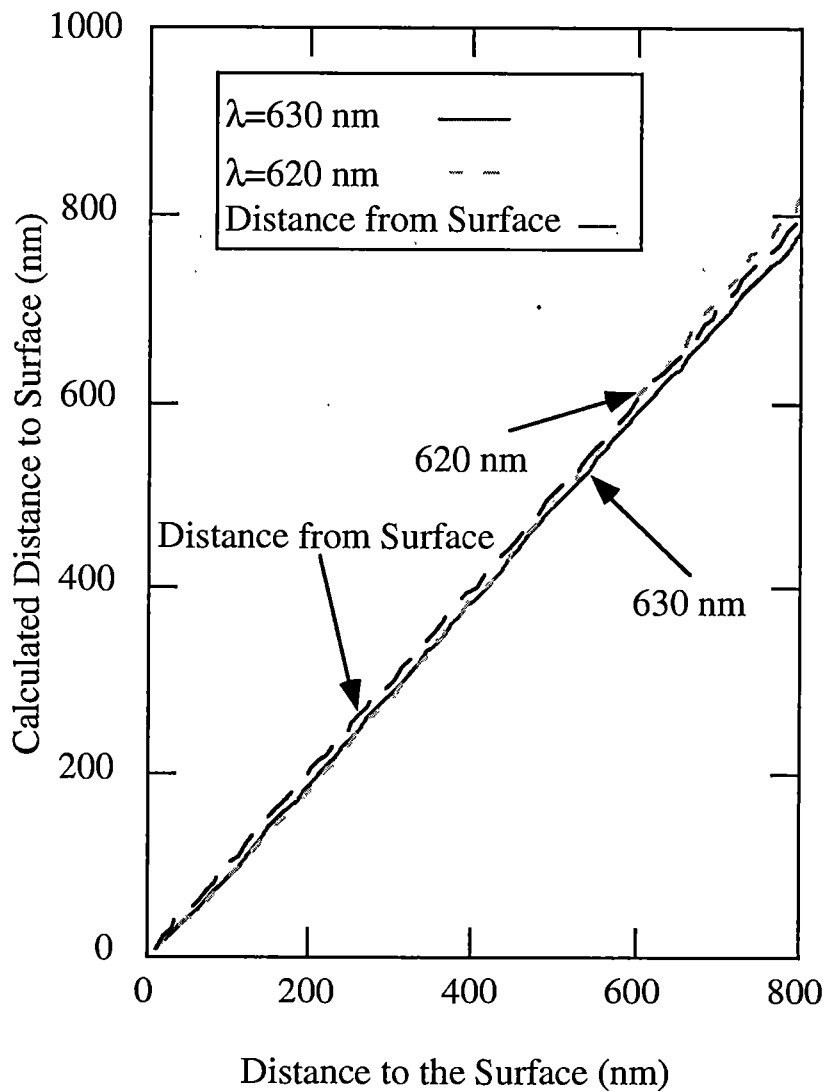


Figure 2.21: Distance to the surface calculation results that are based on unnormalized theoretically generated data sets for 630 nm and 620 nm.

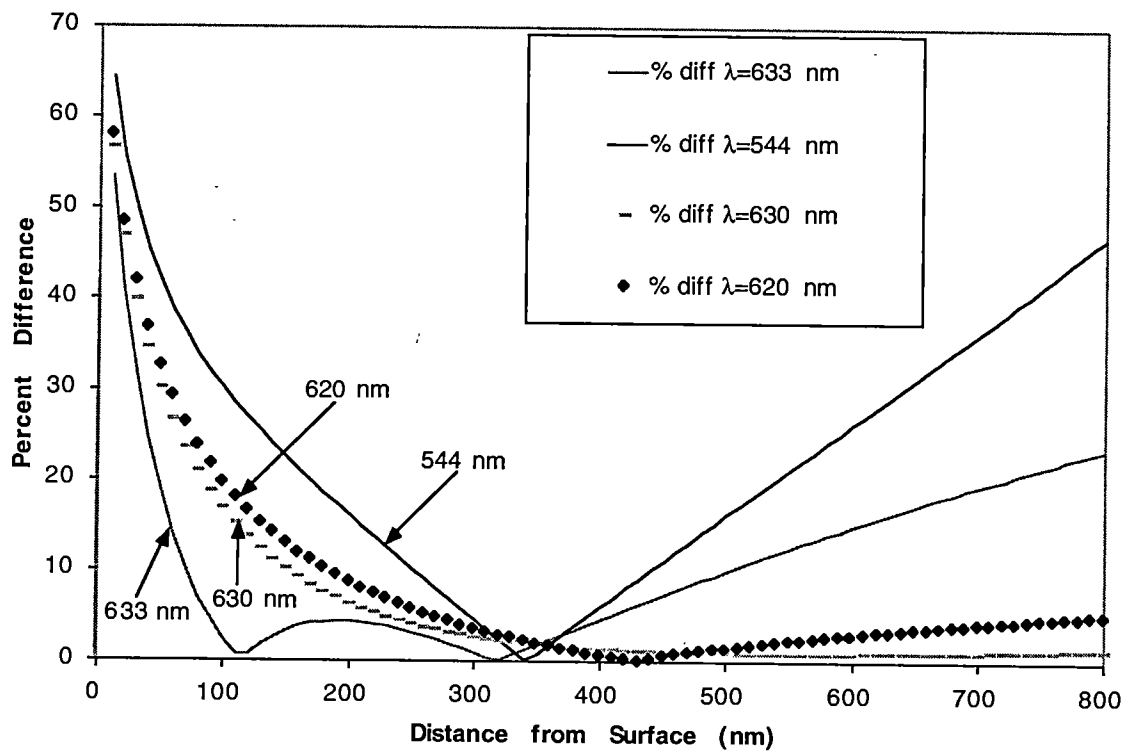


Figure 2.22: The percent difference between the actual distance from the surface and the approximated value for the 633 nm and 544nm case and the 630nm and 620 nm case.

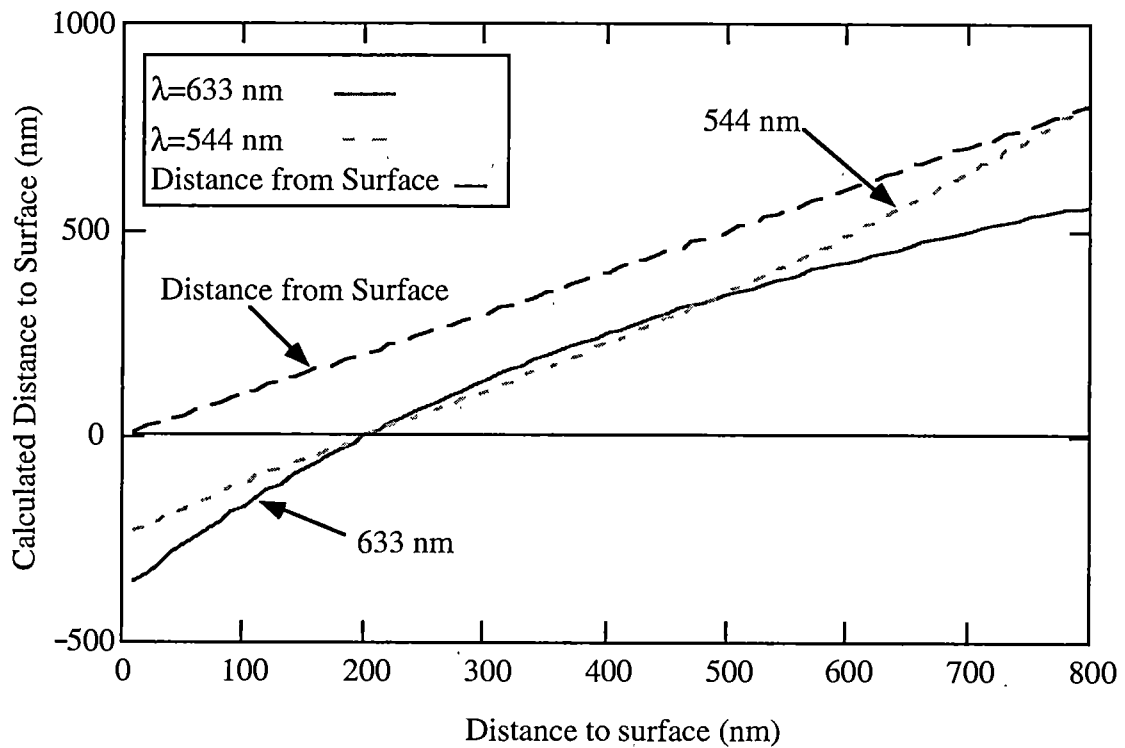


Figure 2.23: Distance to the surface calculation results that are based on data normalized at a point below the maximum for 633 nm and 544 nm. The normalization causes the distance calculations to be shifted.

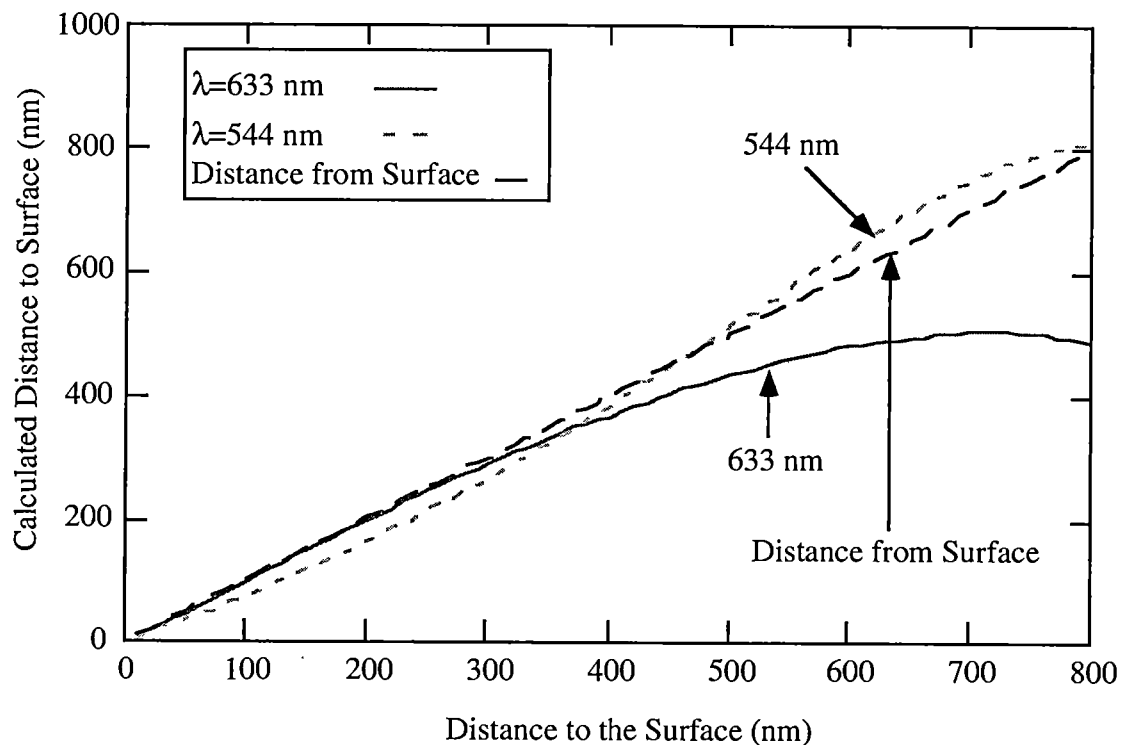


Figure 2.24: Distance to the surface calculation results that are based on data with a constant scatter term added normalized for 633 nm and 544 nm. A constant scatter term was added to the data. Then it was normalized to the highest intensity (at $z=1$) and the distances were calculated. The scattering begins to dominate the results away from the surface when the tunneling signal decreases.

was preformed. The scattering term does not affect the results until the intensity of the signal falls off. At this point the small intensity values are dominated by the constant scattering term. This can be seen where the distance measurements curve downward near 600 nm. When the normalization is not done to the point of greatest intensity the distance to the surface is shifted, as before, and is shown in Fig. 2.25.

This theoretical model presents the possibilities and suggests possible limitations in using this method to find the distance to the surface. The results indicate that a small difference in wavelengths is necessary to obtain accurate results. The results also indicate that the uniform field of scattered light should not change the results close to the surface. This theory still needs improvement and a parabolic model of the probe tip will be presented in the next section.

One method for overcoming the normalization condition would be to apply the theoretical intensity differences at the surface of the sample to experimental results to compensate for differences that are due to wavelength collection efficiencies of the probe tip.

2.4.3 Paraboloidal Probe Approximation

After analyzing the distance to the surface approximations one is lead to develop a better approximation for the shape of the probe tip to over come problems with normalization. The previous section demonstrated that the shift caused by normalization limits the usefulness of the distance to surface theory and the cone approximation. The breakdown occurs because of the difference in tunneling signals

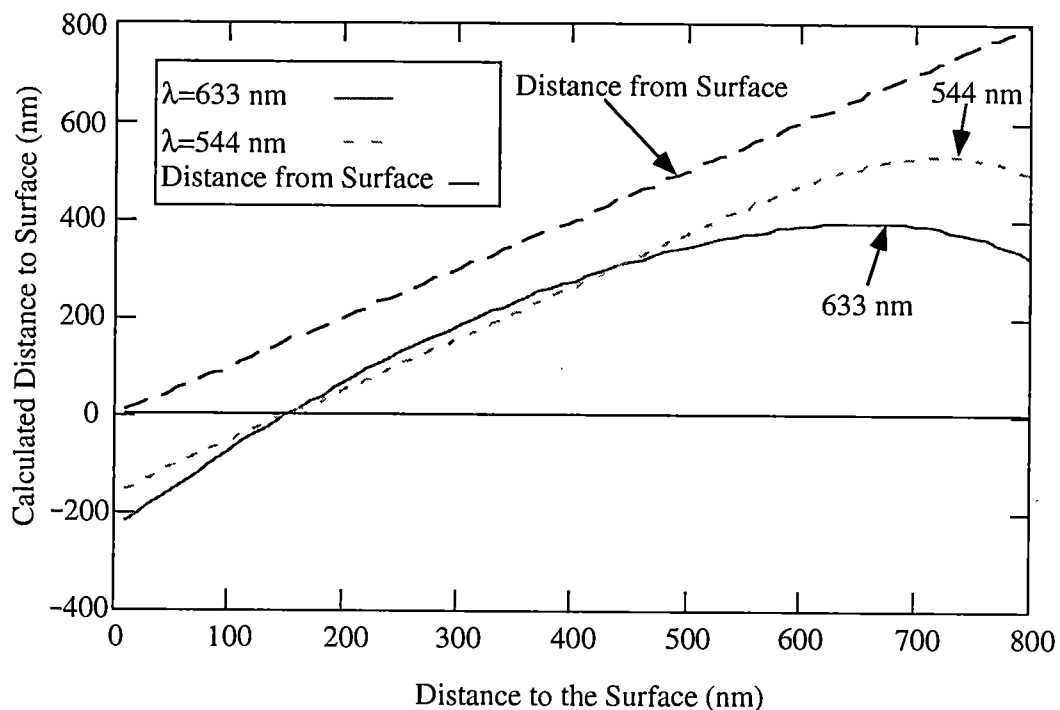


Figure 2.25: Distance to the surface calculation results that are based on data with a constant scatter term added normalized at a point below the maximum for 633 nm and 544 nm. The scattering term was normalized to the intensity at 200 nm from the surface which shifts the distance calculations.

for different wavelengths as the probe touches the surface of the sample. To improve upon the previous theory one can consider the case of a paraboloidal probe with the Cartesian coordinate equation

$$z = z_0 + \frac{R^2}{a} \quad [2.4.5]$$

where R is the radius in the xy plane. This case was treated by Reddick⁴⁸. The transmission is approximated by averaging the planar surface transmission coefficient over the probe cross section and dividing by the area A of the spot of the incident light. Thus, for the planar transmission coefficient across an air gap separating two quartz media, one has the standard result (for p-polarization)

$$T(z) = \frac{2 \sin^2 \bar{\alpha}}{[\cosh(2qz) - \cos 2\bar{\alpha}]} \quad [2.4.6]$$

where qz is b , $\bar{\alpha}$ is and

$$s^2 = n^2 \sin^2 \theta - 1 \quad [2.4.7]$$

The transmission is taken to be

$$\tau = \left(\frac{\pi}{A} \right) \int T(z) R(z) dR(z) \quad [2.4.8]$$

with the integration being from $z = z_0$ to infinity. For the paraboloid,

$$R dR = \left(\frac{a}{2} \right) dz \quad [2.4.9]$$

the integral can be done exactly. Substituting and solving for τ gives

$$\tau = \left(\frac{2\pi a \tan \bar{\alpha}}{qA} \right) \left\{ \left(\frac{\pi}{2} \right) - \tan^{-1} \left[\frac{(\exp(2qz_0) - \cos 2\bar{\alpha})}{\sin 2\bar{\alpha}} \right] \right\} \quad [2.4.10]$$

This equation demonstrates that $d\tau / d\lambda / d\tau / dz_0$ is indeed $-z/\lambda$. The hyperbolic cosine causes the decay of intensity with distance to be relatively slow near the surface in the planar case, but the dependence is more complicated here. At $z_0 = 0$ the transmission is not unity for this tip, but rather is proportional to wavelength. Note that the second term above becomes just $\bar{\alpha}$:

$$\tau \text{ (at touching)} = \left(\frac{2\pi a \tan \bar{\alpha}}{qA} \right) \left[\left(\frac{\pi}{2} \right) - \bar{\alpha} \right] \quad [2.4.11]$$

One should also note that the transmission has no inflection point, but rather decreases monotonically with increasing distance. The derivative of the transmission with respect to distance is

$$\frac{\left(\frac{2\pi a \tan^2 \bar{\alpha}}{A} \right)}{\left[2 \cosh(2qz_0) + \exp(-2qz_0) \cos^2 2\bar{\alpha} - 2 \cos 2\bar{\alpha} \right]} \quad [2.4.12]$$

which has no zero. The second derivative is zero at touching.

2.5 Probe Measures the Electro-Magnetic Cross Section.

The evanescent field may be viewed as uniform across the small thickness of a metal island. In this event, the dipole moment induced is given by Eq. [2.2.10] for s-polarized light. The electric field of the resulting induced dipole in the near zone is simply the gradient of the potential

$$\phi = p \cos\theta / r^2 \quad [2.5.1]$$

The resulting energy density outside the oblate spheroidal island is the absolute square of the sum of this field and the evanescent field. This can be referenced to the value of the evanescent field at the substrate surface at a point well away from the island laterally if there is a region that contains no other particles. In practice, this factor is not critical to the present considerations. Hence, it is expected that the PSTM will garner a flux from the energy density that contains a term proportional to the product of the inverse cube of distance from the center of the particle and the exponential spatial dependence of the evanescent field in this approximation, this term arising from the product of the fields when the energy density is calculated. The inverse sixth power term is not easily observed due to its rapid falloff. As the probe retracts, the inverse cube term also falls off, leaving only the evanescent field. A diagram of the probe interacting with the dipole field is shown in Fig. 2.26.

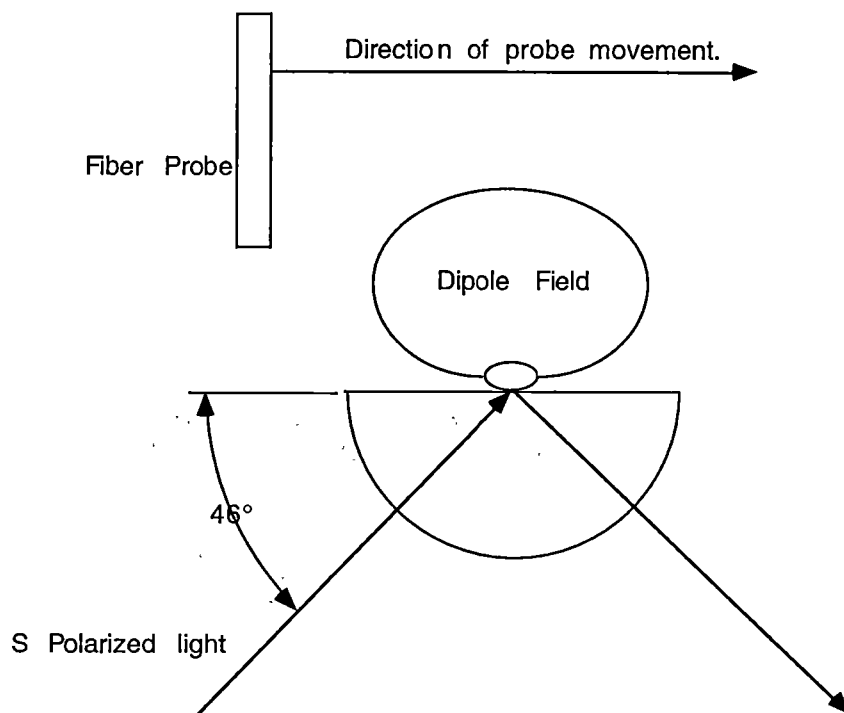


Figure 2.26: Schematic of the probe and a dipole field above a gold particle.

2.5.1 Summary of Theory

In summary this chapter presents the basic theory of reflection and refraction at an interface. A theoretical interpretation (model) for how the probe interacts with the sample surface and a method of distance to the surface is introduced. Also, the concept of two-photon excitation and the scattering and absorption associated with prolate spheroidal particles (gold islands) is described.

Chapter 3 Experimental Description

All forms of SPMs involve a probe being moved very close to a sample surface in a predetermined linear scanning pattern, normally called a raster pattern, which covers all of the area to be imaged. The probe is moved by a relatively hard piezoelectric crystal that is controlled by a computer and feedback electronics. In feedback mode the electronics maintain a constant current while a constant height mode keeps the probe at a set separation from the surface. At each point along the scan path measurements are taken, recorded and displayed on the computer screen. The composite image of the measured values at different points represents a topographical image map of the surface.

This chapter presents a description of the various pieces of equipment used during the experimental process. The experimental setup for the PSTM and NSTM consists of four major components: probe positioning, mechanical structures, illumination, and signal detection/analysis. A schematic of the positioning and signal detection components of the system is shown in Fig. 3.1. The other major part of the experimental work involves sample preparation and characterization.

3.1 Probe Positioning

The PSTM works by moving a sharpened fiber probe over the surface of a sample so that the evanescent field can be locally frustrated at each point. For this to be feasible a precision mechanism must be used to position the fiber probe close to the surface of the sample. There are two main components involved in positioning the

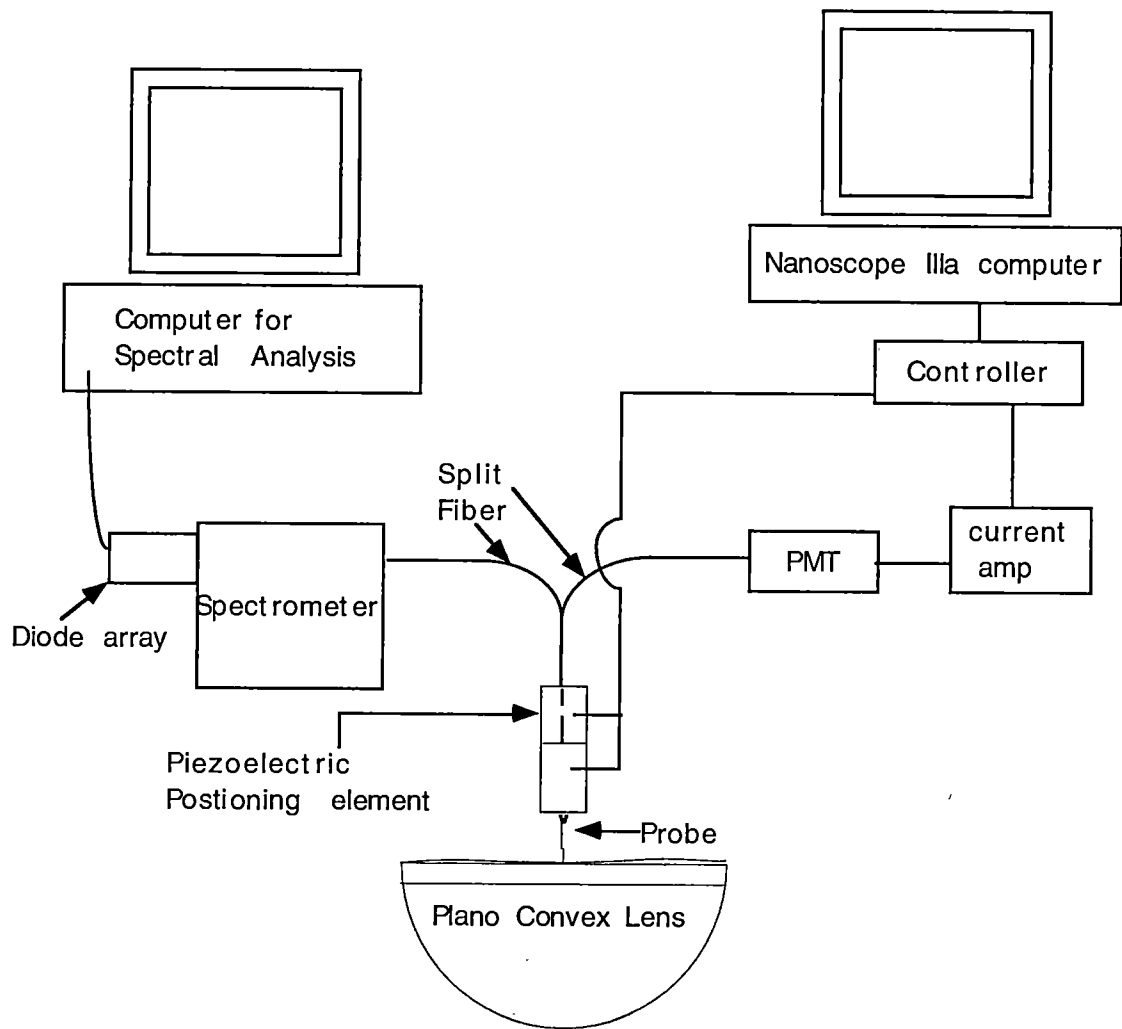


Figure 3.1: Data acquisition system for the PSTM.

probe. Piezoelectric materials are used to move the probe small distances around the surface with the piezoelectric crystal (usually in the form of a pipe) being electrically controlled by a Nanoscope IIIa[®] controller that provides the electronic amplification and signals needed to make the fine adjustments.

"The word "piezo" is derived from the Greek word for pressure. In 1880, Jacques and Pierre Curie discovered that pressure applied to a quartz crystal creates an electrical charge in the crystal; they called this phenomena the *piezoelectric* effect. Later they also verified that an electrical field applied to the crystal would lead to a deformation of the material. This effect is referred to as the inverse piezoelectric effect. After the discovery it took several decades to utilize the piezoelectric phenomenon. The first commercial applications were ultrasonic submarine detectors developed during World War I and in the 1940's scientists discovered that barium titanate ceramics could be made piezoelectric in an electric field."⁴⁹

3.1.1 Piezoelectric Scanner Construction

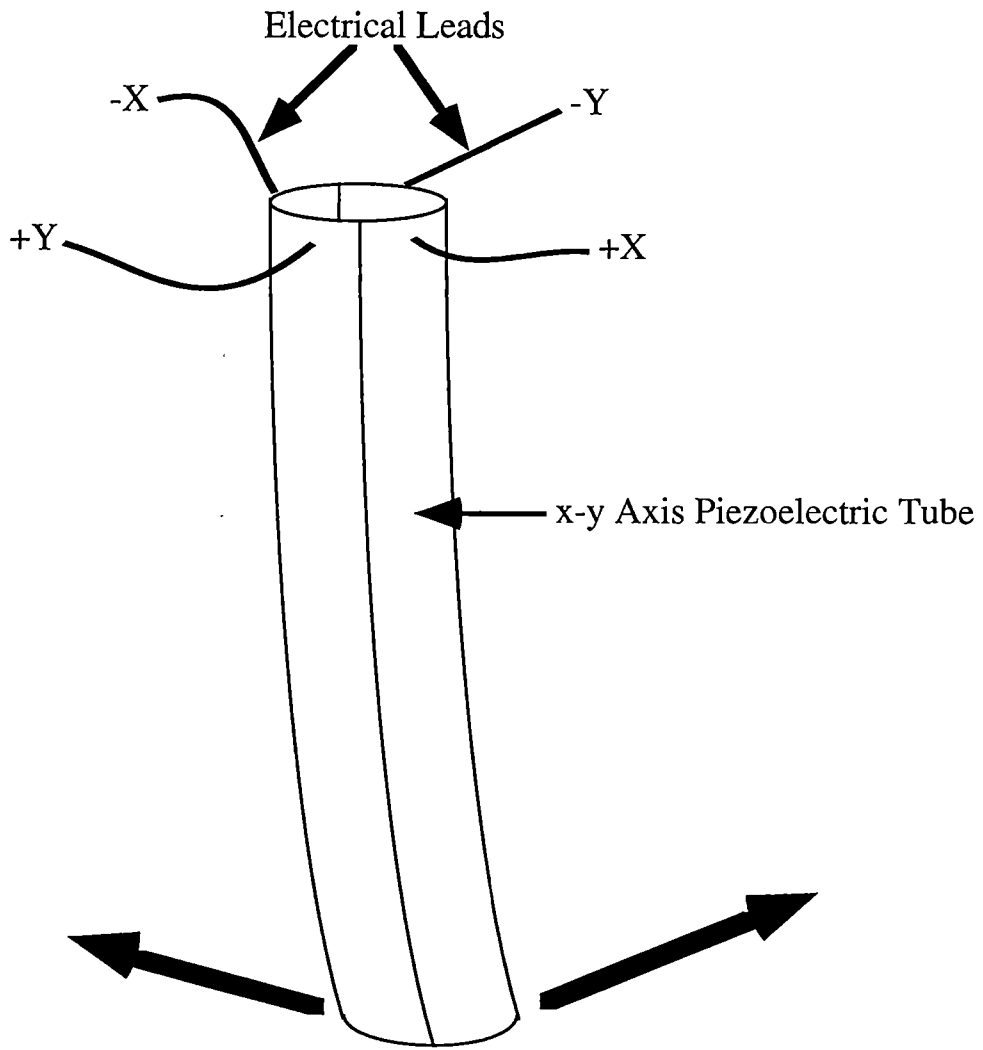
Piezoelectric tubes used in this experiment are constructed of lead zirconium titanate (PZT) by Staveley Sensors, Inc. They are #3 ceramic tubes with nickel plated electrodes on the inside and outside. (0.5" OD x 0.02"W x 2.0"L) The tubes were obtained with 90° quadrants cut (by sand blasting) through the outside surface of the nickel electrode. The segmentation of the electrodes allows different sections of the tube to be electrically isolated so that different electric fields can be placed across different sections of the tube. Using this effect to bend a quadrant-divided tube for positioning SPMs was first proposed by Binnig *et. al.* in 1986⁵¹.

When a voltage is applied across a piezoelectric material it expands or contracts. Over small lengths the strain can be approximated by $s=dE$ where s is the strain, d is

the strain constant or "d" coefficient [meter/volt], and E is the applied electric field [volt/meter]. Scanners made of piezoelectric material do not have a linear movement over large areas. Piezoelectric materials are used in many different devices like microphones, lighters, etc. If a pressure is applied to the piezoelectric material a voltage is created.

The piezoelectric material consists of crystals that contain dipole moments that are the basis of the crystal's ability to move. When the material is first created all of the dipoles are randomly oriented and must be aligned. To align the dipoles the material is heated past a critical temperature (The tubes will lose their polarity if they are heated above $\sim 190^{\circ}\text{C}$) which frees the dipole moments. A DC voltage is applied across the material that aligns the dipoles and then the system is cooled. Once the temperature drops below the critical temperature the dipoles are fixed into place and are thus aligned along the same axis. The group polarization allows the material to respond to voltages placed across the material.

By applying voltages across different segments of the piezoelectric tube a pushing and pulling affect (strain) on the tube is created and the tube bends. One side of the tube is set up to extend and the segment on the other side is set up to contract causing the tube to bend in the direction of the contracting side. (Fig. 3.2) The length of the scanning tube, thickness of the scanner walls, and the strain coefficient of the scanner material determines the maximum size of a scanner's range.



Movement of Piezoelectric Tube

Figure 3.2: Diagram of the x-y piezoelectric scan tube as it flexes.

The PSTM scan tube was constructed from a segmented piezoelectric tube that controls the x and y axis and an unsegmented tube that controls the z axis. The tubes were connected together with a MACOR[®] fitting (MACOR[®] is machineable glass) and glued together using Torr Seal[®] (a low-pressure resin). A diagram of the complete piezo tube construction is shown in Fig. 3.3.

The inside and outside of the tubes are electrically isolated so that the resistance is very large between different sections of the tubes. Contacts (metal pins) placed near the top of the tube in the ring holder (made from MACOR[®]) were used for wire connections. Wires were soldered to the contacts and each section of the electrodes of the tube to deliver the electrical signals.

A nose cone was placed at the end of the tube and a thin metal tube (hypo-tubing), used to guide the fiber through the scanner, was attached in the center of this cone. The fiber probe was attached inside the hypo-tubing with hot wax. This holds the probe fixed in place while the scanner was being used.

Excess water was removed, as water destroys the electrical isolation, from the tube through baking for ~30 mins at 100° C. After baking and while the tube is still warm it was coated in a thin sheet of plastic to protect it against hydration. Detailed diagrams of the parts for building a scanner are located in Appendix A.

Calibration of the scanner was done using a feeler gauge. The feeler gauge was set to measure the deflection in the different directions as voltage is applied to each section. A plot was made of deflection versus voltage and starting values for the tube calibration were determined. Once these were found an image of a diffraction grating

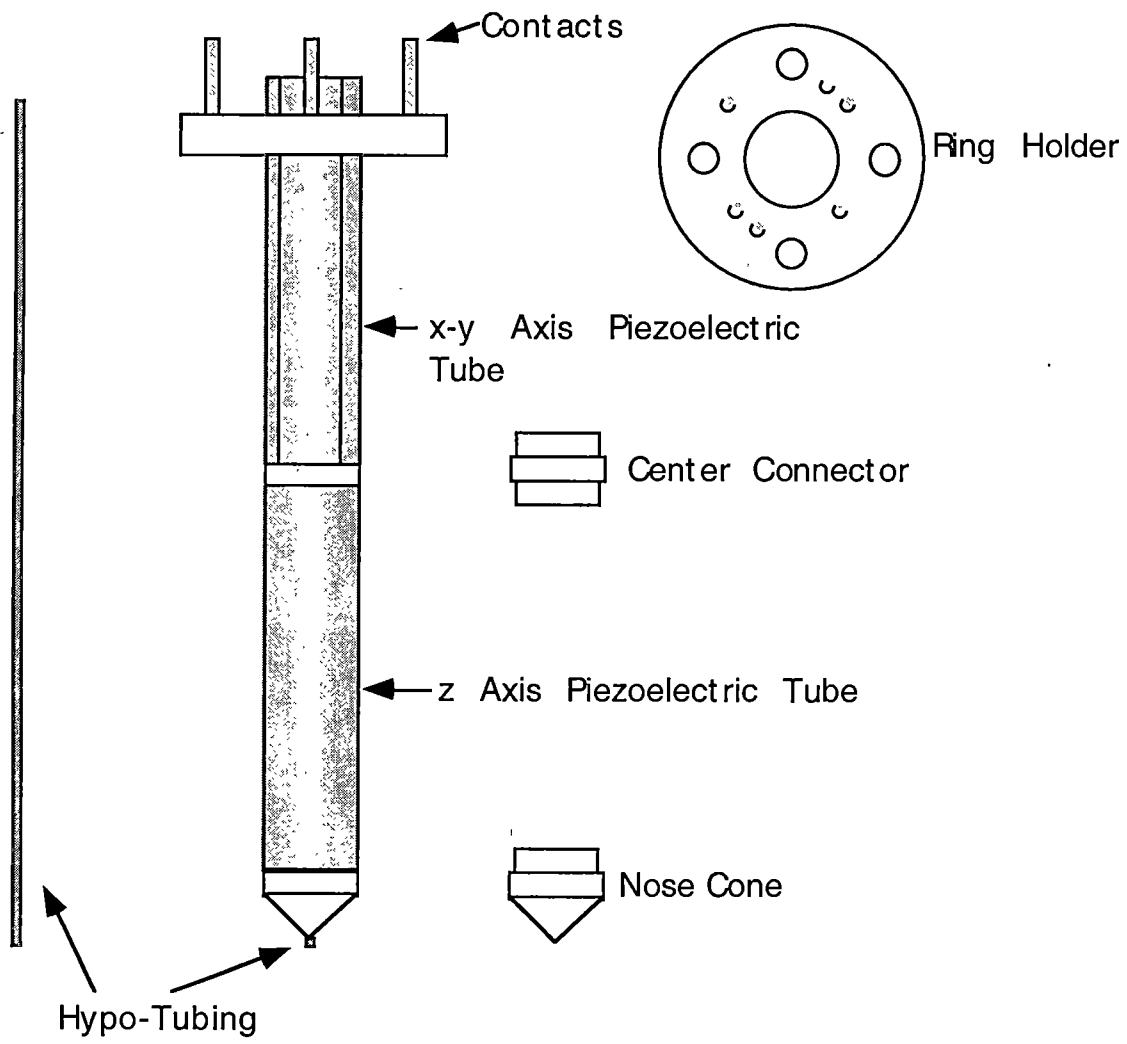


Figure 3.3: Diagram of the piezoelectric scanner.

of known spacing was imaged and then minor adjustments were made to the voltage versus distance calculations. The Nanoscope[®] has an algorithm that was used to make up for the nonlinear behavior of the piezoelectric material and the response to applied voltages can actually be determined down to the subatomic scale. For this research the scale was simply checked using other samples with known sizes and spacing.

3.2 Microscope

3.2.1 Stand and Scan Head

Drawings for the stand construction are shown in Appendix B. The stand was constructed of aluminum and consisted of a base and legs. The rotating mirror assembly attaches to the base and the microscope head sat on the top of the base. The base has dimples in the surface that were used to position the microscope head so that it did not move. Pictures of the stand and scan head can be seen in Fig. 3.4 and Fig. 3.5.

3.2.2 Nanoscope Controller

The Nanoscope IIIa[®] from Digital Instruments[®], Inc. of Santa Barbara, CA (DI) was used for image collection. The IIIa consists of a computer, controller, and software that are used to collect the data from the PSTM head. The DI software for STM is used to control the head. The controller digitizes the signal and sends information to the head from the computer and vice versa. The software is able to do many types of data manipulation. The controller also controls the feedback mechanism that keeps the

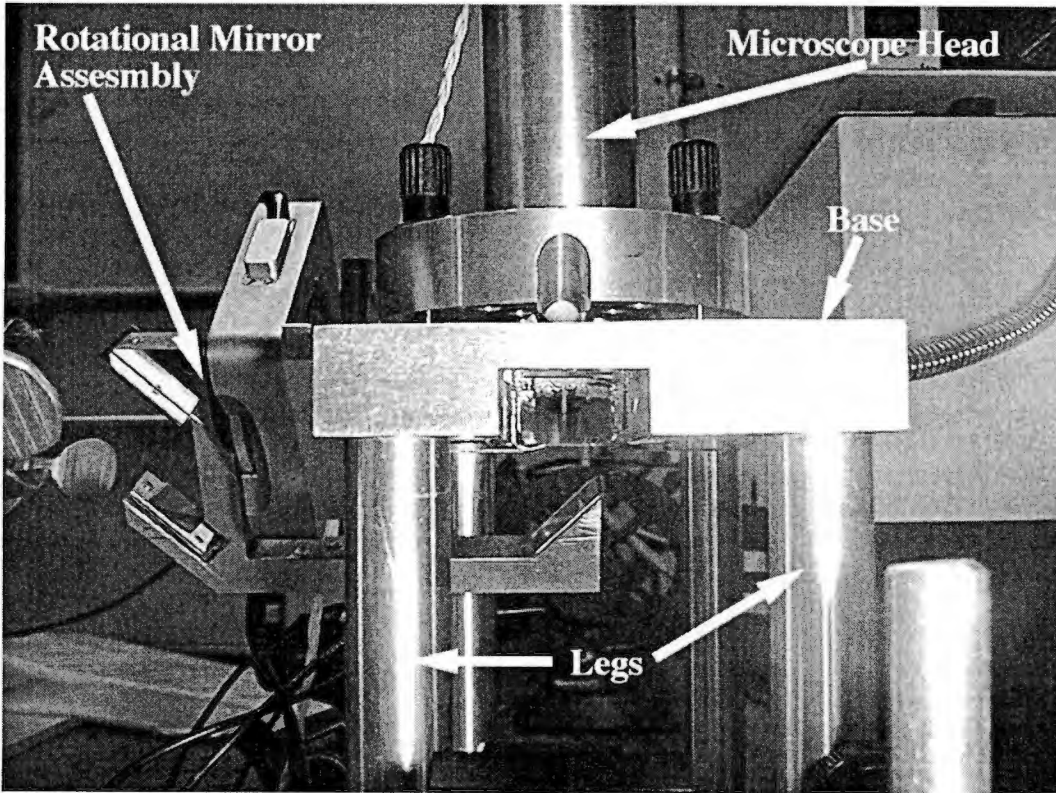


Figure 3.4: Picture of the stand with rotating mirror assembly.

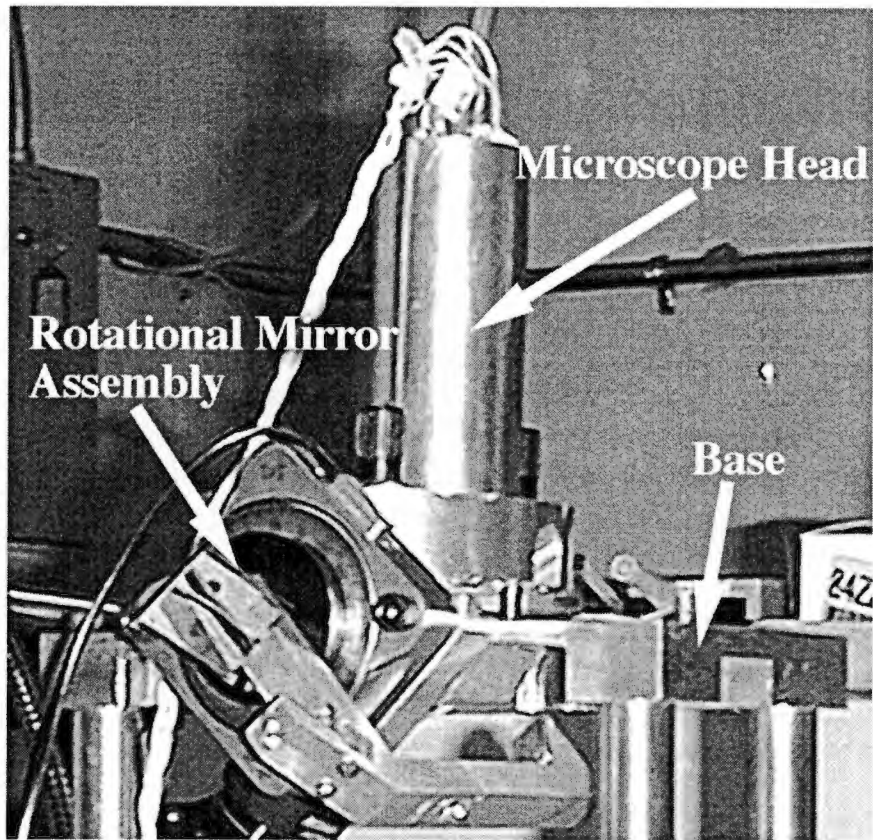


Figure 3.5: Rotational mirror assembly, stand, and scan head.

tip of the probe at the proper distance from the sample surface to maintain a constant current signal.

The Nanoscope[®] computer controller comes with a standard software package that contains many programs for image analysis and controlling the SPM. Due to the many features built into the Digital Instruments[®] software only the two types of imaging modes used in this experiment, current mode and height mode, will be discussed.

Current mode is enabled if the probe tip is scanned across the sample at a constant height z above the surface and the change in tunneling current is monitored and displayed as an image of the sample. During height mode the probe tip is scanned across the sample's surface so that the tunneling signal remains constant. To do this a feedback system built into the controller modifies the voltages across the z piezo. The voltages across the z piezoelectric tube walls are then recorded and displayed as a image of the sample.

The exponential nature also allows for scattered light to be removed from the signal. The scattered light is uniform over small distances while the tunneling signal falls off due to its exponential nature. By using the controller to look at just the (exponentially) changing signal the uniform scattered light background effects are minimized.

The probe tip was moved in a raster scan above the surface to collect data over the complete area of the sample. A sample raster scan is shown in Fig. 3.6. During the line scan in the fast scan direction a preset number (256 points for most images in this work) of data points were recorded.

3.3 Signal Detection/Analysis

3.3.1 Probe Creation

Corning® 50/125 fiber optic cable is a step index fiber that consists of an inner index material that is 50 microns in diameter and an outer index that is 125 microns in diameter which is covered by a protective plastic. The fiber was striped of this plastic cover and then cleaned with alcohol before being put into the tip puller. The tip puller then heats the fiber and stretches it into a sharp tip. The inner and outer parts of the fiber both get stretched, as the fiber is pulled.

A P-2000 laser based micropipette puller (Fig. 3.7) was used to pull the fiber optic tips. The device consists of a CO₂ laser that was used to heat the fiber while the fiber was being pulled apart. By controlling the length, force, and heat used in the pull different shapes of fiber tips were obtained. The tips were then checked with an optical microscope to confirm that they had satisfactory shape. Fig. 3.8 shows an SEM image of a gold and palladium coated fiber probe.

The parameters set to control the puller were

- **Heat**-Heating induced by the CO₂ laser
- **Fil**- Width of the area heated
- **Vel**-Velocity of trigger set point for the start of the hard pull. As the fiber heats up it starts to pull apart from the tension being placed on the fiber. When this velocity hits a certain point a hard pull was initiated.
- **Del**-Delay between the deactivation of the laser and the start of the pull.
- **Pull**-Force applied to the fiber during the hard pull.

(Typical settings used: Heat-310 fil-0, vel-6, del-127, pul-242)

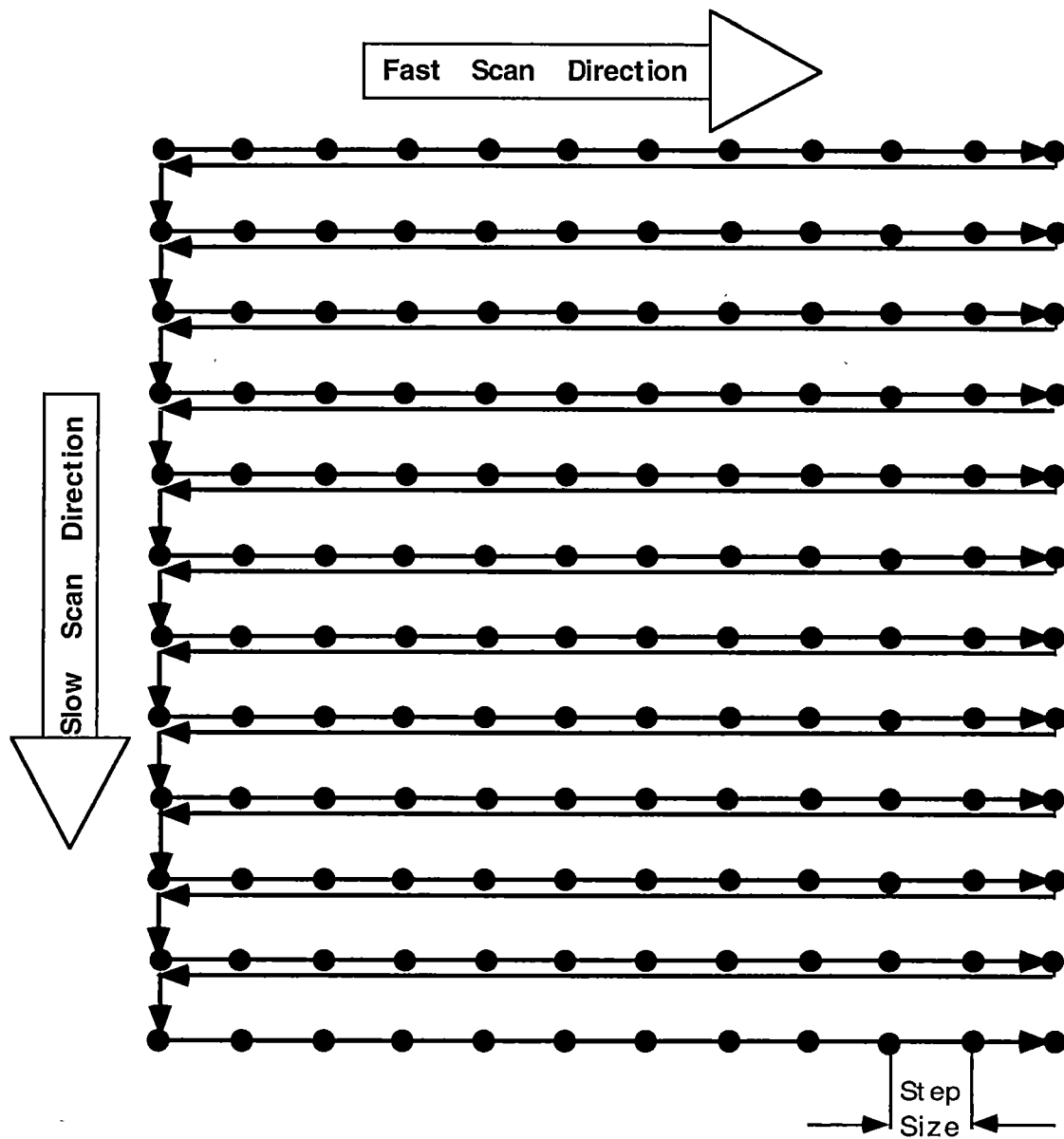


Figure 3.6: An example of a typical raster scan pattern used in the imaging of the surface of a sample with a SPM.

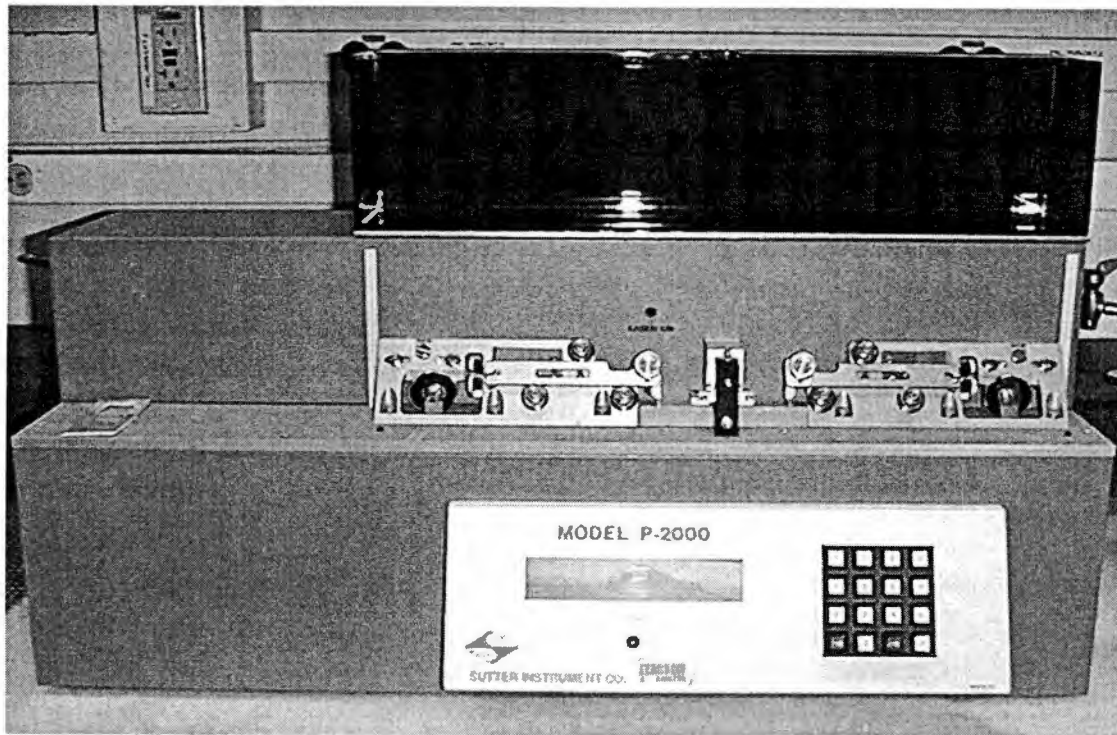


Figure 3.7: Picture of the P-2000 CO₂ laser based tip puller. The tension, heating, and other physical parameters can be adjusted to produce the optimum probe tips.

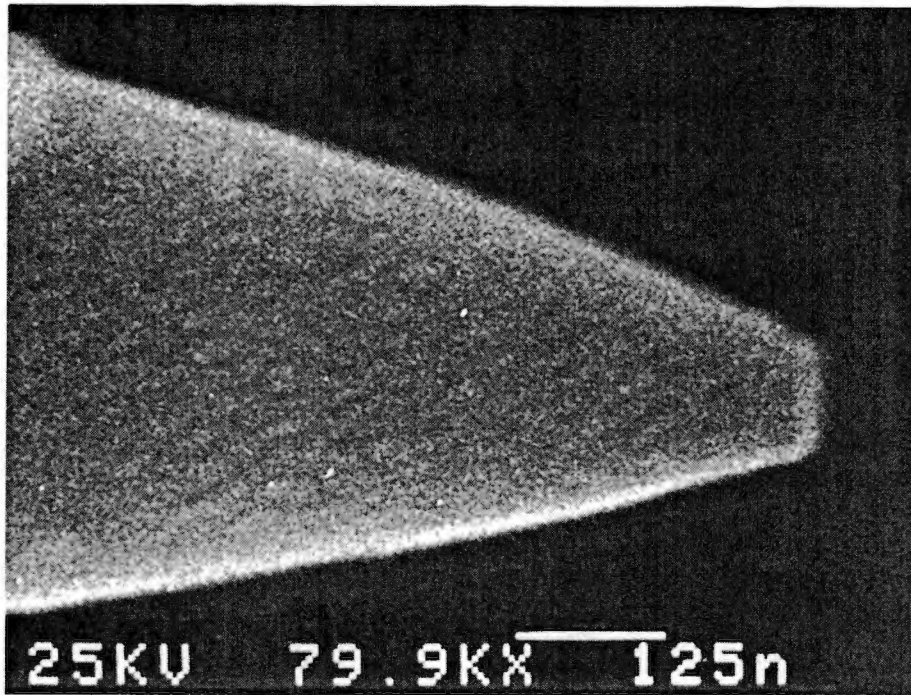


Figure 3.8: SEM Picture of a pulled fiber tip coated with 6nm of gold and palladium. The flat end of the tip is < 100nm in width and the $1/2$ angle of the cone is 15 to 20 degrees. This tip looked sharp under and optical microscope. A mild acid vapor can further sharpen such tips.

3.3.2 Spectrometer

Spectroscopy data was recorded with a Princeton Instrument[®] intensified diode array (700 diodes) attached to an ISA Jobin Yvon[®] CP 200 spectrometer or a ISA[®] (Czerny-Turner) HR-640 monochromator. The CP 200 spectrometer was equipped with a 200g/mm grating that had a spectral range from ~200 to 800 nm and a resolution better than 3.5 nm. Fig. 3.9 shows the spectral efficiency for the grating while Fig. 3.10 shows a schematic of the spectrometer. The HR-640 was equipped with a 600g/mm grating that had a spectral range from 0 to 1500 nm and 0.2 Å resolution. A schematic of the HR-640 is shown in Fig. 3.11.

3.3.3 PMT and Diode Array

The intensified diode array was monitored by a computer and controller combination. The controller "provides power, thermosetting, and timing signal to the detector head, coordinates data gathering with the experiment, sets exposure time, digitizes and averages data, and transmits it to the computer."⁵² The controller was connected to a computer through two 50-conductor shielded cables that connect, using a GPIB (IEEE-488 protocol), to an interface board. The computer ran Princeton Instruments[®] CSMA software version 2.1 to process and record the data.

The resolutions of the detectors were tested using a HG pen lamp and HeNe lasers. Data of a HG pen lamp placed in front of the spectrometer showed that the resolution of the detector was approximately the 3 nm expected value. A ThorLabs^{®53} Inc. ULTRsplice[®] connector was used for coupling the pulled fiber tip to the split fiber.

■ grating groove density : 200 g/mm (P/N : 21 374 010)

- . Non blazed
- . Spectral coverage : 300 to 820 nm
- . Resolution : < 3.5 nm
- . Spectrum (190 – 820 nm) dispersed over : 25 mm (CP 200)

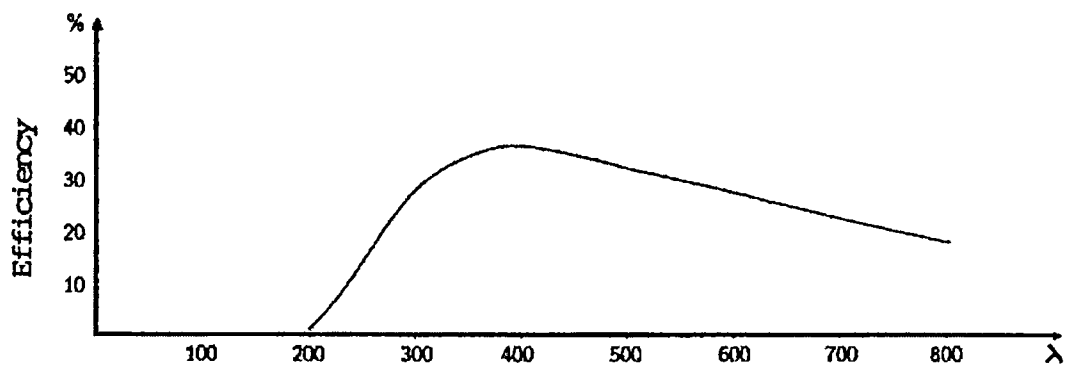


Figure 3.9: Grating parameters for the Jobin Yvon® CP200. A 200g/mm grating with a spectral range from 0 to 1500 nm and 0.4 Å resolution.⁵⁴

■ CP 200

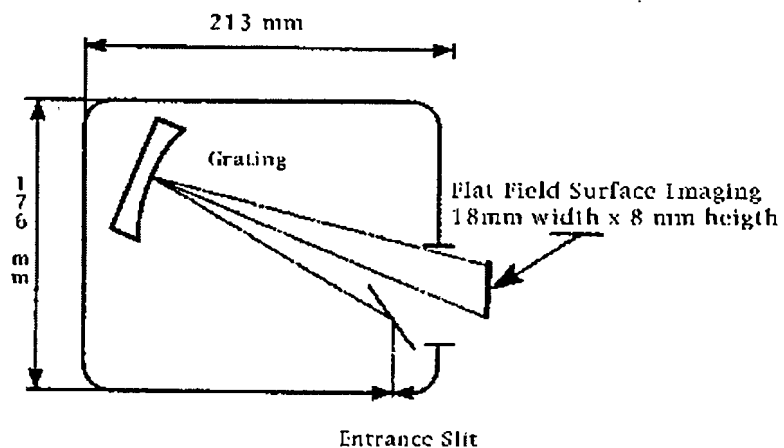


Figure 3.10: Schematic of ISA Jobin Yvon[®] CP 200 Spectrometer⁵⁴ used in gold island spectroscopy experiment.

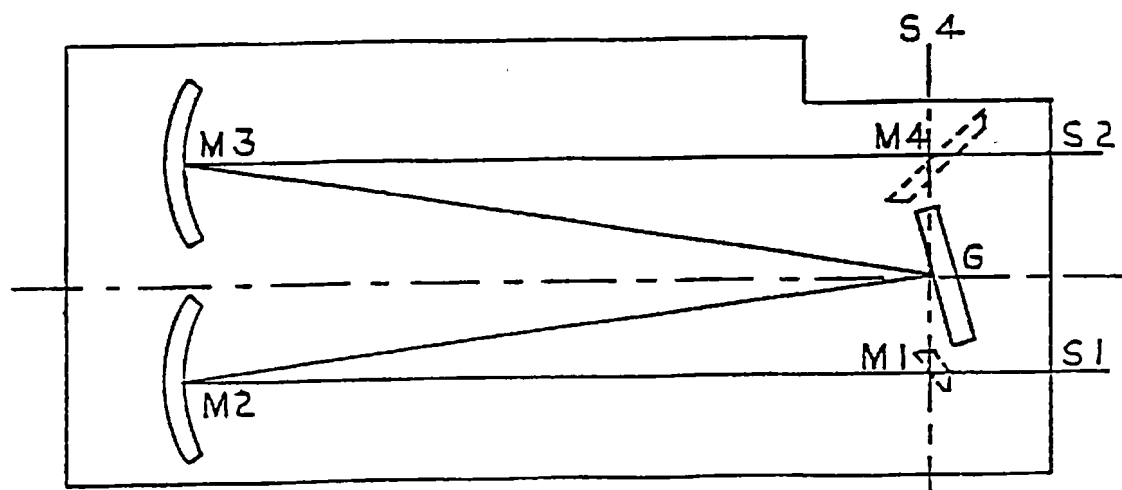


Figure 3.11: Schematic of HR-640 monochromator⁵⁵ used for the two-photon experiment.

The split fiber was created by Gould[®] fiber optics using Corning[®] 50/125 fiber. The split fiber was designed for 50/50 transmission down each path. One end of the split fiber was directed into a 1P28 PMT and the other end to a spectrometer. The ends of the fibers were fitted with ST connectors that are attached to the PMT or the spectrometer.

3.4 Illumination

3.4.1 Rotational Mirror Assembly

A diagram of the rotational mirror assembly that was used in some parts of the experiment to deliver the laser light is shown in Fig. 3.12. This assembly attached to a piezoelectric driven rotator and allowed for the delivery of light from a continuous range of angles without constant adjustments of the mirrors. It works by rotating about the center of the plano convex lens so that the beam position does not move as the mirror assembly is rotated. This is a new item to the PSTM and had not previously been used in any experiments.

3.4.2 Lasers

Standard HeNe gas lasers were used to deliver light at 632.8 nm, 544 nm and 612 nm in this experiment. Also, a HeCd laser was used for some imaging. The NSPM incorporates a HeNe laser and a Ti:Sapphire laser that is driven by an Argon ion laser. The theory behind the operation of these lasers is well known and will not be discussed in detail. List of laser used in this experiment: HeCd 440 nm, HeNe 632.8 nm, 544 nm, 612 nm, Ti:Sapphire set to 780 nm and pumped with an Ar+.

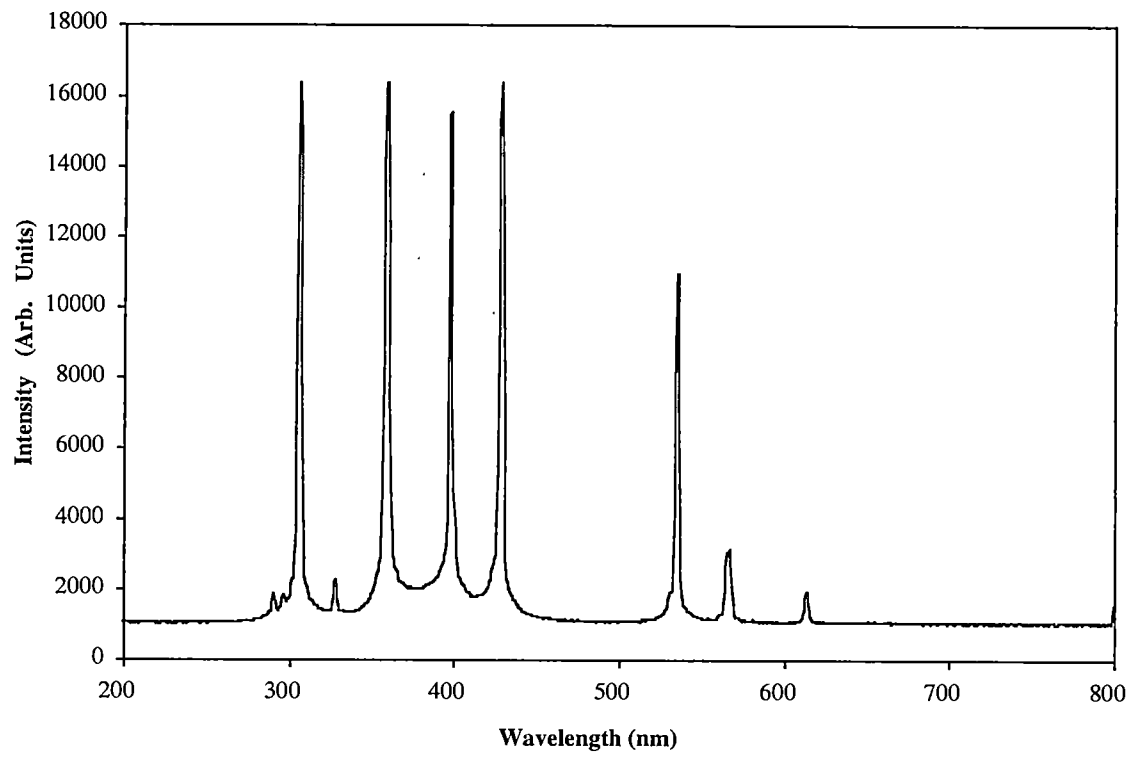


Figure 3.12: Spectrum of HG pen lamp placed in front of the CP- 200 spectrometer.

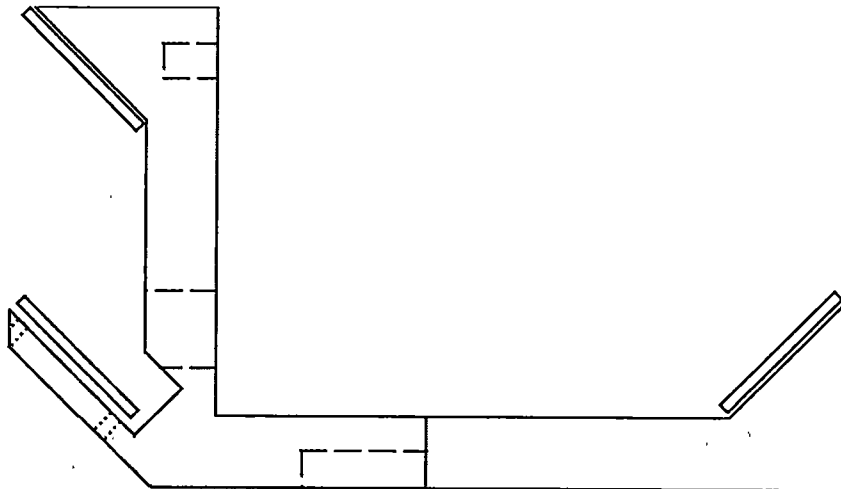


Figure 3.13: Rotational arm for mirror assembly.

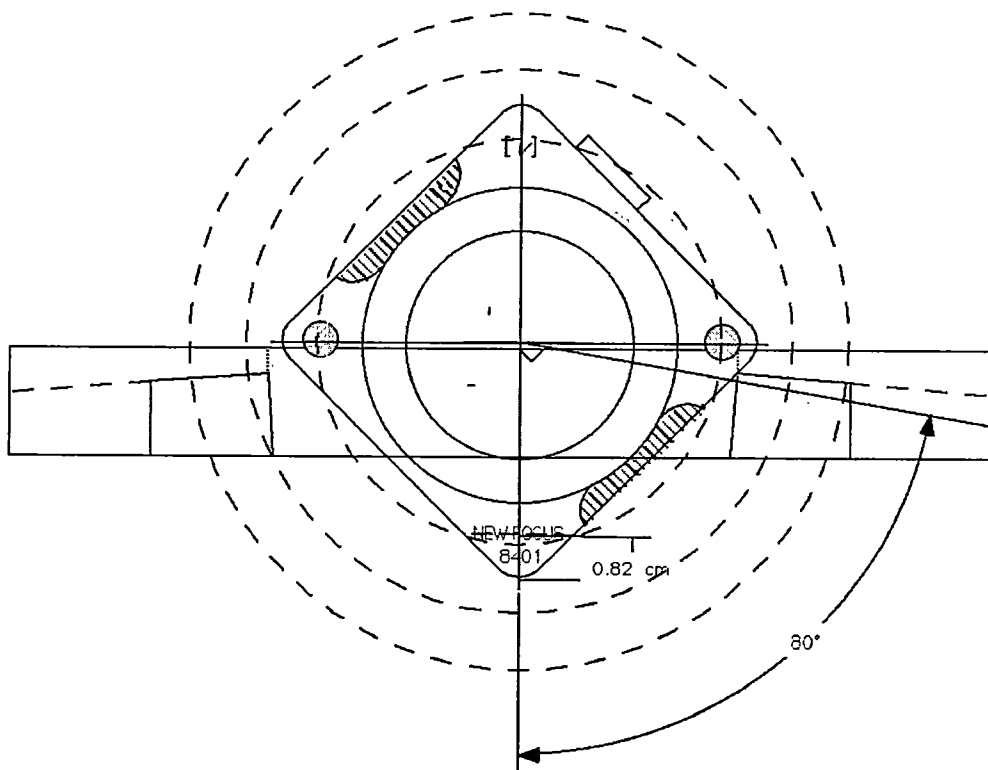


Figure 3.14: Diagram of the piezoelectric drive which rotates the mirror assembly as it is attached to the base.

3.4.3 Standard Imaging Setup

The standard imaging setup used throughout the experiment is shown in Fig. 3.15. It consisted of two HeNe lasers that were directed to the plano convex lens through the use of the rotating mirror assembly. The beams were directed so that they fell at the same spot on the sample. A cubic beam splitter was used to combine the beam paths as seen above.

The polarization rotator was used to adjust the polarization between s and p and also to adjust for changes in the polarization as the mirror assemble was rotated. (When light reflects off of the surface of a mirror it's linear polarization can be changed. The amount of change depends on the orientation of the mirror relative to the polarization. As the mirror assemble rotated the polarization of the light that is incident upon the plano convex lens changed due to the changing angle of incidence between the first mirror in the assembly and the polarization angle of the incident light.)

Polarizers and lenses were also placed in the beam path when necessary. For example when the 544 nm HeNe laser was used additional polarizers were placed into the beam path to ensure the polarization of the light. The polarizers also assured that the different laser sources had the same polarization. Variable neutral density filters were also used at times to reduce the incident power from a laser so that the power from each laser was similar.

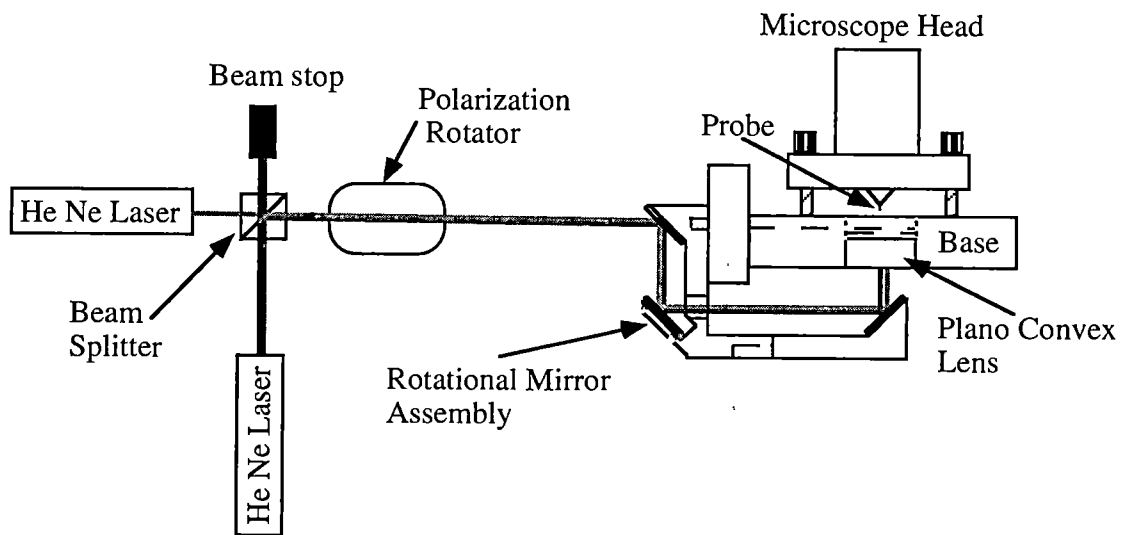


Figure 3.15: Schematic of the light delivery system for standard imaging purposes.

3.4.4 Two-Photon Light Delivery

The light delivery system for the two-photon experiment is displayed in Fig. 3.16. It consisted of a HeNe laser, that was used for imaging and probe tip sample separation, and a Ti:Sapphire laser for excitation of two-photon fluorescence. The two beams were merged with a polarized beam splitter and then focused to a small spot size (~0.5 mm) on the sample. The size of the spot can be varied to increase or decrease the concentration of light by adjusting the position of the focusing lens.

3.4.4.1 Power Meter Conversion for Two-Photon System

When data was taken in all of the experiments the power read was conducted by splitting the beam from the Ti:Sapphire laser into p and s polarization components with a polarizing beam splitter. The power that was incident upon the sample was adjusted by rotating the polarization of the beam before it entered the beam splitter. In this way the laser was left under optimum working conditions and the beam intensity could be varied. Because of this the beam incident upon the sample was proportional to the power reading being displayed. A short experiment is shown to determine the appropriate conversion for the power meter reading. In this experiment the power of the s and p polarized beams that exited the beam splitter were measured and compared. From the results a simple linear equation was determined with the slope coming from this experimental data. $I = -0.96 * (\text{power reading}) + (\text{max power reading})$

The power was measured using a Scientech® Laser Power meter model AC2500. The results of the test are shown in Fig. 3.17 and the experimental setup in Fig. 3.16.

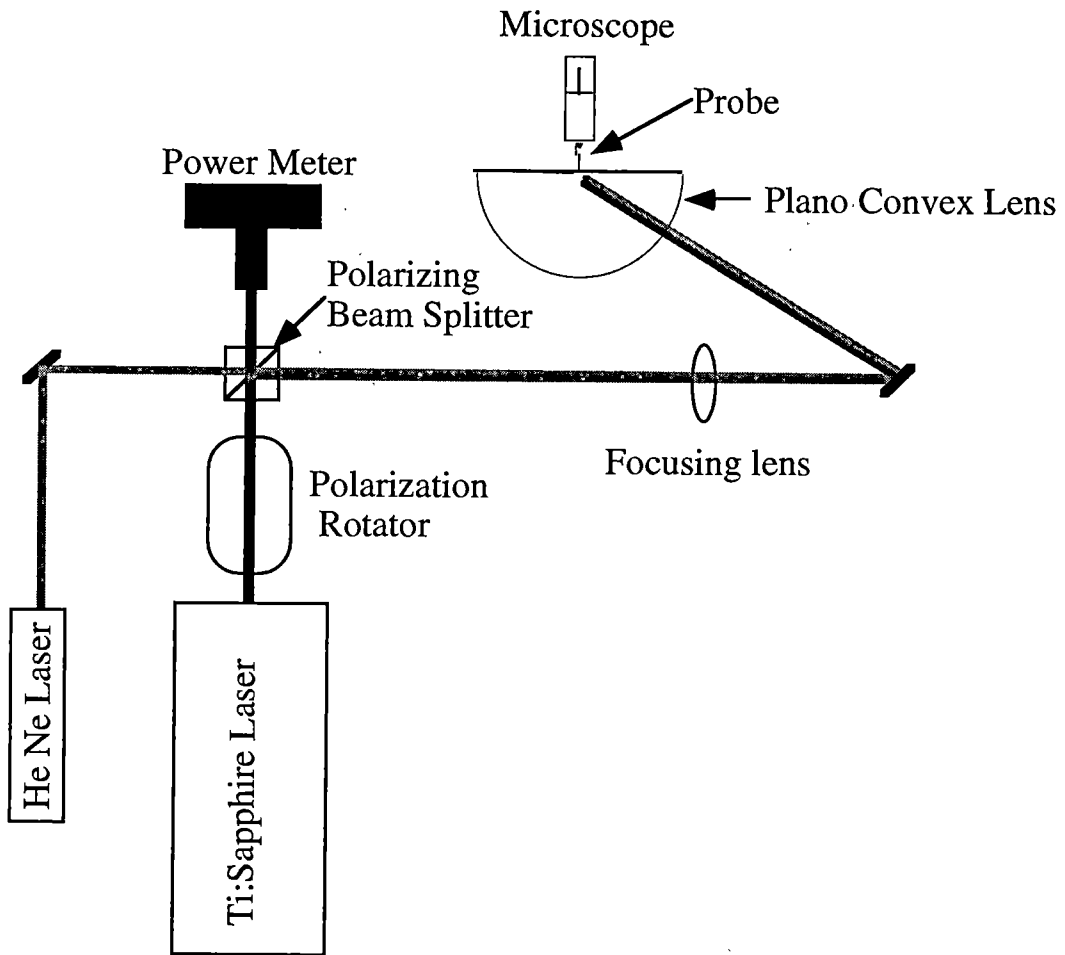


Figure 3.16: Schematic of the light delivery system for two-photon excitation purposes.

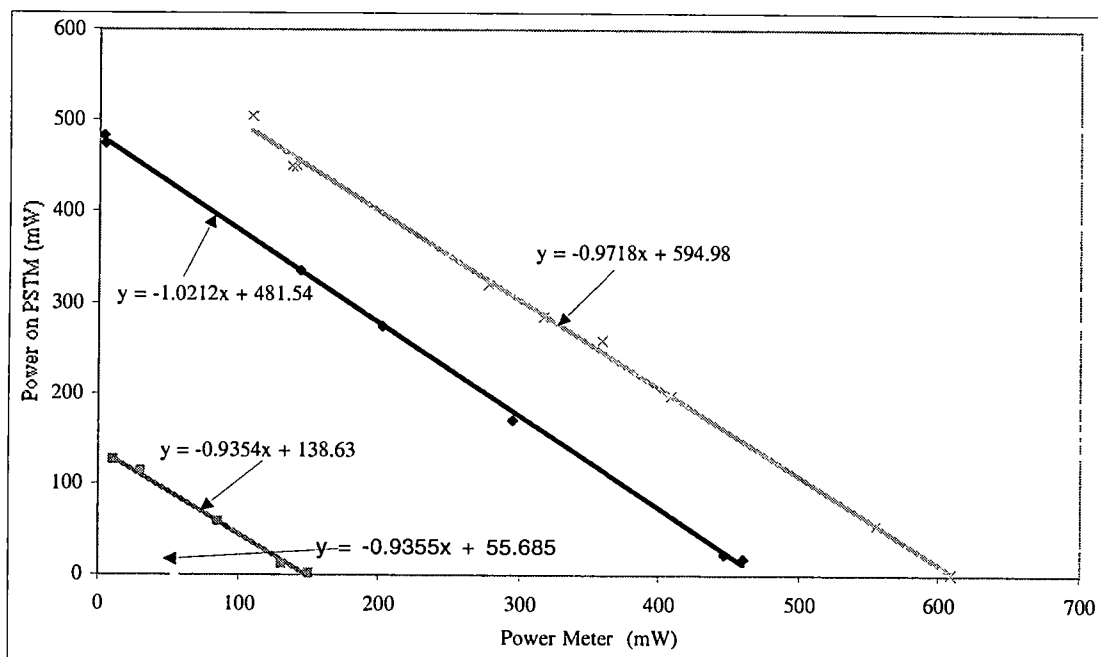


Figure 3.17: A display of the p to s power readings of the Ti:Sapphire laser after passing through the polarizing beam splitter.

3.4.5 White Light Source and Delivery System

A 73 W quartz halogen light source was used for white light illumination. The light was collected with lens and focused into a fiber bundle that transmitted the light to another focusing lens located below the plano convex lens. The light was brought into the plano convex lens and focused to a 5-mm spot so that TIR conditions existed for all the wavelengths of the light source. The white light signal was used for spectroscopic purposes and not for imaging as the signal was too noisy to produce clean images. A laser delivered from the opposite side of the plano convex lens by the rotating mirror assembly was used for imaging purposes. A schematic of the light delivery system is shown in Fig. 3.18.

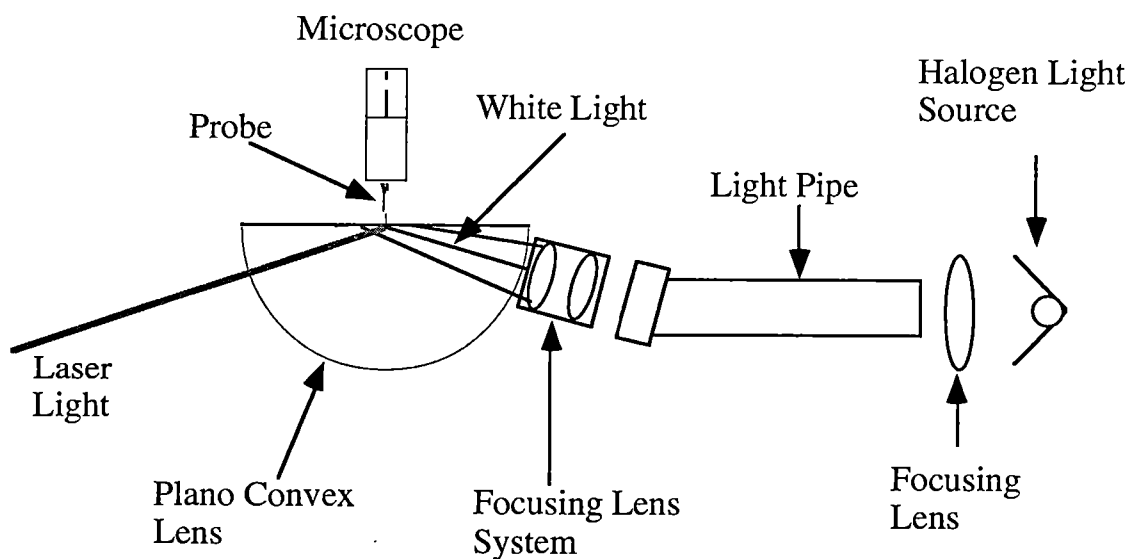


Figure 3.18: Schematic of white light delivery system.

3.5 Sample Preparation and Characterization

3.5.1 Sample Cleaning

Before a sample is prepared the substrate must be cleaned. This cleaning process for mica and quartz are given below.

Sample cleaning for quartz:

1. Wash each slide with microwash (Microwash is an ammonia based detergent that will remove finger prints and dust.)
2. Rinse the slide with hot tap water for 5 minutes to remove the microwash
3. Put in an acetone bath in the ultrasonic cleaner for 5 minutes
4. Rinse with acetone
5. Put in an isopropanol bath in the ultrasonic cleaner for 5 minutes
6. Rinse with isopropanol
7. Blow-dry with clean nitrogen gas
8. Put directly into the vacuum evaporator for coating

Sample cleaning for mica:

1. Rinse mica with acetone
2. Rinse mica with isopropanol
3. Blow-dry with clean Nitrogen gas
4. Attach scotch tap on one side of mica (This is used to cleave the mica)
5. Remove the tape (This removes a thin layer of mica and exposes a clean layer)
6. Put directly into the vacuum evaporator for coating

3.5.2 Vacuum evaporation process

A cryopump based electron beam vacuum evaporation system was used to deposit the gold onto the substrate. The evaporator was pumped down to 3×10^{-6} torr through a series of steps of rough pumping, sorption pumping and then cryopumping until the system reached the desired pressure. Once the pressure was low enough an electron beam was focused onto a sample of gold until it evaporated. The gold was then heated through electron bombardment, a crystal thickness gauge monitored the thickness and rate of evaporation during the process. Gold samples were then annealed to form gold islands. During the heating process the gold moves around on the surface forming small balls of material. The higher the heat the more spherical the balls of gold became. A small tube oven was used for heating the samples.

3.5.3 Description of the Shimadzu® (model UV-250).

The Shimadzu® spectrophotometer was used for initial characterization of gold island samples. The Shimadzu® is a double monochromator recording spectrophotometer which was used to find the absorption or transmission plots of materials. It uses a sample and a reference slide, a piece of clean substrate material, to measure the absorption.

The absorption calculation, taking the negative log of the sample divided by the reference for each wavelength, was done automatically.

3.5.4 Spectrometer Set up for Fluorescent Measurements

A HR-640 spectrometer was set up with a computer controlled data acquisition system. The data acquisition was done with an AD board and a visual basic program. The voltage over a silicon photo diode was measured and correlated with the position of the spectrometer. This equipment was used to characterize the fluorescence of the yellow dye used in the NSPM experiments.

Chapter 4 Results

In this chapter results are presented which cover many different aspects of the tip to sample interaction process. The chapter begins by presenting comparative imaging results for gold metal island films and then progresses to absorption spectroscopy of these films. After showing these results data is presented which demonstrates the microscopes ability to detect two-photon fluorescence as related to the NSPM. Finally, preliminary results are presented to show the possibility of distance to the surface measurement. The diversity of results is a consequence of attempts to improve the versatility of the PSTM and to demonstrate the need for improvements enabling the tip to be precisely placed close to the sample.

4.1 Imaging with the PSTM

The PSTM is an instrument used to image and characterize the electrodynamic topography of samples. When imaging with the PSTM many different parameters must be taken into consideration because one must be aware of what the PSTM measures when it records an image. In general, for nonmetallic or transparent samples, the PSTM measures the evanescent field decay associated with light that is nominally totally internally reflected from the top of the sample. Far field scattering, in this case, is not a problem as long as the size of the particle/structure to be measured is small compared to the wavelength used for imaging. (An experiment examining far field scattering intensity measurements was performed and the results are given in Appendix C.) Small feature size relative to the illuminating wavelength is a standard

condition, and limiting factor, for all samples imaged with the microscope. Larger samples can be imaged if the tip can be prevented from colliding with the sample. For example, human venous blood chromosomes of micron sizes have been imaged with the PSTM⁵⁶. (Appendix D gives example of images (Interference, Nuclepore filter, crossed grating) obtained with the microscope. Images of gold islands obtained by imaging with the surface plasmon field are found in Appendix E.)

A key difference is obtained when imaging metal samples. In this case the induced electric dipole field on a local structure produces an external energy density that is sampled by the PSTM in the near zone of the radiation field. As such, the flux detected is a measure of the near-zone form of the electromagnetic cross section of the local structure. The ability to measure the near-zone field is a distinct advantage since the structure's physical topography alone, as measured at a wavelength at which the polarizability is small, is nearly identical with the electromagnetic topography if the probe is within a few nanometers of the sample. That is, the electromagnetic topography can be measured across a range of wavelengths starting with a range in which the frequency-dependent polarizability is small and ending in any desired range such as the range of the surface plasmon resonance. Unfortunately, present methods for tip positioning and the available scanning mechanisms severely limit these features. Nevertheless, it can be expected that improvements in scanning-probe mechanics will continue and it is therefore important to explore positioning methods for imaging and spectroscopy, testing of metal samples, and alternative signal collection methods.

4.2 Imaging of Metal Island Films

When metal island films are measured new parameters must be understood when viewing PSTM images. In images of metal island films the size of the particles appear greater than their physical size because of an increase in signal due to the plasmon (dipole) field present in and around each particle. This field will in effect smear out the image of the physical topography of the particle. The smearing of the image can be viewed as a direct measurement of the *total* optical cross section around each particle in the near zone of the particle's radiation field. In this zone the fields are electrostatic in spatial nature and are simple dipole fields that are well understood.

Images of metal island films demonstrate that the electromagnetic topography of the particles change when illuminated by different wavelengths of light. When a wavelength of light corresponding to a plasmon resonance in the particle is used the electromagnetic topography is of a much larger scale. When a wavelength is used that is off of the resonance the particles appear closer to their physical size.

When the resonance condition is met on a certain particle this plasmon field will compete with and possibly overpower the evanescent field. Therefore, images will be dominated by particles for which the resonance condition has been met and particles that are off resonance will be obscured if they are too close to the target particles. This is demonstrated in images that are presented of the same sample area imaged with different wavelengths of light.

4.2.1 Gold Islands ---Experiments

For this experiment thin films of gold metal islands were produced by evaporating gold onto mica substrates and onto quartz substrates, which were then heated. The heating allows the gold to migrate on the surface of the substrates and form small metal particles (as discussed earlier). A low heating temperature ($\sim 150^\circ\text{C}$) was used in some cases in an attempt to minimize the uniformity of the particle shape distribution on the surface. Higher heating temperatures and longer heating times lead to rounder particles with a smaller shape distribution⁴³.

4.2.1.1 Gold Islands on Mica

The imaging capabilities on a sample of gold islands is shown in Fig. 4.1, Fig. 4.2, Fig. 4.3, and Fig. 4.4. (For comparison an image of a clean mica substrate is give in Fig. 4.5.) Each sample consists of 4.1 nm of gold evaporated onto a mica substrate and then heat treated for 4 minutes at 200°C . A HeNe 632.8 nm laser with s-polarization at a 50° incident angle was used for imaging. These images show resolution at different scan sizes and show a consistency and scaling in the images. The labels "A" and "B" mark similar structures in scans over the same area. The absorption maximum, as determined from data taken with the Shimadzu[®] spectrophotometer, for this sample is located at $\sim 650\text{ nm}$. Each scan line consists of 256 samples across the scan range. Also, all of the island on mica images were obtained with the microscope in height mode where the tunneling signal between the probe and the sample were

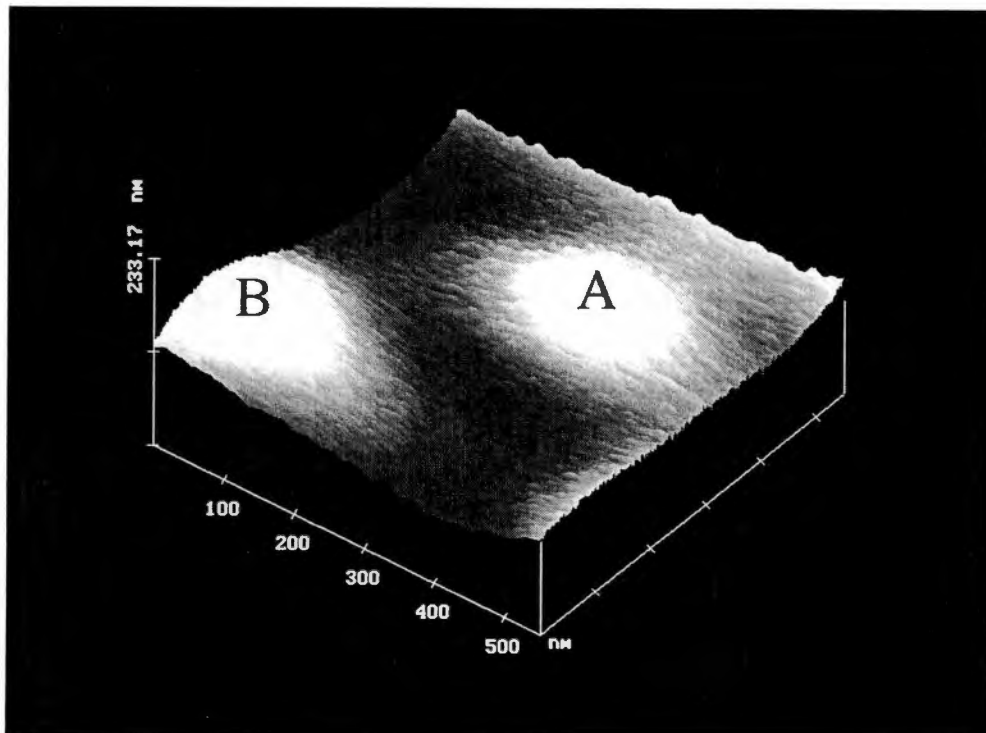


Figure 4.1: A 550 nm image of gold islands on mica under s-polarization with a 632.8 laser incident at 50° . The mica was coated with 4.1 nm of gold and then heat-treated for 4 minutes @ 200° C. The particles in this image appear ~ 300 nm in width. A and B are used to mark the position of the particles for different scan sizes.

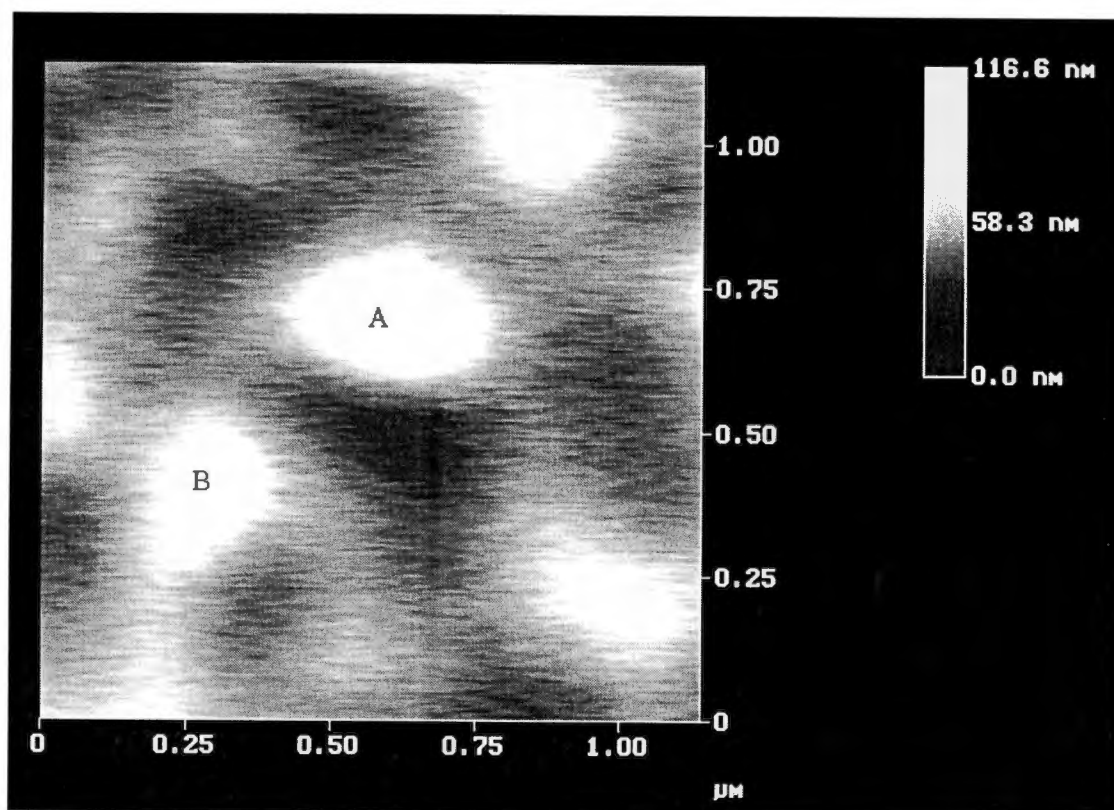


Figure 4.2: A 1.25 μm scan of gold islands on mica under s-polarization with a 632.8 laser incident at 50° . This is the same area as Fig. 4.1 over a larger scan range. The mica was coated with 4.1 nm of gold and then heat-treated for 4 minutes @ 200°C . The particles in this image appear ~ 300 nm in width.

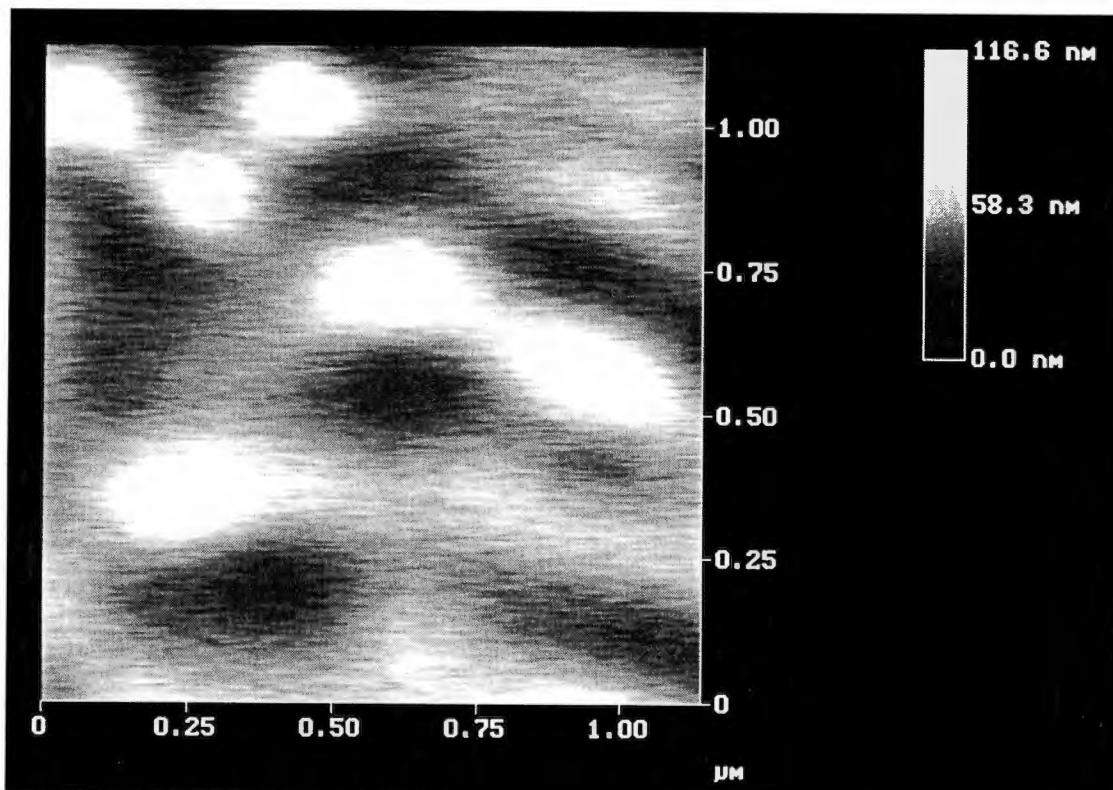


Figure 4.3: A 1.2 μm scan of gold islands on mica under s-polarization with a 632.8 laser incident at 50° . The mica was coated with 4.1 nm of gold and then heat-treated for 4 minutes @ 200°C . The particles in this image appear ~ 300 nm in width.

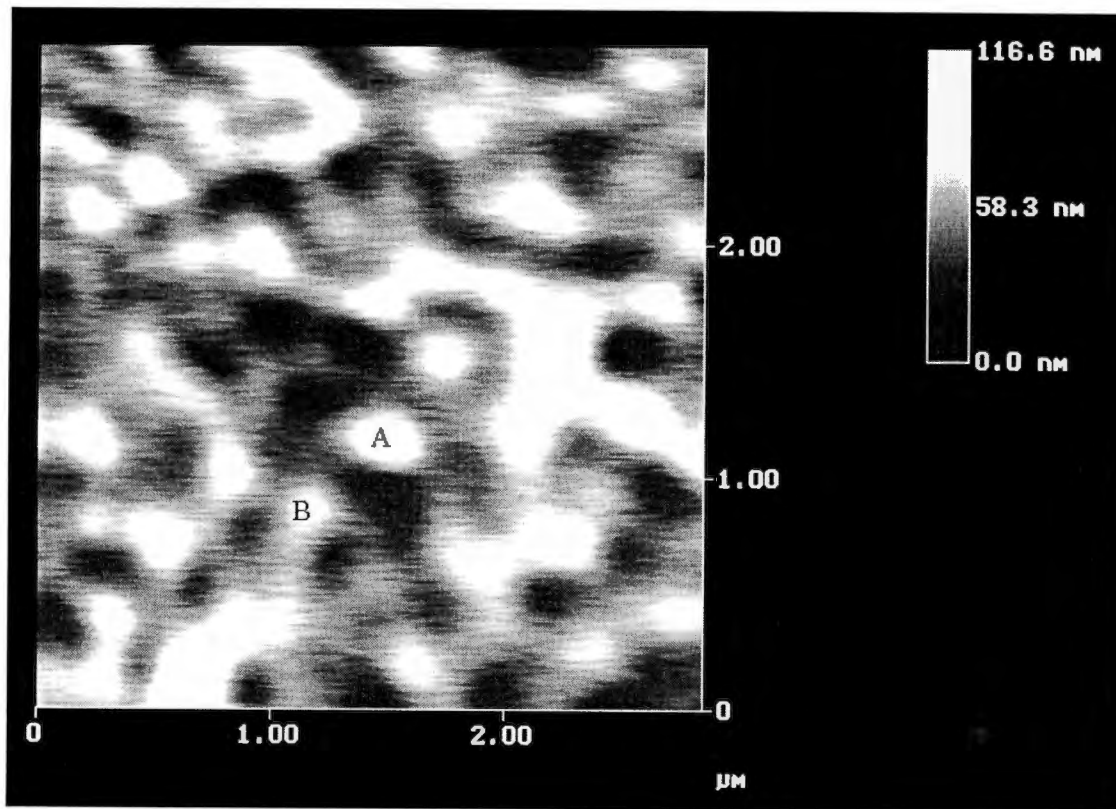


Figure 4.4: A 3 μm scan of gold islands on mica under s-polarization with a 632.8 laser incident at 50° . The mica was coated with 4.1 nm of gold and then heat-treated for 4 minutes @ 200°C . The particles in this image appear $\sim 300\text{ nm}$ in width.

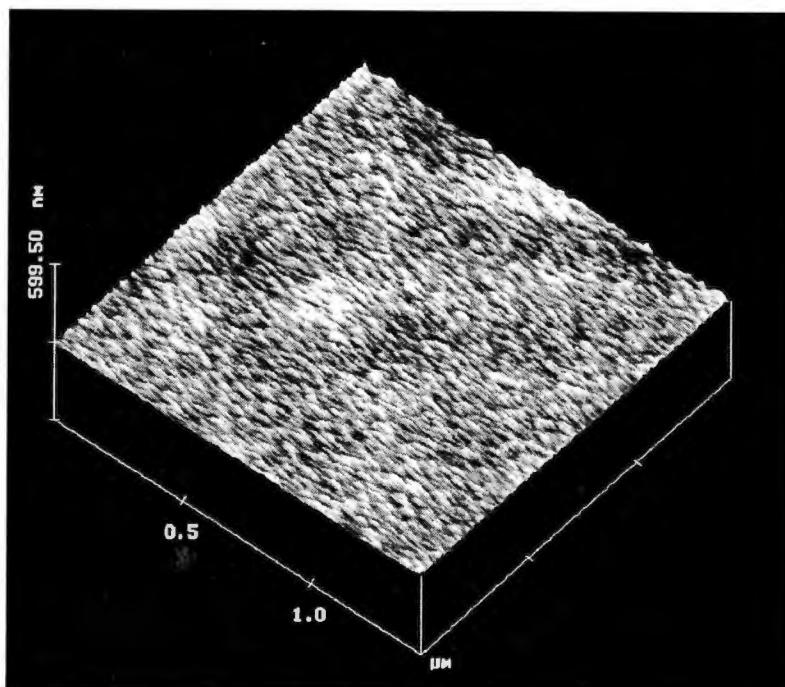


Figure 4.5: A 1.5 μm PSTM image of clean mica. This was imaged with a s-polarized 632 nm laser light incident at 50° . The image does not show any real structure above noise.

held constant by adjusting the z-axis position of the probe. It is the z-axis movements, along with the x-y positions, that were measured and recorded in each scan.

AFM images of the islands on a Mica substrate are shown in Fig. 4.6 through Fig. 4.9. When these images are compared with the PSTM images one can see that the particle sizes appear approximately 10 times larger in the PSTM measurement. The particles have an average size of 300 nm in the PSTM images while only have an average size of 30 nm in the AFM images. Also, it is important to remember that the PSTM images will be dominated by particles that have a shape that matches the resonance conditions for 632.8 nm light.

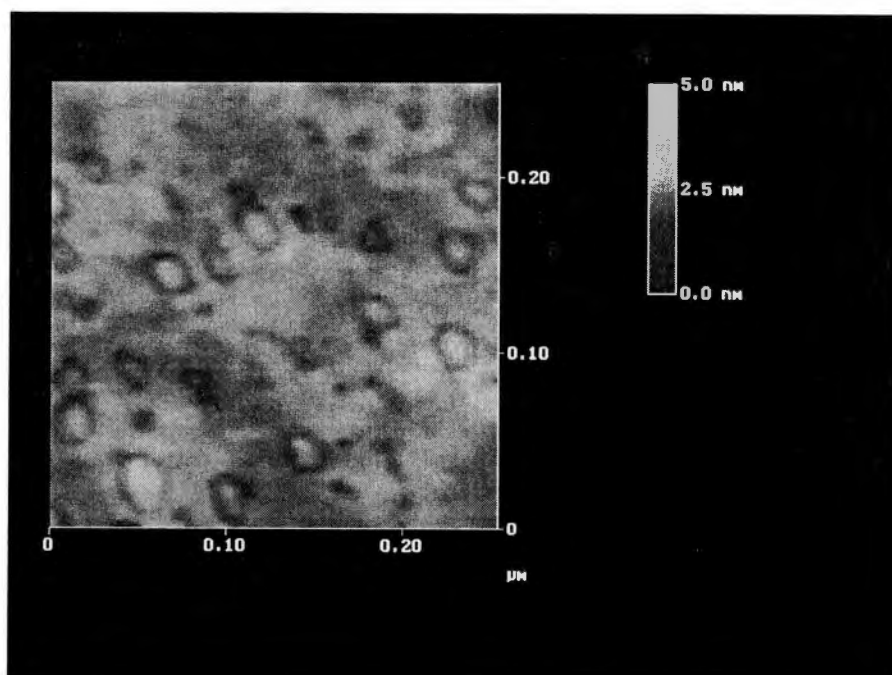


Figure 4.6: An 2.5 μm AFM image of gold islands on mica of 4.1 nm of gold heat-treated for 3 minutes @ 150° C The particles in this image appear ~ 30 nm in width.

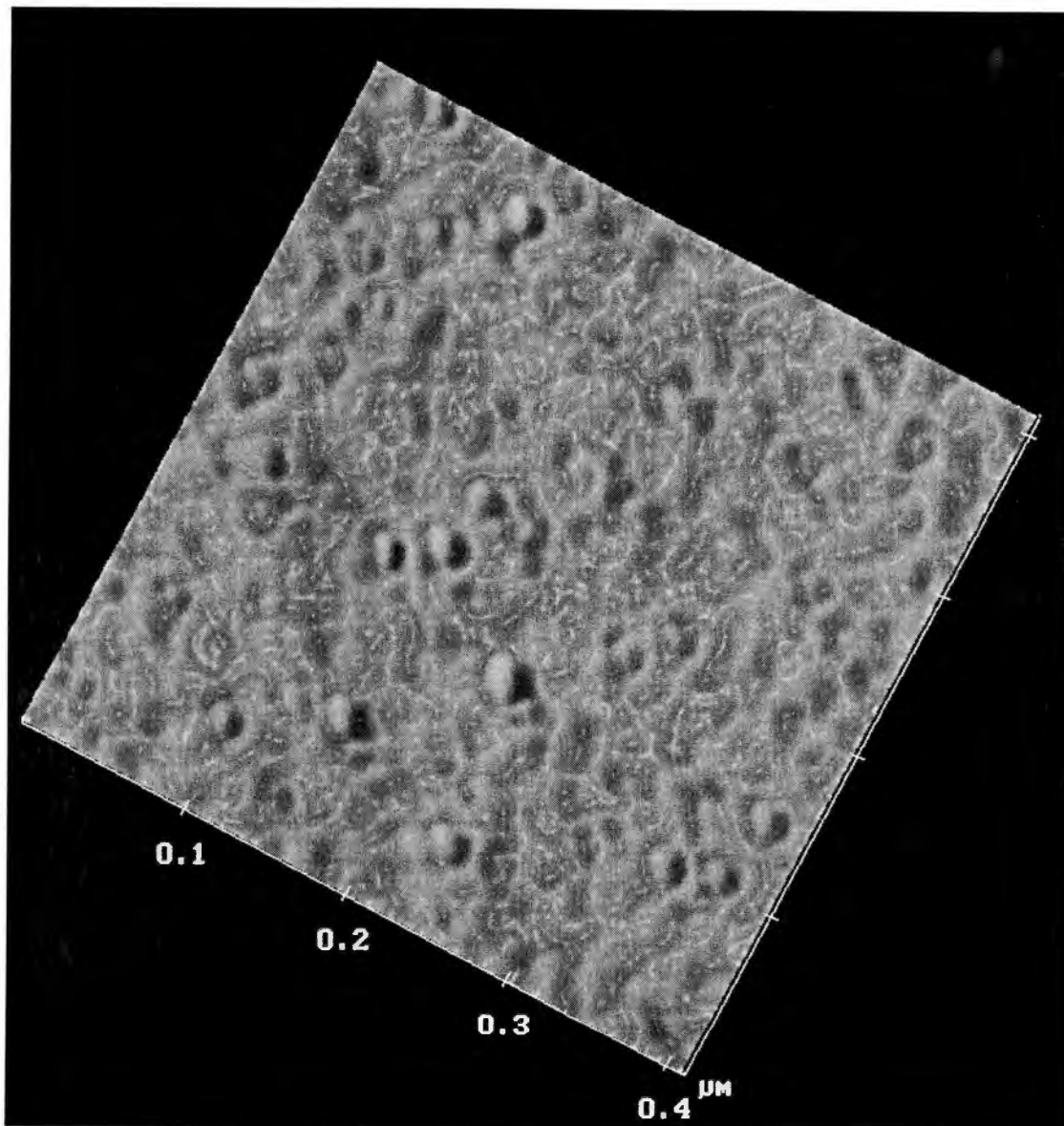


Figure 4.7: A 3-D 0.4 μm AFM image of gold islands on mica of 4.1 nm of gold heat-treated for 3 minutes @ 150° C. The particles in this image appear ~30 nm in width.

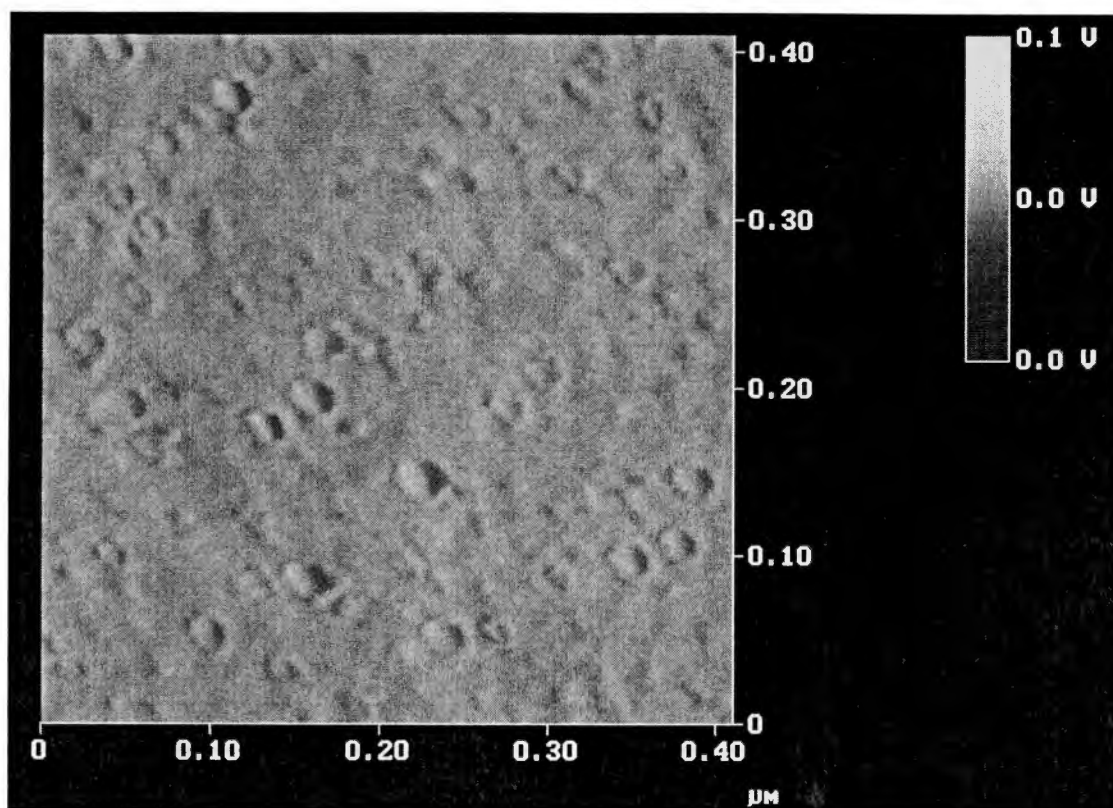


Figure 4.8: An $0.42 \mu\text{m}$ AFM image of gold islands on mica of 4.1 nm of gold heat-treated for 3 minutes @ 150°C . The particles in this image appear $\sim 30 \text{ nm}$ in width. This is the same area as in Fig. 4.7.

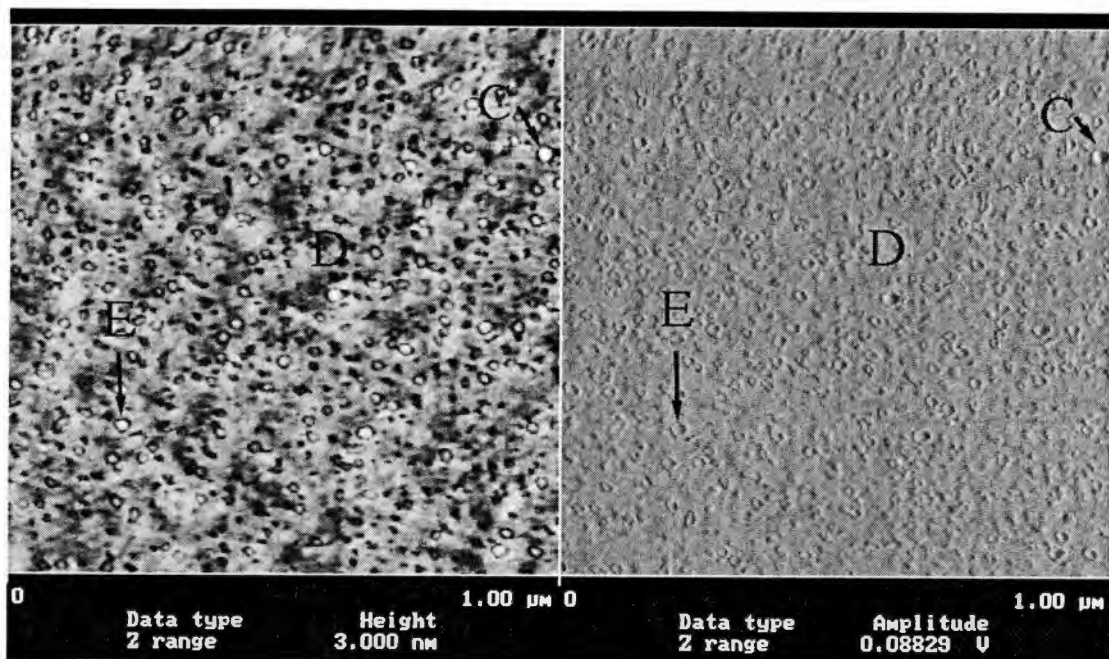


Figure 4.9: An 1.0 μm AFM image of gold islands on mica. The 4.1 nm of gold was heat-treated for 3 minutes @ 150° C. The right image is displayed in Amplitude mode while the left is displayed in Height mode. The particles in this image appear ~30 nm in width.

4.2.1.2 Gold islands on Quartz

The imaging capabilities on a sample of gold islands on quartz are shown in Fig.4.10 and Fig. 4.11. Each sample consists of 4.6 nm of gold evaporated onto a quartz substrate and then heat treated for 6 minutes at 800° C. A HeNe 632.8 nm laser with s-polarization at 50° incident angle was used for imaging. A Corning 125/50 multi-mode fiber, pulled to a point with a micropipet tip puller, was used as a probe. These images show resolution at different scan sizes and show a consistency and scaling in the images. The absorption maximum, as determined from data taken with the Shimadzu spectrophotometer, for this sample is located at ~600 nm. Each scan line consists of 256 samples across the scan range.

The imaging capabilities on a sample of gold islands on mica are shown in Fig. 4.12 and Fig. 4.13. Similar areas in the images are marked with corresponding letters. Each sample consists of 4.6 nm of gold evaporated onto a mica substrate and then heat treated for 6 minutes at 600° C. A 544 nm HeNe laser and a 440 nm HeCd laser at a 46° incident angle and s-polarization were used for imaging. These images show resolution at different scan sizes and show a consistency and scaling in the images. There are also images taken over the same scan area with different wavelengths of light which demonstrate differences. The particles imaged with the 544 nm light appear larger than the particles imaged with the 440 nm light. This is due to the 544 nm light being closer to the resonance value of the islands and the resulting larger electromagnetic cross section in this sample. The images taken with 440 nm light

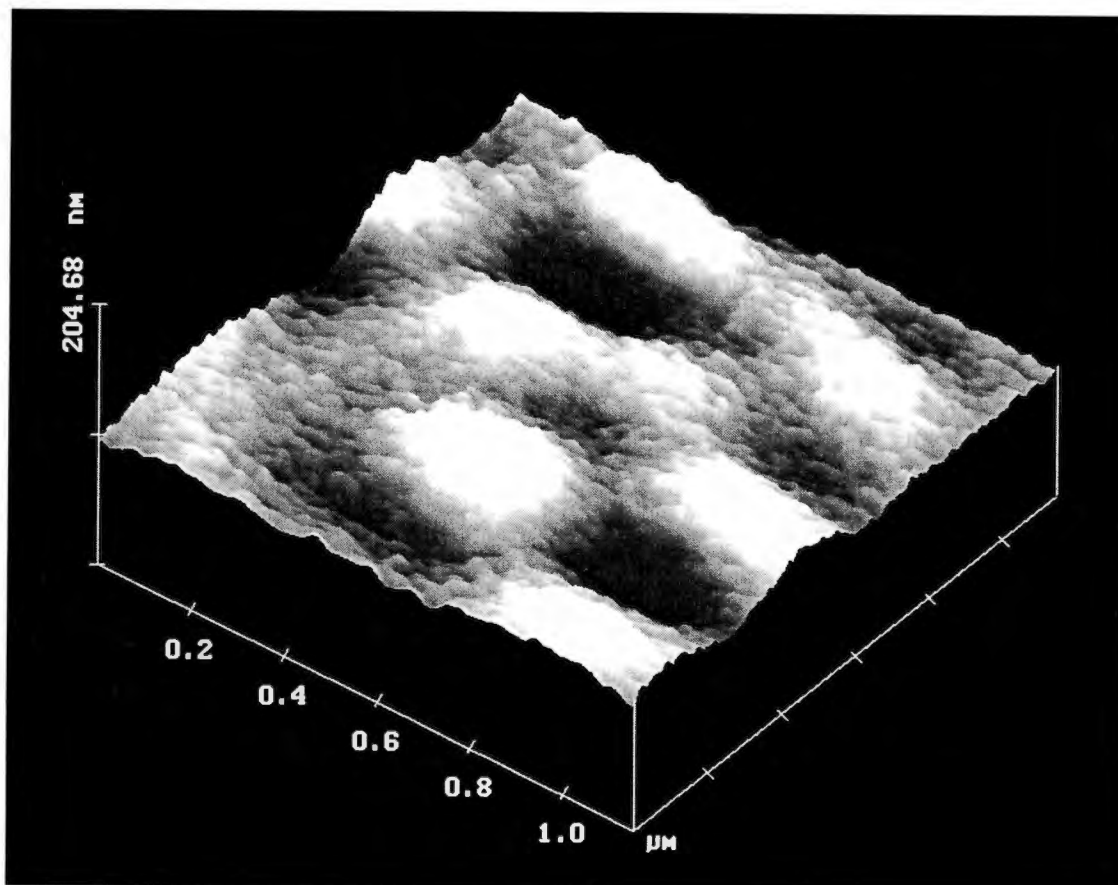


Figure 4.10: A 1.1 μm PSTM image of gold islands on a quartz substrate under s polarization with a 632.8 laser at 50° angle of incidence. The quartz is coated with 4.6 nm of gold and then heat treated for 6 minutes @ 800°C . The particles in this image appear ~ 240 nm in width.

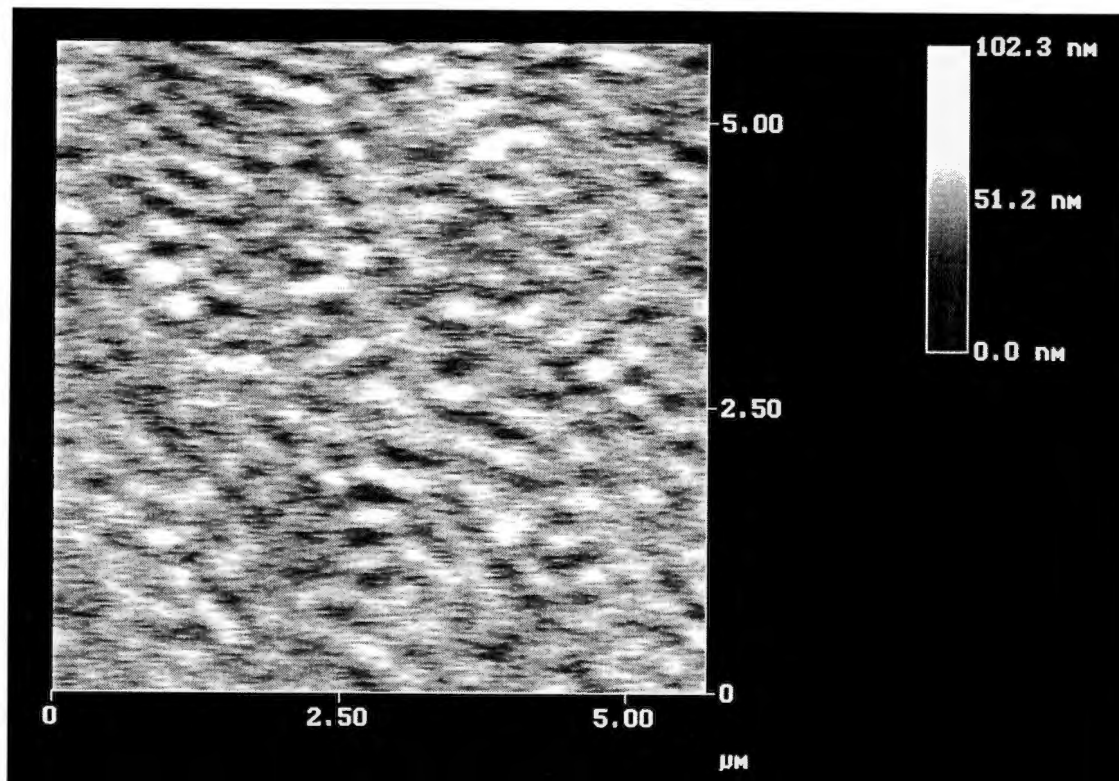


Figure 4.11: A 5.5 μm PSTM image of gold islands on a quartz substrate under s-polarization with a 632.8 nm laser at a 50° angle of incidence. The quartz is coated with 4.6 nm of gold and then heat treated for 6 minutes @ 800°C . Same area as Fig 4.10 over a larger scan range. The particles in this image appear ~ 240 nm in width.

544 nm

440 nm

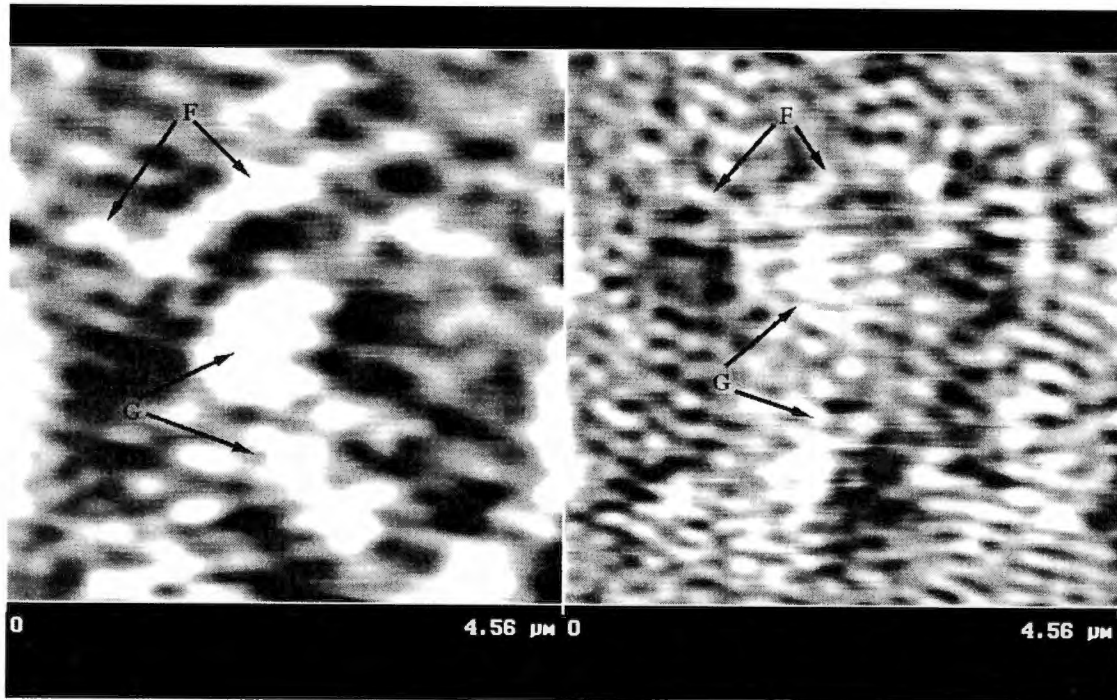


Figure 4.12: PSTM image of gold islands on quartz as imaged with a 544 nm laser (left) and 440 nm laser (right). The light was incident from an angle of 46°. The quartz is coated with 4.6 nm of gold and then heat treated for 6 minutes @ 600° C. The image area covered in the scan is the same. In the left image the particle sizes range from 185 nm to 260 nm and in the right image 82 nm to 155 nm.

show smaller particle sizes as this wavelength is farther from the resonance.

Next Fig. 4.13 through Fig. 4.16 show images that are comparisons of current mode to height mode. The current mode images show a better contrast because they plot the intensity of the field as the probe is scanned across the surface. This results in sharper field contrast than that obtained in height mode. In both images similar features are visible with just a slight offset. The similar areas are marked with corresponding letters.

Fig. 4.17 shows an example of gold islands on quartz as imaged with a SEM and Fig. 4.18 shows an image with an AFM. The particle sizes (30 nm to 80 nm) in the AFM images compare well with the PSTM image (82 nm to 155 nm) given in Fig. 4.15 and Fig. 4.16 which were obtained with the 440 nm HeCd laser. The images indicate that the HeCd gives a different map of the electromagnetic field. The difference in the images are a result of the 440 nm wavelength being further from the resonance position of the islands on the surface. This demonstrates that the particles total cross sectional area is smaller for 440 nm light.

The images of gold islands on quartz and mica demonstrate the imaging capabilities and versatility of the PSTM. Consideration must be made of the sample properties and the wavelength of the incident radiation used when imaging a sample. These images reinforce the fact that the PSTM produces an electromagnetic topographical map of the surface of a sample. The microscope in fact produces a map of the electromagnetic field strengths at any given point in the near zone whenever the polarizability is sufficient.

Current Mode

Height Mode

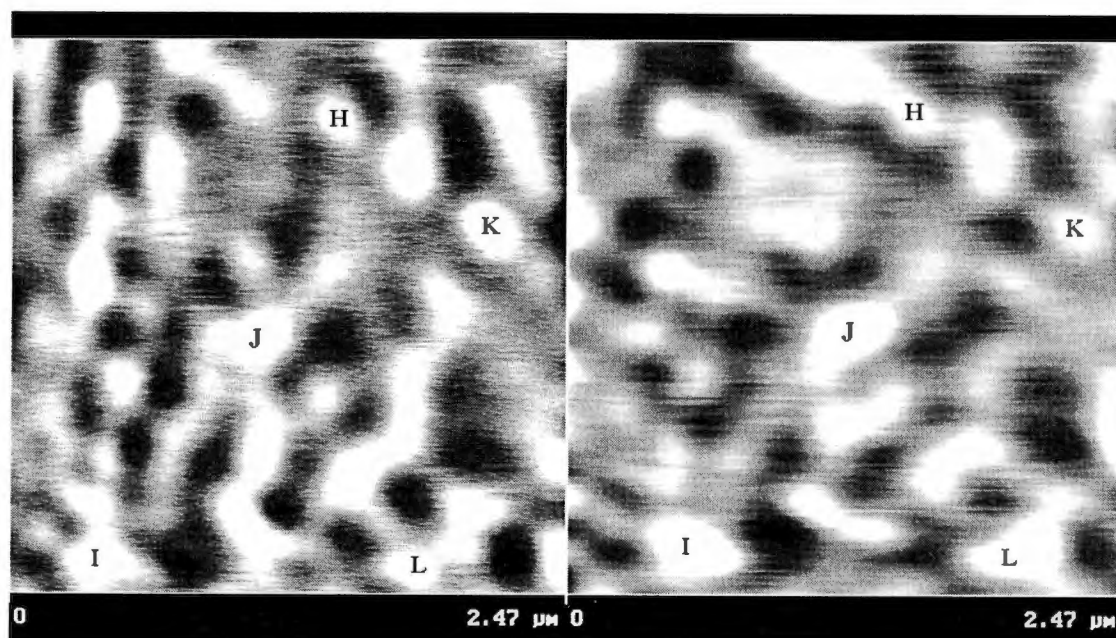


Figure 4.13: PSTM image made with a 544 nm laser in current mode (left) and height mode (right). Current mode keeps scans the tip across the surface in a straight line while in height mode the tip is kept at a constant tunneling signal. The light was incident from an angle of 46° . The quartz is coated with 4.6 nm of gold and then heat treated for 6 minutes @ 600°C . The image area covered in the scans is the same, but a slight offset exist between the images. In both images the particle sizes range from 175 nm to 220 nm.

Current Mode

Height Mode

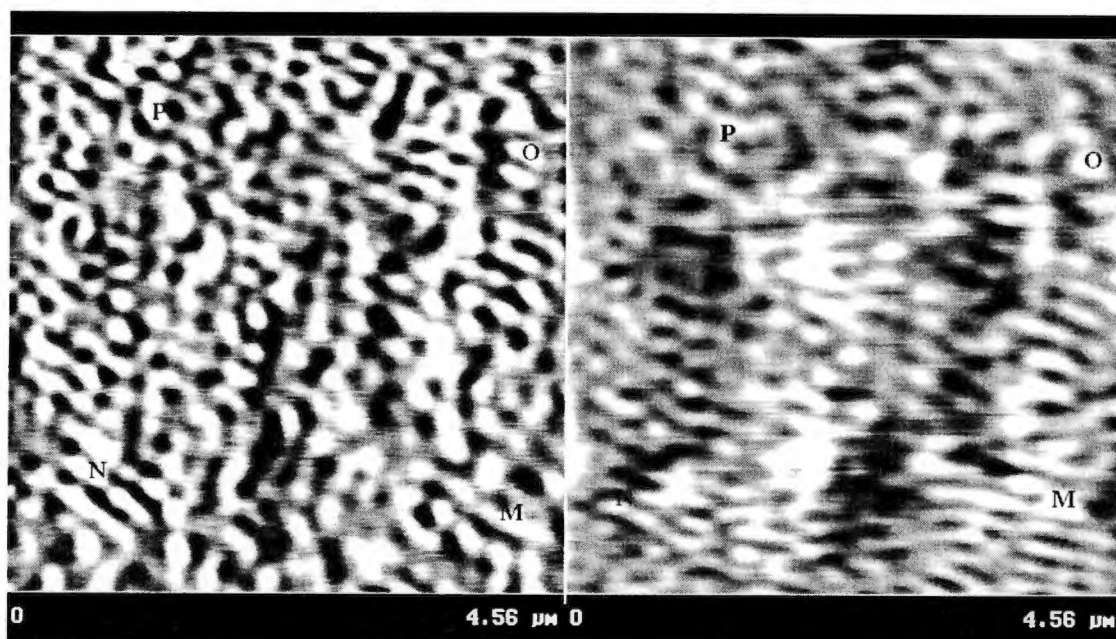


Figure 4.14: PSTM image of gold islands with a 440 nm laser in constant current mode (left) and constant height mode (right). Scans are over the same sample area. The light was incident from an angle of 46° . The quartz is coated with 4.6 nm of gold and then heat treated for 6 minutes @ 600°C . The image area covered in the scan is the same, but a slight offset exists between images. In the images the particle sizes range from 82 nm to 155 nm.

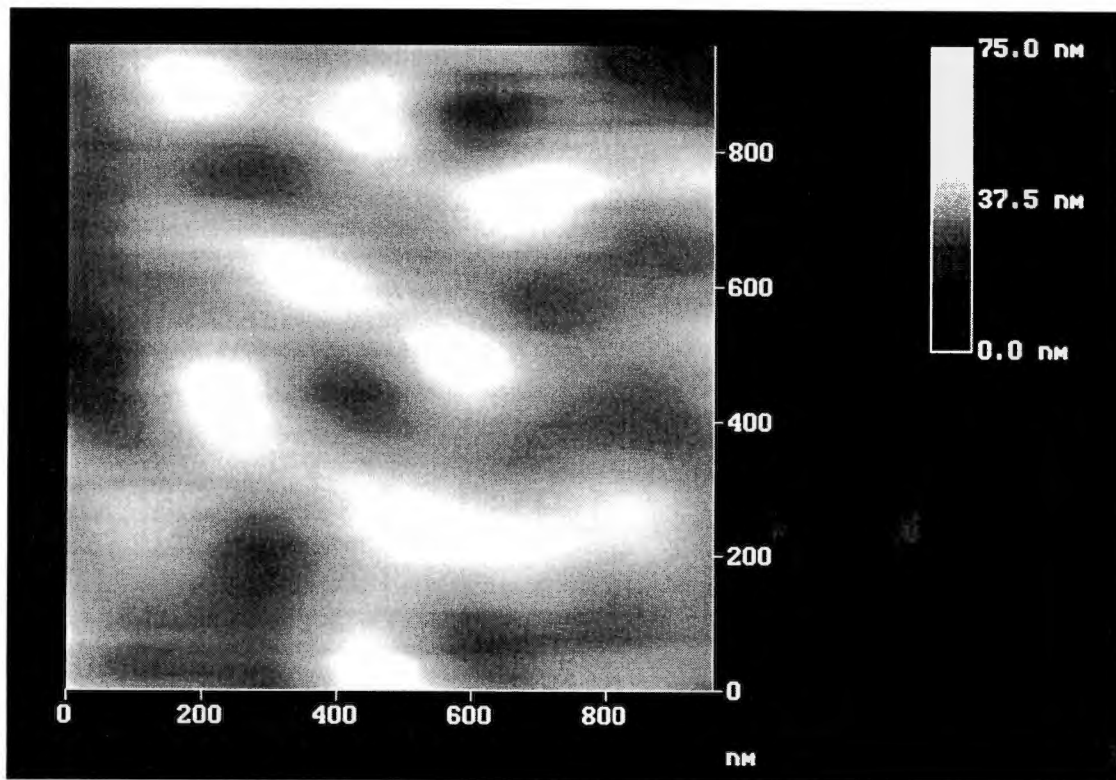


Figure 4.15: A $0.9\ \mu\text{m}$ PSTM image of gold islands on quartz with a $440\ \text{nm}$ laser in height mode. The light was incident from an angle of 46° . The quartz is coated with $4.6\ \text{nm}$ of gold and then heat treated for 6 minutes @ $600^\circ\ \text{C}$. The particle sizes range from $82\ \text{nm}$ to $155\ \text{nm}$.

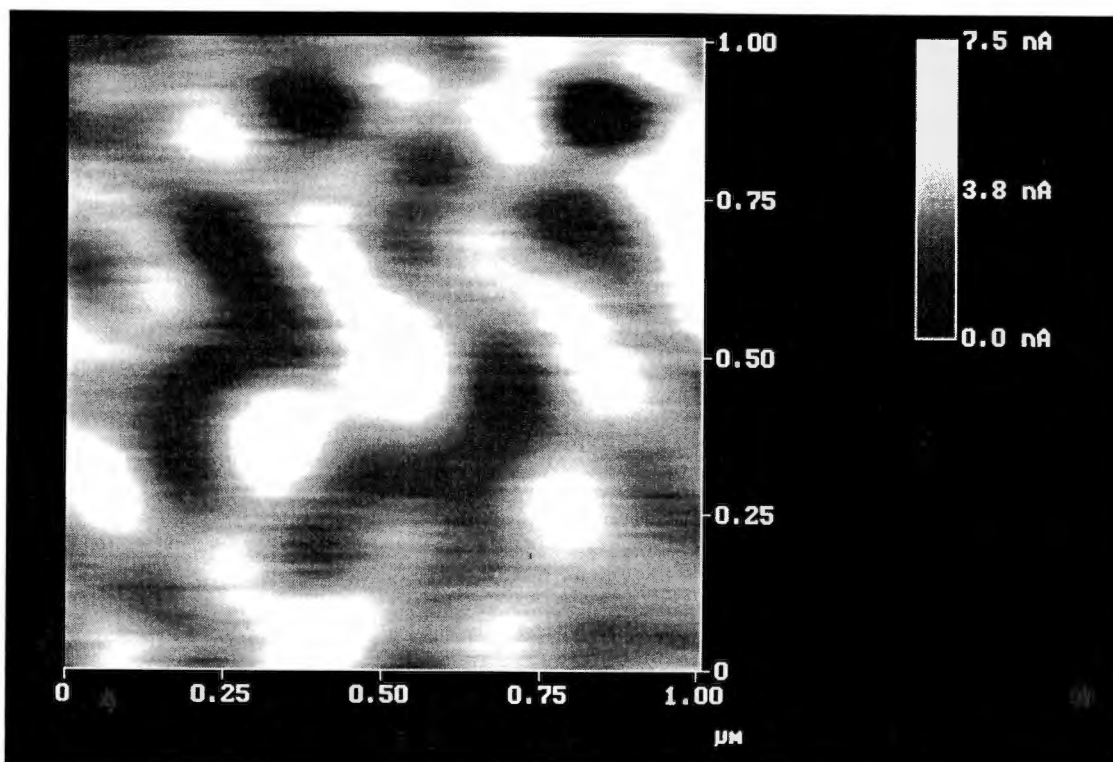


Figure 4.16: A 1.0 μm PSTM image of gold islands on quartz with a 440 nm laser in current mode. The light was incident from an angle of 46° . The quartz is coated with 4.6 nm of gold and then heat treated for 6 minutes @ 600°C . The particle sizes range from 82 nm to 155 nm.

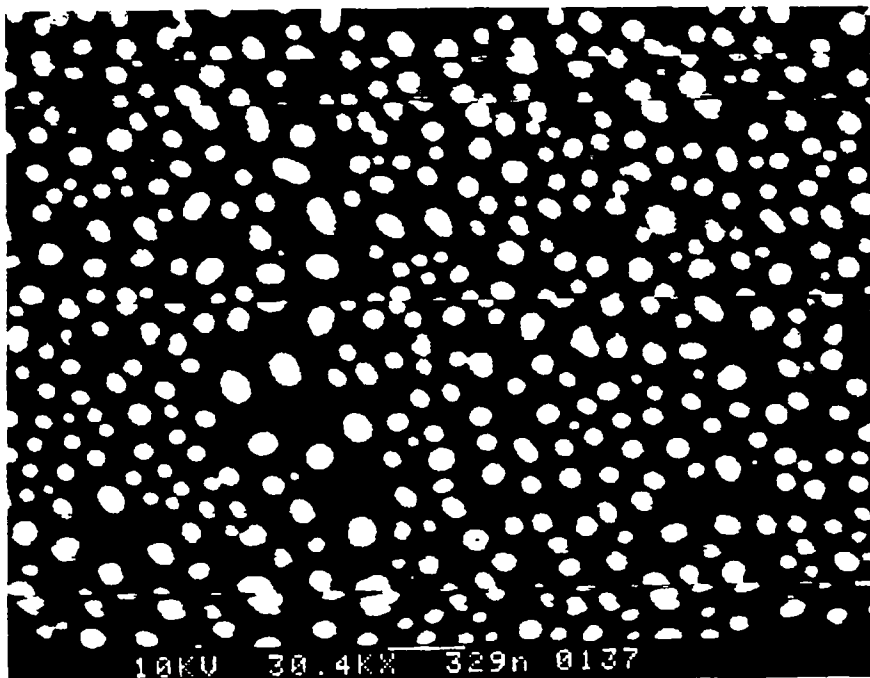


Figure 4.17: A SEM image at 30K magnification of gold islands on a quartz substrate annealed for 4 minutes @ 800° C. The particle sizes range from 30 nm to 100 nm.

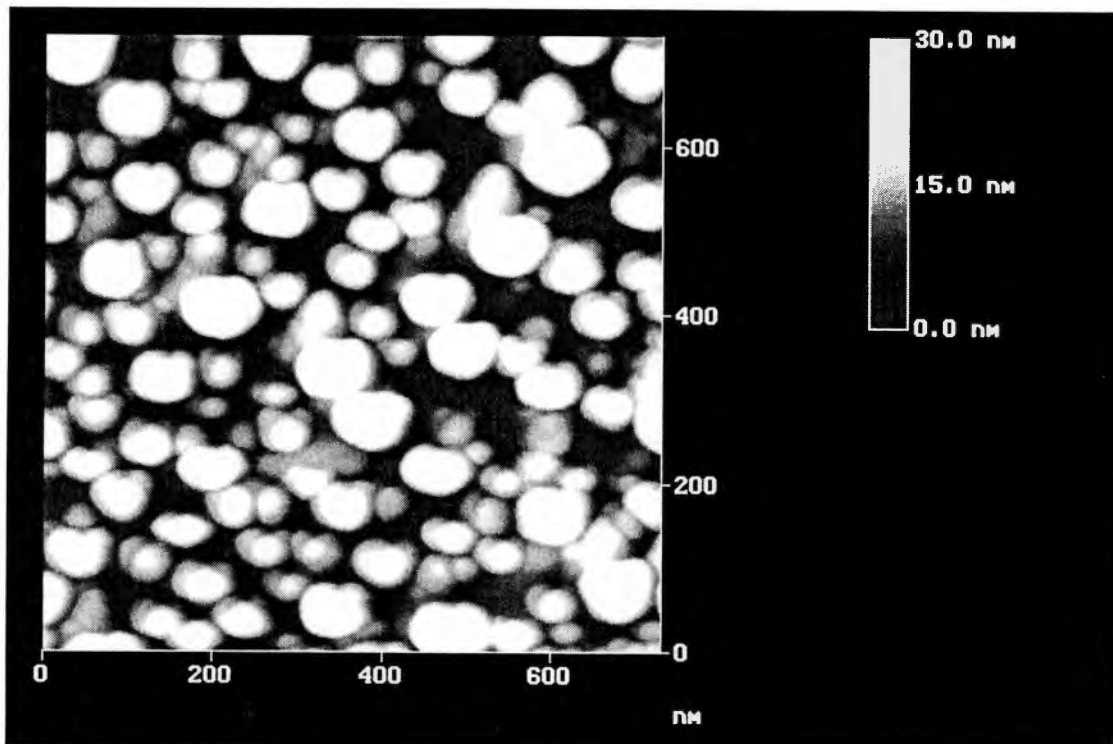


Figure 4.18: An AFM tapping mode image of gold particles on quartz 4.6 nm heated for 6 minutes @ 800° C. This a sample prepared in the same manner as the samples imaged with the PSTM and shown in Fig. 4.10 and 4.11. The particle sizes range 30 nm to 80 nm.

4.3 Spectroscopy of Gold Islands

Results are presented which demonstrate the ability of the PSTM to capture absorptive spectroscopic information. These results demonstrate the convenience of using the PSTM for spectroscopy is far simpler than in other scanned-probe measurement systems.

In Fig. 4.19 data taken with the Shimadzu® spectrophotometer (section 3.5.3) is shown for a sample of gold islands (5.0 nm of gold heat-treated for 5 minutes @ 200° C) on quartz and on mica. The results give an example of the absorption spectra associated with each case. In Fig. 4.19 a shift between the absorption data on the quartz sample and the mica sample can be observed which corresponds to the difference in substrate dielectric between the media. (Quartz $n^2 \sim 2.13$, Mica $n^2 \sim 2.49$) This shift is also observed between the spectroscopic cases studied with the PSTM.

4.3.1 Spectroscopy of Gold Islands on Mica

In this part of the experiment 4.6 nm of gold was evaporated onto mica which was heat-treated for 4 minutes at 147° C. A 632.8 nm HeNe laser with s-polarization was used for imaging and detection of the evanescent field. The white light source was a 73 Watt Quartz Halogen bulb, with no specific (random) polarization, that was focused to a small (~10 mm) spot on the surface of the sample. It was visibly under TIR conditions over the range of the spot. A schematic of the setup was given in

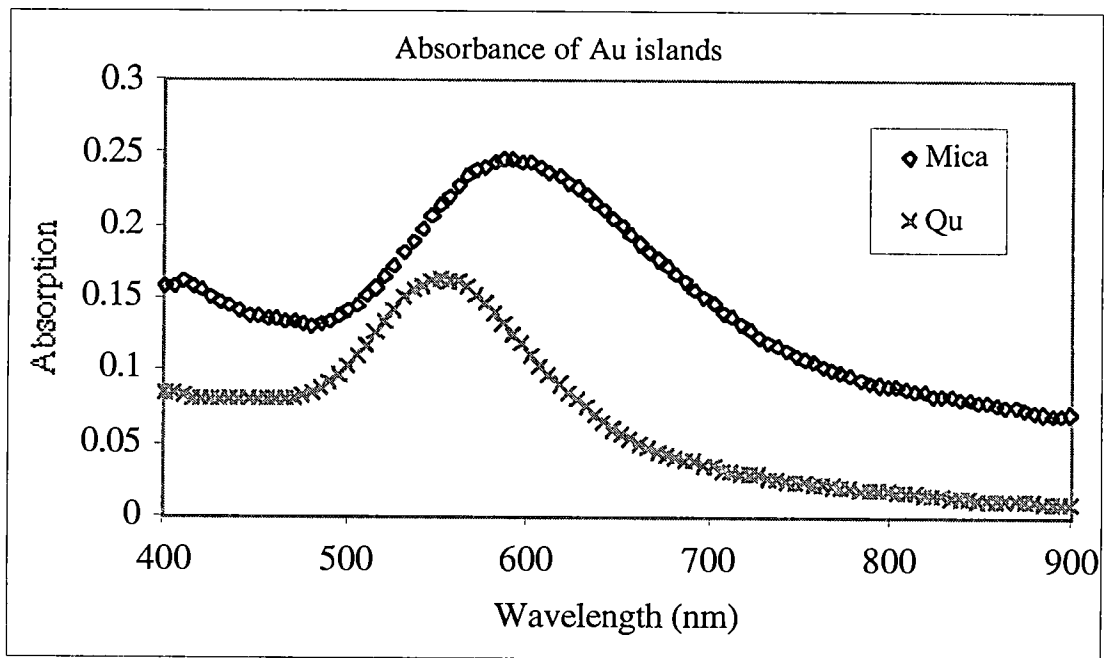


Figure 4.19: Absorption data for gold islands on Quartz and on Mica. A shift in the absorption peak caused by the different dielectric functions of the substrates can be seen. The index of refraction for Quartz is ~ 1.46 , while the index of refraction for Mica is ~ 1.59 . Only the area of the graphs between 400 nm and 680 nm will be seen in the PSTM spectroscopy images.

In Fig. 3.18 spectroscopic data was acquired with the Princeton Instruments® intensified diode array attached to the ISA Jobin Yvon® CP200 spectrometer shown in Fig. 3.10. The data was acquired over 90 runs of 0.989 seconds for a total time of ~90 seconds. A Corning® 125/50 multi-mode fiber, pulled to a point with a micropipet tip puller, was used as a probe.

First, the approximate position of the evanescent field was found by measuring the intensity of the tunneling signal for a HeNe 632.8 nm laser, as a function of probe movement along the z-axis, perpendicular to the surface. Once the evanescent signal was observed the voltage across the piezo that controls the movement in the z direction was recorded. The tip was retracted, the HeNe was turned off, the white light source turned on, and the tip was moved to the z voltage location that was previously recorded. A search was then made for the evanescent signal from the white light source. The intensity of the white light signal was less than the laser light but was located at a similar distance from the surface.

4.3.1.1 Gold Islands on Mica Data Set "A"

The intensity versus distance plot for the Gold Islands on Mica data set "A" is shown in Fig. 4.20. The figure shows the exponential decay of the signal which was checked by confirming that the log with respect to distance was a straight line. The #3 data was taken at the same location as the #1 data but the tip was moved closer to the surface and may have been broken. The higher background signal is an indication of a change in tip shape.

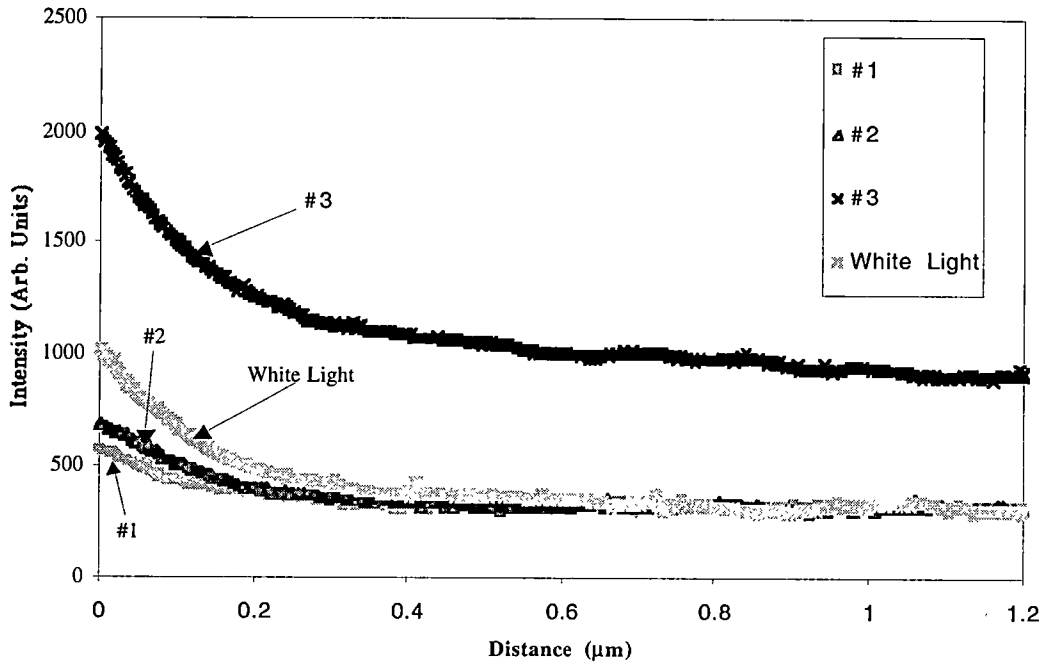


Figure 4.20: Plot of the evanescent signal intensity (arbitrary units) vs. distance (μm) for different locations of the sample. The higher background signal in #3 is an indication of a change in tip shape.

Once the signal due to evanescent field of the white light source was observed the signal was used to control the separation between the probe tip and the surface. This distance was maintained by keeping the measured tunneling signal constant. The position of the tip was moved to different locations of the surface and data was taken over a ~90 second time period.

To account for differences in signal intensity caused by the uncertain distance to the surface the data was "normalized" to the 410 nm to 419 nm portion of the white light reference spectrum. The 410 nm to 419 nm portion of the spectrum was chosen because the absorption should be very low if not zero in this location. This normalization was also needed because the reference white light spectrum, which was taken over a clean mica slide, was measured in a different experimental run and at a different separation from the surface. The results of the normalization can be seen in Fig. 4.21 where the intensity of the signal is plotted as a function of the wavelength. The normalization removes information about the absolute absorption intensities but allows for a comparison of absorption peak position. Data in the figure was smoothed by summing over 8 data points (This corresponds to a 3.8 nm range in the detector which is comparable to the spectrometers resolution.).

The absorption was calculated summing over 8 data points and the negative log of the spectrum over gold islands divided by the spectrum over plain mica was calculated to obtain the absorption. In Fig. 4.22 the absorption is given versus wavelength for three different data sets and the data is overlaid with a 6-order polynomial fit. In Fig. 4.23 theoretical absorption peaks, calculated using the absorption calculation

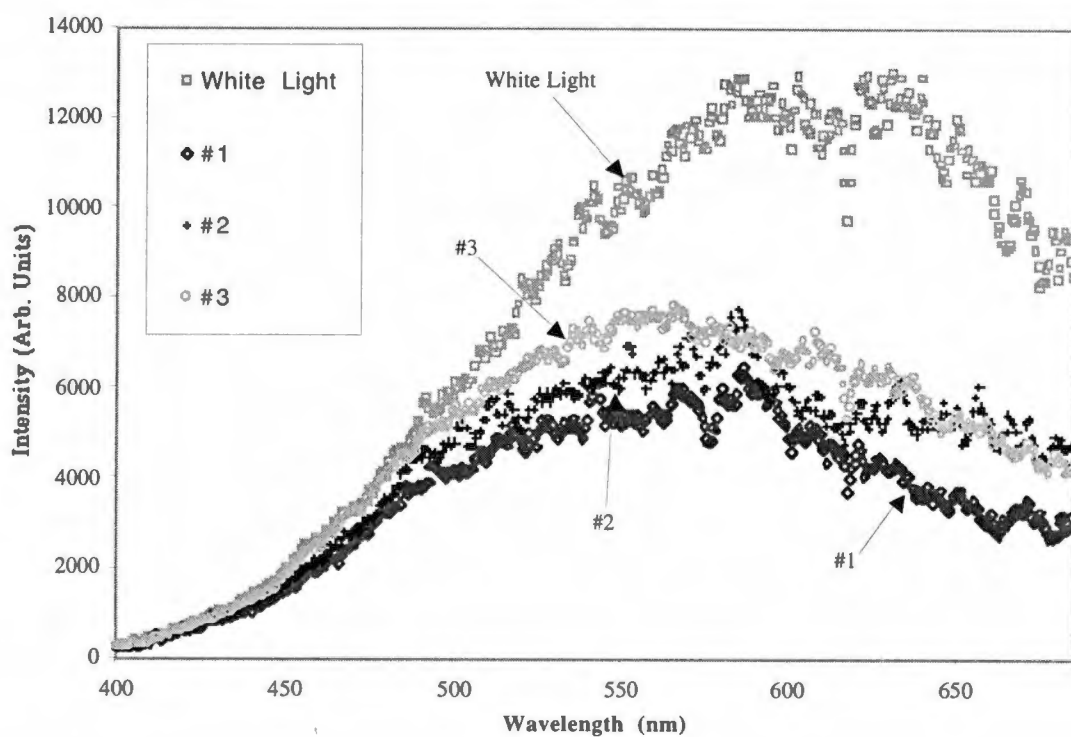


Figure 4.21: Scaled transmission intensity values for the gold islands on mica data set of gold islands on a mica substrate. A 4.6 nm layer of gold was evaporated onto mica which was heat treated for 4 minutes at 147° C. The data sets were normalized to match over the 410 to 419 nm range of the spectrum because the absorption should be a minimum in this location.

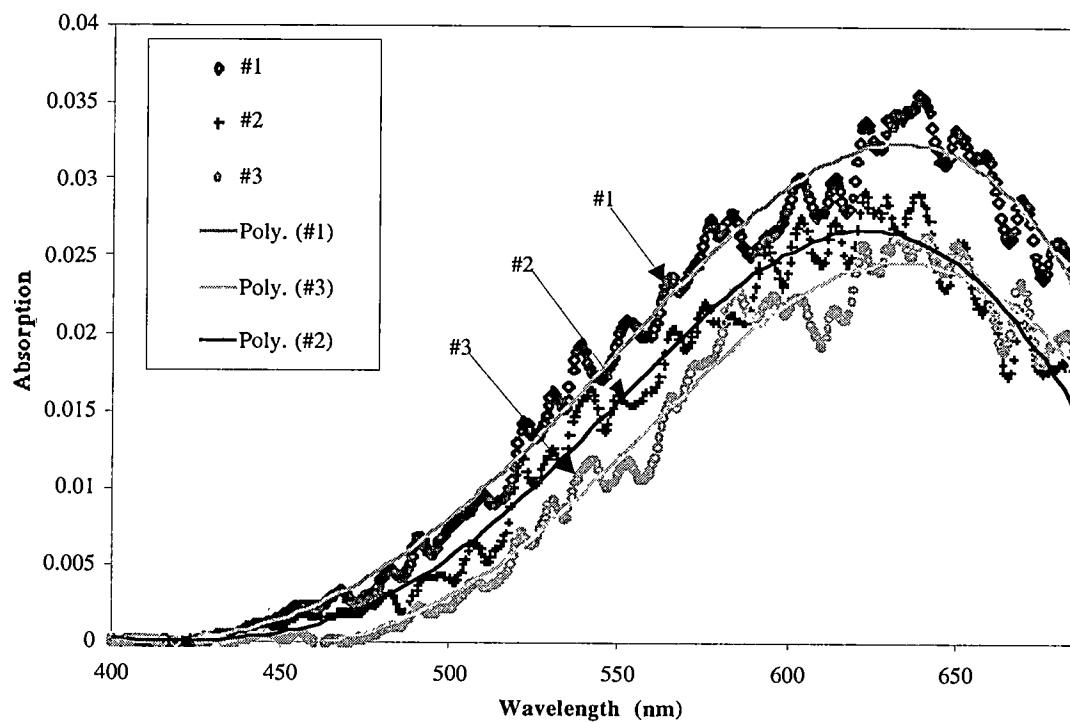


Figure 4.22: Absorption data for gold islands on mica data set "A". A 4.6 nm layer of gold was evaporated onto mica which was heat-treated for 4 minutes at 147° C. The absorption data has been smoothed and then fitted with a 6th order polynomial. Curve #2 is from a different location on the sample than #1 and #3. Data sets #1 and #3 were taken at the same position over the surface of the sample with the tip moved closer to the surface for sample #3.

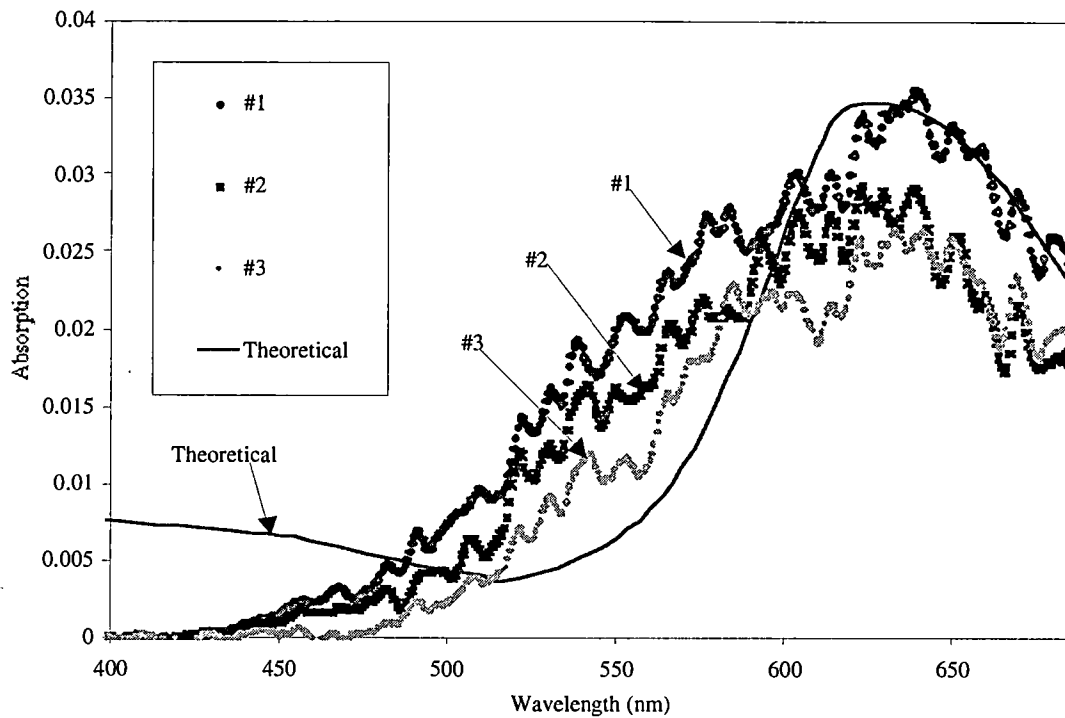


Figure 4.23: Absorption results for the gold islands on mica data set "A" compared with theoretical calculations. The theoretical absorption is for a "gaussian" distribution of particles centered at $R_0=0.2$ with a distribution $\Delta R=0.1$, surrounded by a dielectric function $\epsilon=1.7$, and light incident at an angle of 47° . (Very low white light signal in the 400 nm to 450 nm range so the theory and experiment do not match well in this location. Also normalized in that area so information from that section would be washed out.)

presented in section 2.2, are shown with the data. The dielectric function was set to the average value for mica and air to approximate the fact that the islands sit on the interface.

4.1.1.2 Gold Islands on Mica Data Set B

The following data sets, labeled "B1" and "B2", were prepared following the same method used for data set "A". A sample of 4.6 nm of gold was evaporated onto mica which was heat-treated for 4 minutes at 147° C. A 632.8 nm HeNe laser with s-polarization was used for imaging and for detection of the evanescent field. The white light source was a 73 Watt Quartz Halogen bulb, with no specific (random) polarization, that was focused to a small (~10 mm) spot on the surface of the sample. It was visibly under TIR conditions over the range of the spot.

In Fig. 4.24 the scaled intensities for the "B1" data set are presented and the absorption spectrum is shown in Fig. 4.25. A difference between the shape of the signals is seen in both figures. A plot of the absorption overlaid with theoretical absorption plots is given in Fig. 4.26. The theoretical values were generated using the theory presented in section 2.2. The relative heights of the theoretical absorption have been modified by a multiplicative factor for scaling purposes.

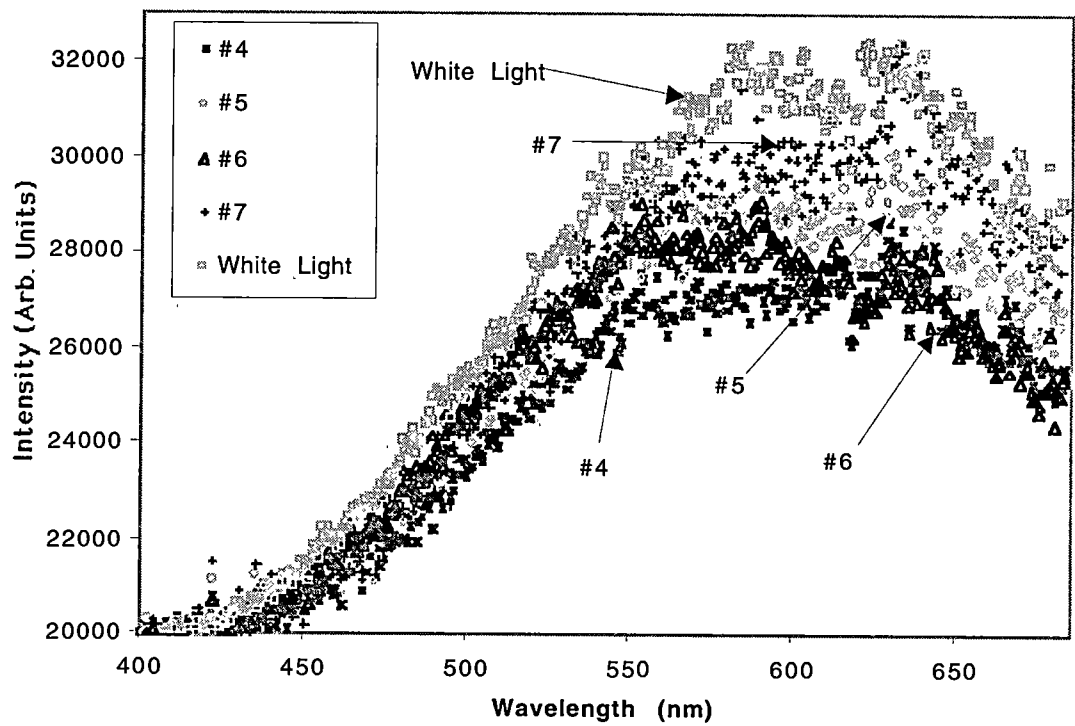


Figure 4.24: Scaled transmission intensity values for the "B1" data set of gold islands on a mica substrate. A 4.6 nm layer of gold was evaporated onto mica which was heat treated for 4 minutes at 147° C. The data sets were normalized to match over the 410 to 419 nm range of the spectrum.

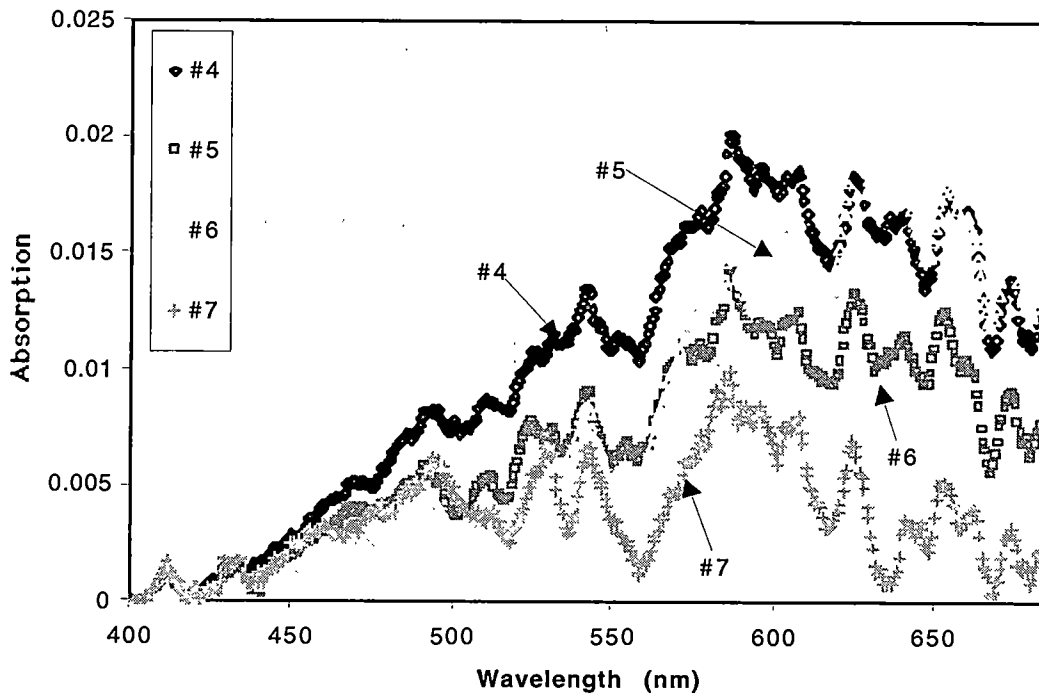


Figure 4.25: Absorption data for data set "B1" of a sample of gold islands on mica. A 4.6 nm layer of gold was evaporated onto mica which was heat-treated for 4 minutes at 147° C. The absorption data has been smoothed.

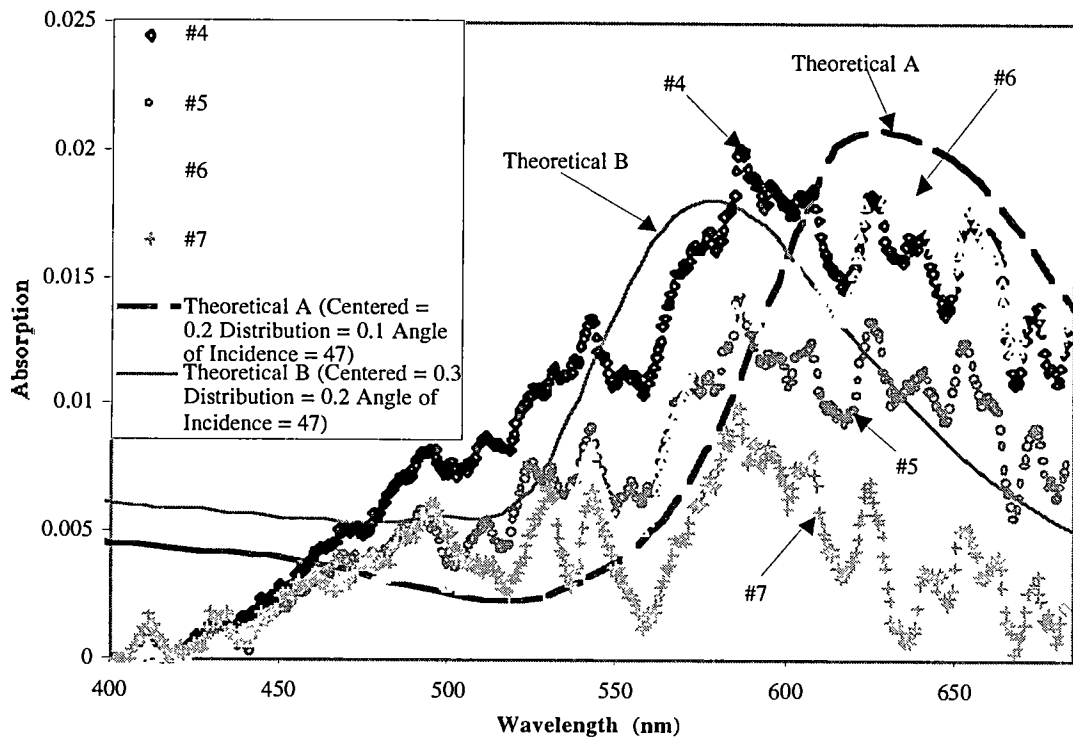


Figure 4.26: Absorption results for the "B1" data set compared with theoretical calculations. The theoretical absorption is for a "gaussian" distribution of particles centered at $R_g=0.3$ and 0.2 with a distribution $\Delta R=0.2$ and 0.1 respectively, surrounded by a dielectric function $\epsilon=1.7$, and light incident at an angle of 47° .

The intensity vs distance plot for the "B2" data set is shown in Fig. 4.27. The figure shows the exponentially decay of the signal. The exponential nature of the signal was checked by confirming that the log of the signal with respect to distance was a straight line. The scaled transmission for the "B2" data set are presented in Fig. 4.28 with the absorption shown in Fig. 4.29. This data also demonstrates a shifting in the absorption peak for different locations of the sample. In Fig. 4.30 the absorption curves are overlaid with a theoretical absorption curve for a distribution of particle shapes.

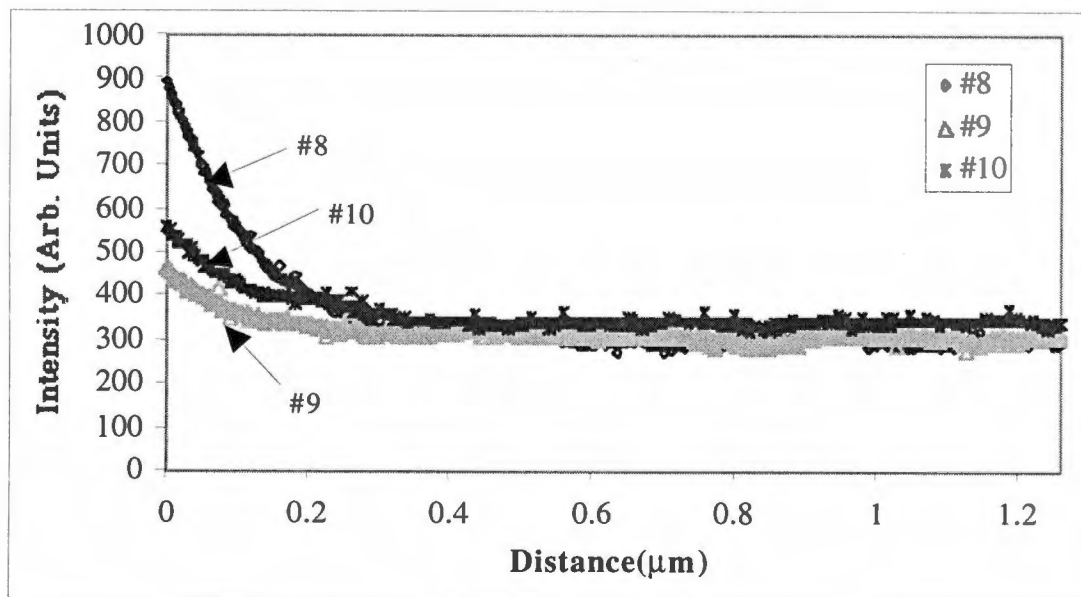


Figure 4.27: Plot of the evanescent signal intensity (arbitrary units) vs. distance (μm) for different locations of the sample for the "B2" data set.

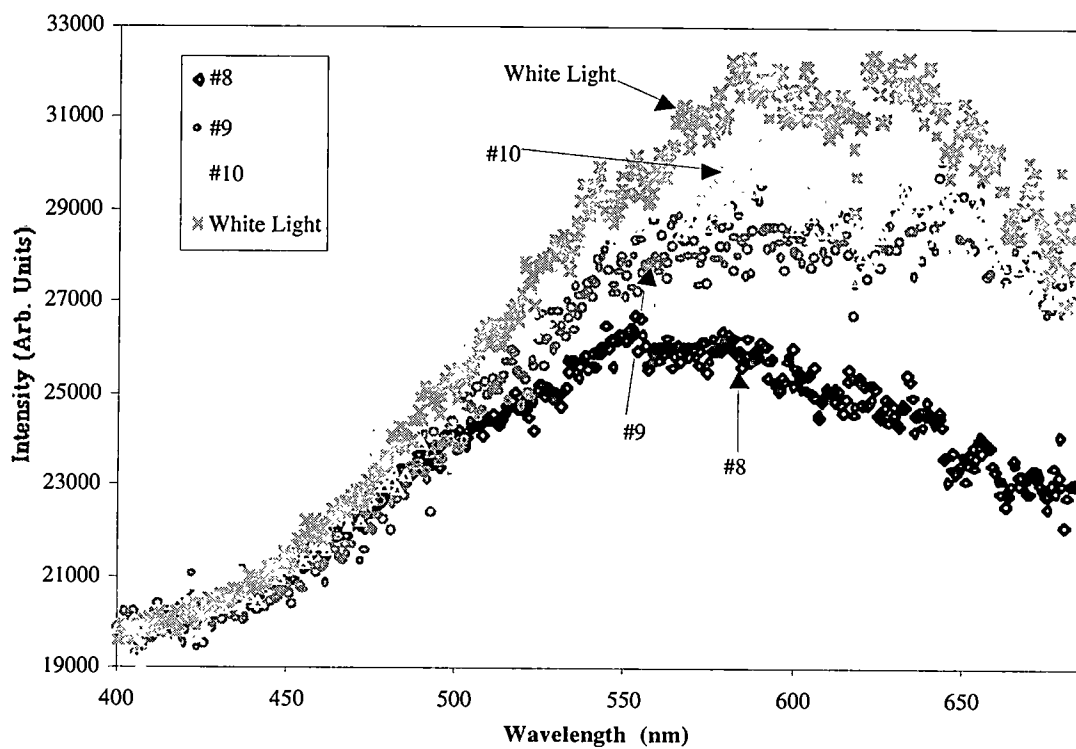


Figure 4.28: Scaled transmission intensity values for the "B2" data set of gold islands on a mica substrate. A 4.6 nm layer of gold was evaporated onto mica which was heat treated for 4 minutes at 147° C. The data sets were normalized to match over the 410 to 419 nm range of the spectrum because the absorption should be a minimum in this location.

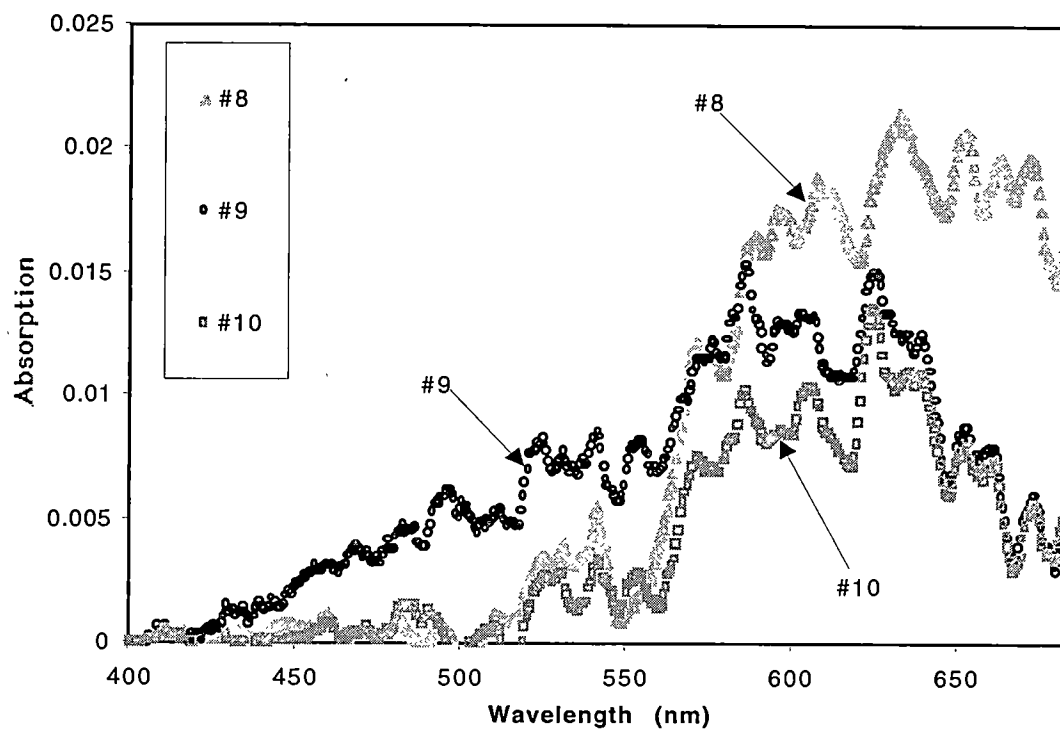


Figure 4.29: Smoothed absorption curves for the "B2" data set for different location of the sample of gold islands on mica. A 4.6 nm layer of gold was evaporated onto mica which was heat-treated for 4 minutes at 147° C.

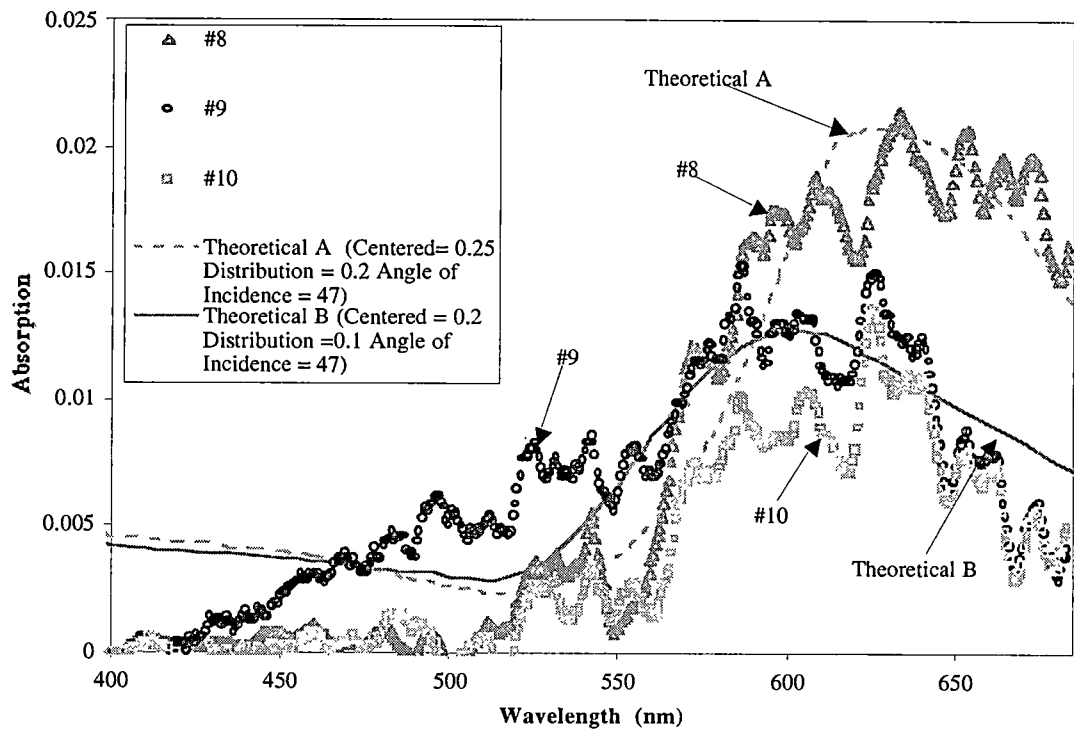


Figure 4.30: Absorption results for the "B2" data set compared with theoretical calculations. The theoretical absorption is for a "gaussian" distribution of particles centered at $R_0=0.25$, and 0.2 with a distribution $\Delta R=0.2$, and 0.1 for both values of R_0 , surrounded by a dielectric function $\epsilon=1.7$, and light incident at an angle of 47° .

4.1.2 Spectroscopy of Gold Islands on Quartz

The absorption spectrum peak for gold islands on quartz is located at 560 nm which is shifted from the data on mica. This shift is due to the difference in the index of refraction between mica ($n \sim 1.59$) and quartz ($n \sim 1.46$). The absorption peak in the figures is sharper than with the mica data. This is because the sample used was heated at a higher temperature (500°C) for a longer time (5 minutes), therefore the islands that were formed are much rounder and have a smaller distribution of shapes.

The data was normalized to the 410 nm to 419 nm portion of the white light spectrum. In this location the absorption should be very low if not zero. The normalized signal was then summed over 8 data points and the negative log of the spectrum over gold islands divided by the spectrum over plain quartz was calculated to obtain the absorption.

A clean fused silica cover slip placed onto the plano convex lens was used for the white light sample. The gold island sample was produced on a fused silica cover slip coated with 4.0 nm of gold. The gold sample was then baked for 5 minutes at 500°C to create the islands.

The scaled intensity values for this data set are shown in Fig. 4.31 followed by the absorption in Fig. 4.32. The peak absorption is located around 560 nm which is shifted from the peak observed in the mica results (625 nm). The absorption is compared to theoretical curves and the absorption obtained with the Shimadzu® Spectrometer in Fig. 4.33. In this figure the theory and experimental results show good agreement.

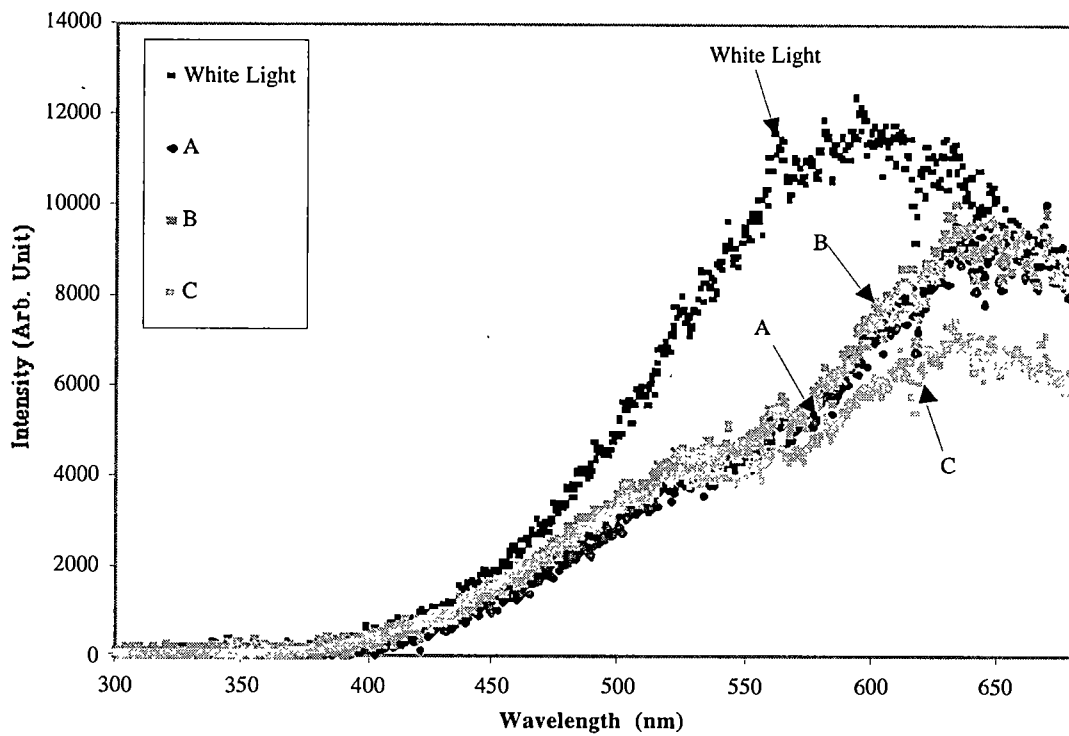


Figure 4.31: Tunneling intensity of the gold island over quartz data. The data sets were normalized to the white light signal between 410 to 419 nm. It can be seen that the shape of the scaled data matches up at both sides of the spectrum for the "A" and "B" data.

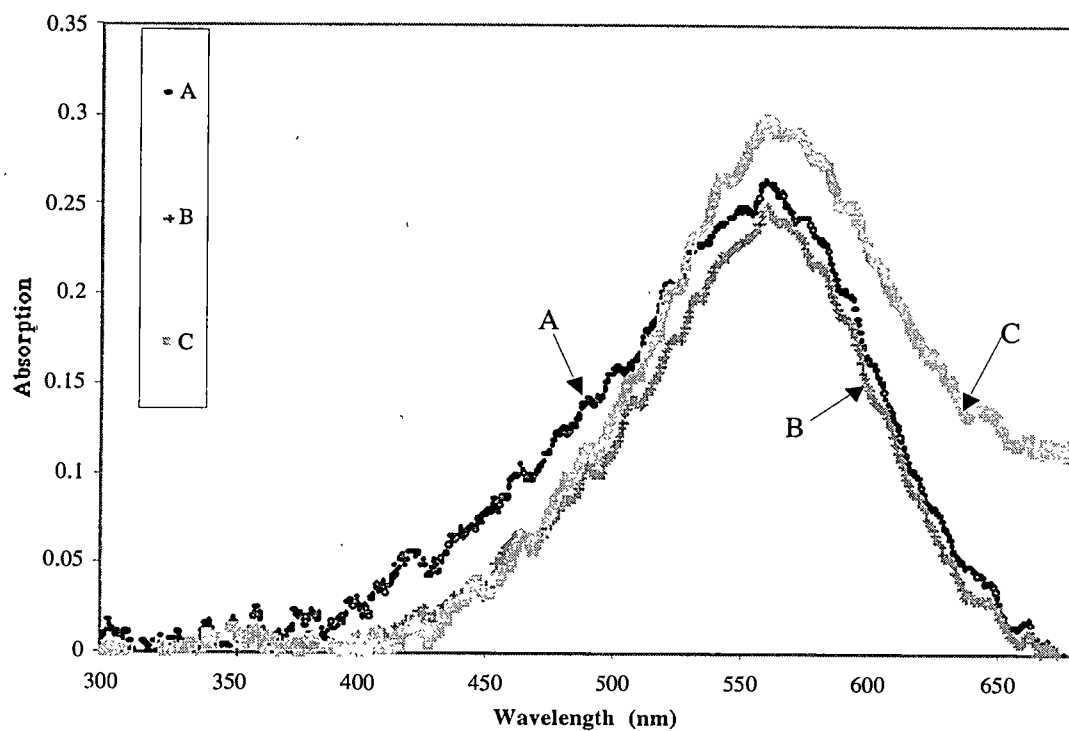


Figure 4.32: Absorption spectrum for 4.0 nm of gold heat-treated for 5 minutes at 500°C on a quartz substrate. The "A" and "C" data were taken from the same position. The difference between the scans was the set point used for each set of data. The tip was closer to the sample during the "C" data collection period.

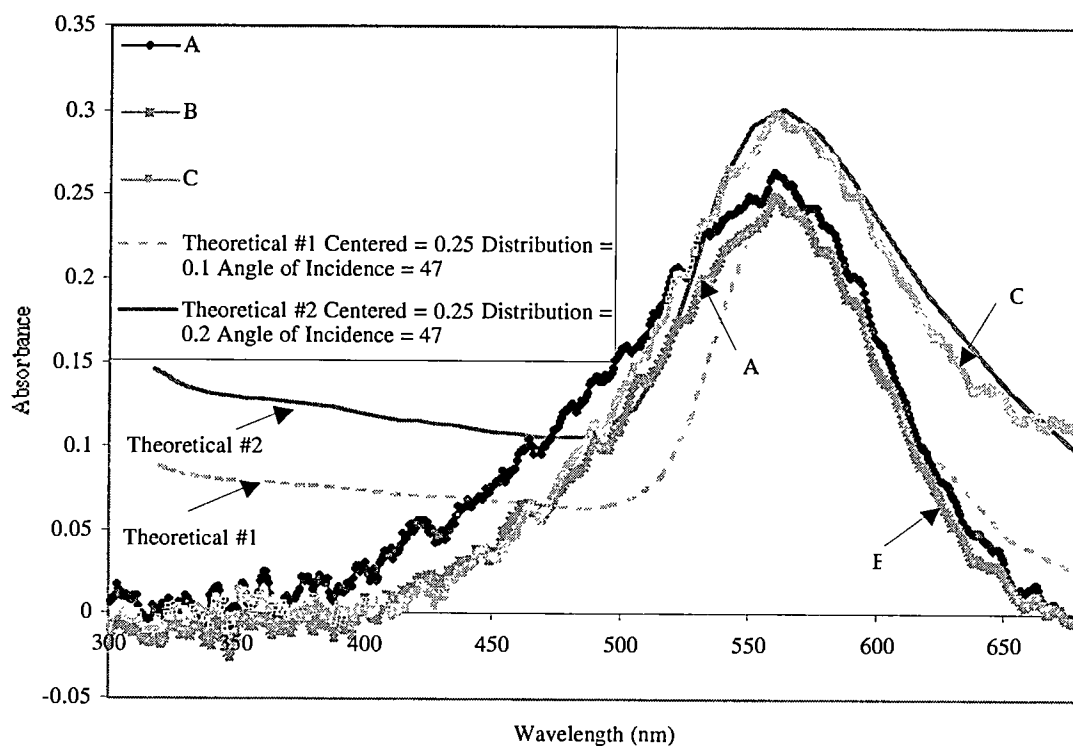


Figure 4.33: Absorption spectrum with theoretical overlays for 4.0 nm of gold heat-treated for 5 minutes at 500° C on a quartz substrate. The "A" and "C" data were taken from the same position. Theoretical values were overlaid onto the experimental values.

The measurement of absorption spectroscopy is a major improvement to the PSTM analysis process. It demonstrates that the white light signal is strong enough to conduct spectroscopy. It is still not strong enough and stable enough to provide concurrent imaging, but as this experiment demonstrated a secondary light source could be used to collect topographic images.

4.4 Two-Photon Excitation Experiment

The goal of the two-photon experiment is to determine the feasibility of modifying the PSTM into a new type of microscope called a NSPM. Measurements are presented which demonstrate the ability to detect the nonlinearly excited signal with the fiber probe. Results of metal coated and uncoated fiber probes are presented for varying conditions.

The results given in the following pages are from different experiments that were designed to test the ability of the PSTM to collect and study the two-photon excitation effect. All samples consist of yellow dye spun coated onto a quartz slide.

4.4.1 Characterization of Yellow Dye

Yellow dye was placed on a quartz slide and excited with a UV lamp whose spectral distribution is shown in Fig. 4.36. The sample and source were placed in front of a HR-640 monochromator and a silicon photo diode that was monitored with an AD board connected to a computer for data storage recorded the fluorescence signal. The fluorescence signal for the dye is given in Fig. 4.35. The recorded fluorescence signal

shows that the yellow dye has 2 large peaks at 525 nm and 736 nm and a much smaller peak at 406 nm. It is the 524 nm (green) peak that will be measured in the experiment.

The absorption of the yellow dye was measured and is shown in Fig. 4.37. A xenon arc lamp was used to illuminate the sample for the absorption measurement. The absorbance curve ($Abs = -\log(I/I_0)$) is displayed as a function of wavelength. It can be seen from this graph (Fig. 4.37) that the yellow dye readily absorbs light in the 400 nm to 500 nm region of the spectrum. This is the region of the frequency doubled wavelength (390 nm) of the Ti:Sapphire laser used in the experiments described.

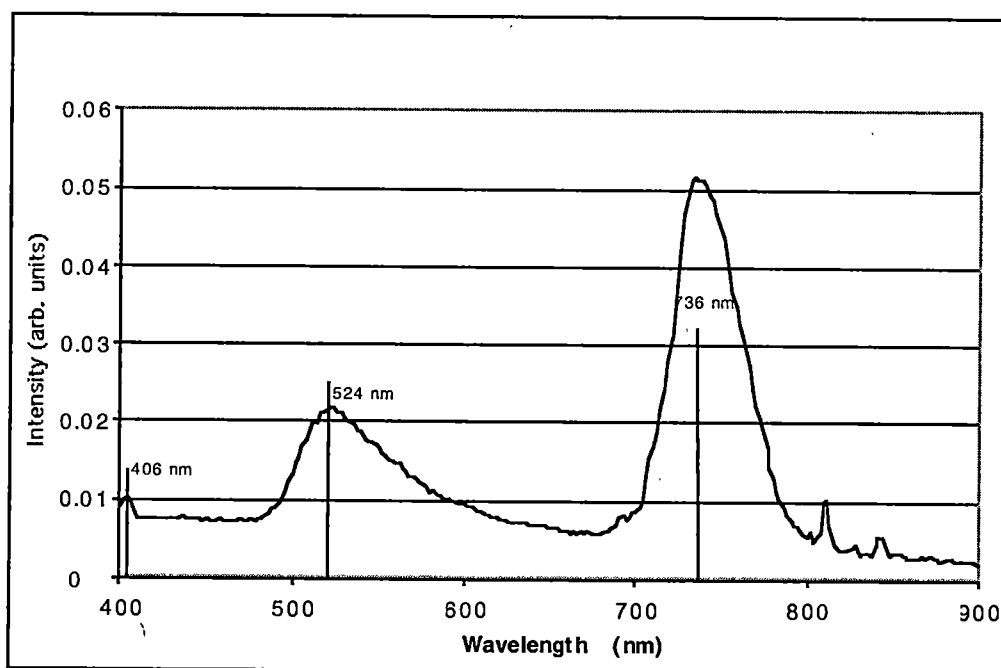


Figure 4.34: Fluorescence of the yellow dye when illuminated with a 366 nm light source. The intensity is in arbitrary units and the values correspond to the voltage readings on the silicon photo detector.

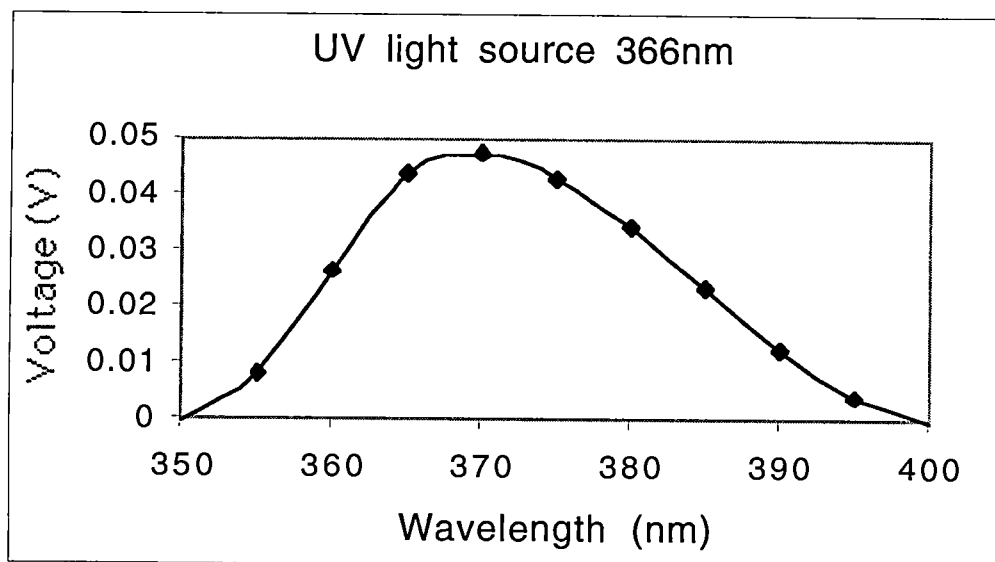


Figure 4.35: Spectral distribution of the UV lamp used to excite the dye during initial testing.

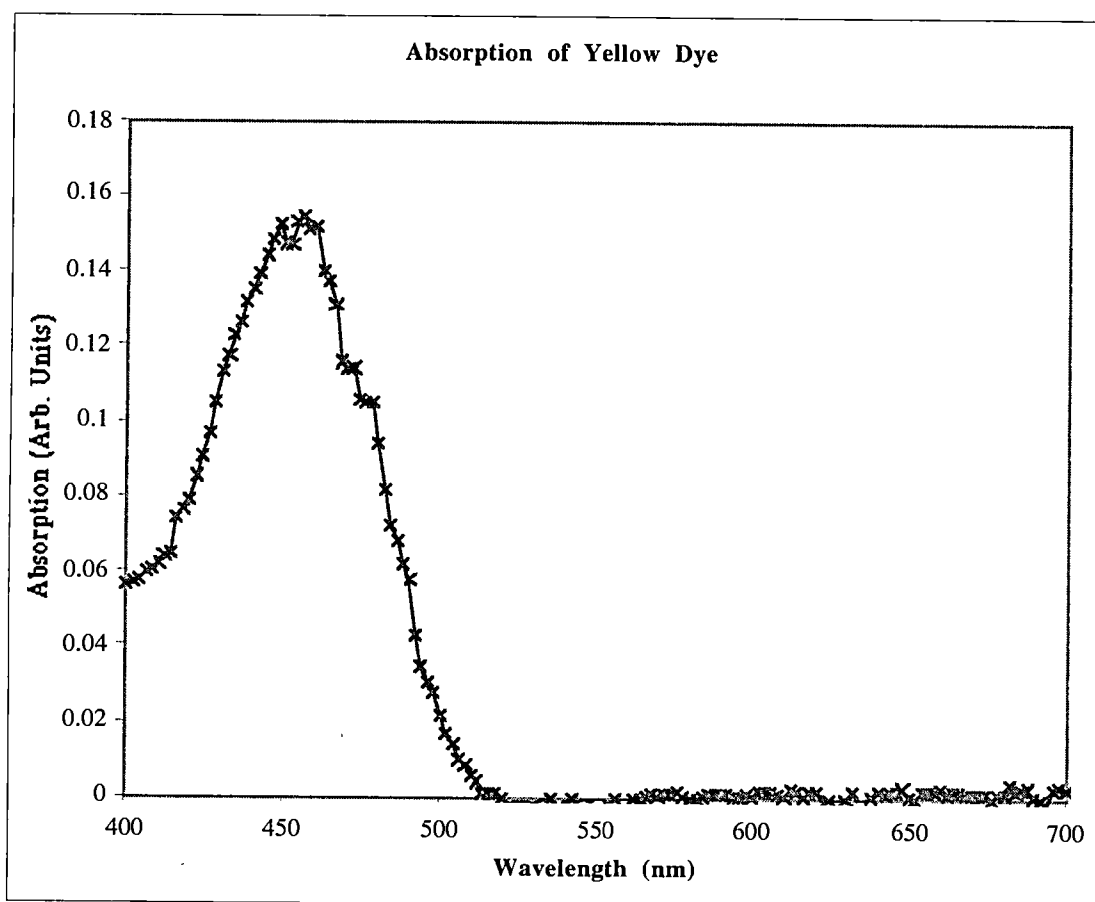


Figure 4.36: Absorption of the yellow dye over the visible spectrum of light. This data was taken with the HR-640, silicon detector and a xenon arc lamp source.

4.4.2 Two-Photon Data Sets

In the two-photon measurements given below the Ti:Sapphire laser beam was focused to a 1 mm spot on the surface of the sample. This focus for the beam was chosen so that no green light (fluorescence) could be seen through a #8 colored glass filter with the naked eye. This was determined to be the lower limit of two-photon excitation for a 127 mW pump energy. The coated probes used were coated with 62.4 nm of gold while being rotated.

The probe tip was held at a constant height very close to the surface and measurements were taken as the pump laser's intensity was increased. The observed intensity increase of the fluorescence signal was plotted versus the pump intensity in Fig. 4.37. The figure shows that the signal was very weak or zero up until 127 mW of pump intensity. After this point was reached the fluorescent signal increased considerably. This is also shown in Fig. 4.38 where the log of the intensity vs the log of the pump power is plotted. Straight lines have been fitted to the section below 127 mW pump intensity and the section above. For a two-photon signal a log-log plot is expected to have a slope of 2.

In Fig. 4.39 results for a coated probe at a fixed position above the sample surface are presented. The probe was coated with 60 nm of gold while being rotated and was held at a fixed position in the evanescent field of the HeNe 632.8 nm laser. The signal was collected with the HR-640 centered on the 520 nm wavelength while the incident pump intensity was varied.

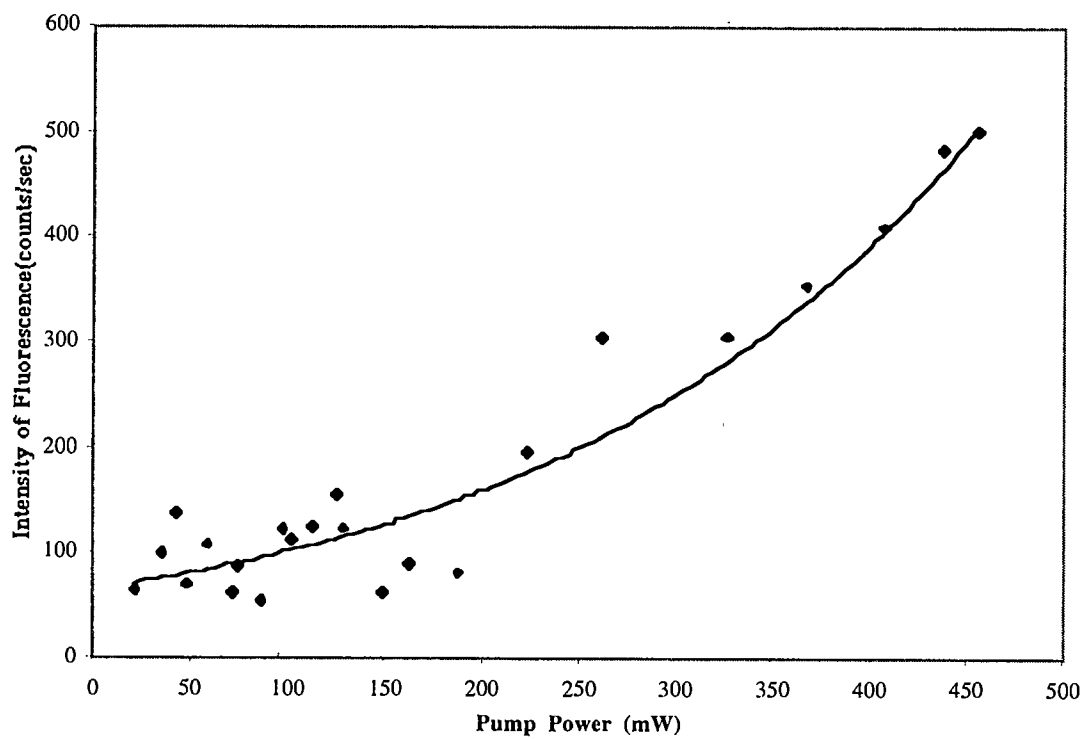


Figure 4.37: Plot of the intensity as a function pump intensity for a probe held at a fixed distance from the surface of the sample. A two-photon signal is not detected until the pump power reaches ~ 126 mW.

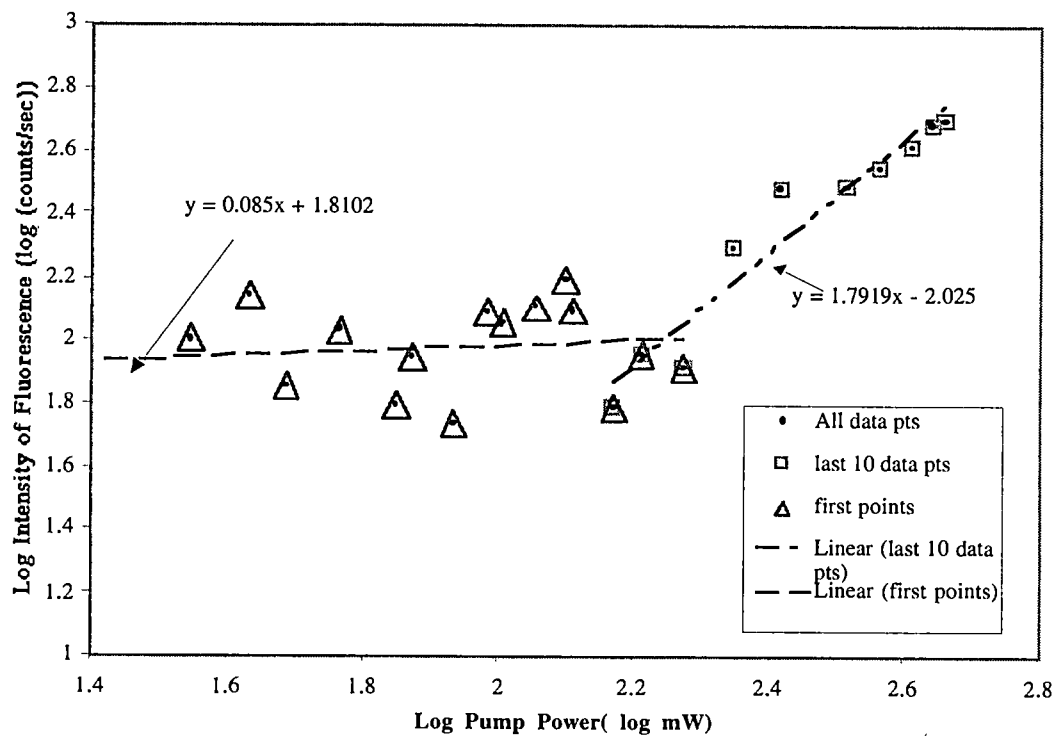


Figure 4.38: Log plot of the intensity as a function of the pump intensity for a probe held at a fixed distance from the surface of the sample which has the data separated into two sections. The last 10 data points occur above the point where the two-photon effect should be observed with or without enhancement. A slope near 2 can be found for this section.

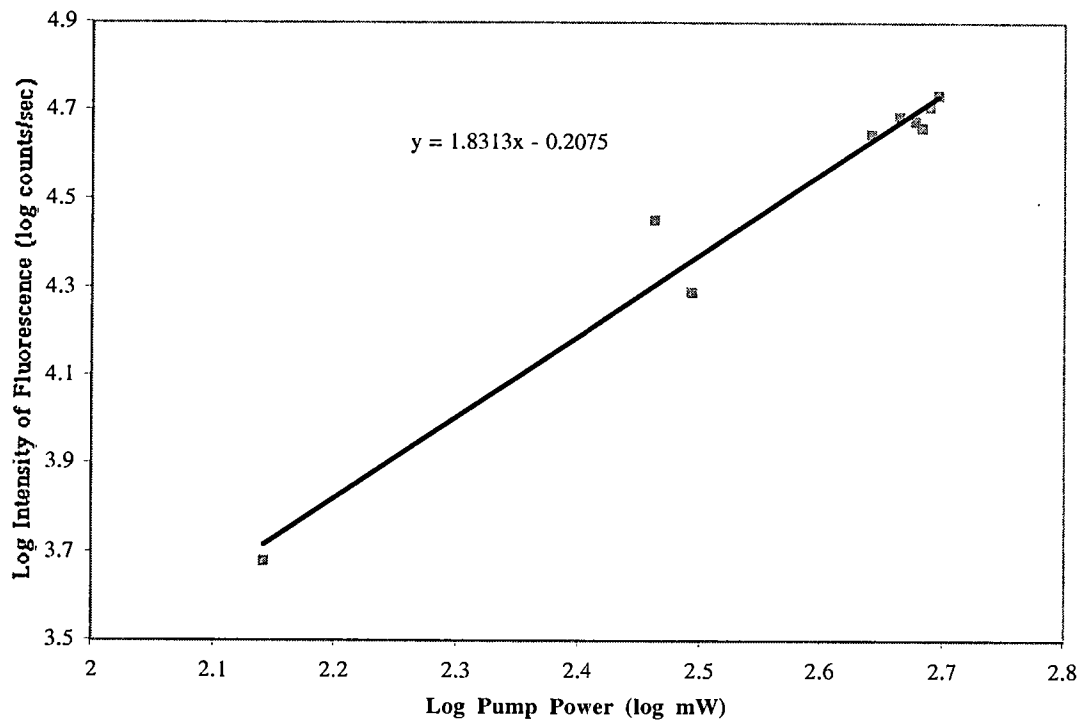


Figure 4.39: Log-log plot of two-photon fluorescence signal as a coated probe tip is held at a fixed position above the sample surface.

The results shown in Fig. 4.38 and Fig. 4.39 clearly indicate that the effectiveness of the metal-coated probe in enhancing the local energy density of the evanescent field is limited at the probe-to-sample distances explored. In order to see these effects, which are of inverse sixth power in the distance superimposed upon the usual exponential decay, the probe would need to be positioned within 1-2 nm of the sample during the scan. As this becomes technologically feasible for the mechanisms of scanned probe instruments in the probing of rough surfaces, it would permit a much better resolution over conventional PSTM. In particular, it should be possible to locate individual fluorophores placed as taggants on DNA base pairs or other sites on biologically significant samples.

In Fig. 4.40 a graph of the fluorescent signal as a function of probe tip movement in the z-direction is presented. A coated probe tip (60 nm) was moved towards the sample surface (by adjusting the tunneling signal of the 632.8nm laser) while monitoring the fluorescent signal. The pump laser power was set to 281 mW which was just at the point of visible two-photon excitation. (The lens had been adjusted for this experiment so the pump energy needed for fluorescence was higher than the 127 mW reported for the earlier results.) As the probe is moved toward the surface the signal increases but it cannot be determined from this graph if any enhancement of the signal by the metal-coated probe took place. This graph does show the ability to detect the fluorescence signal through a coated fiber probe with the PSTM.

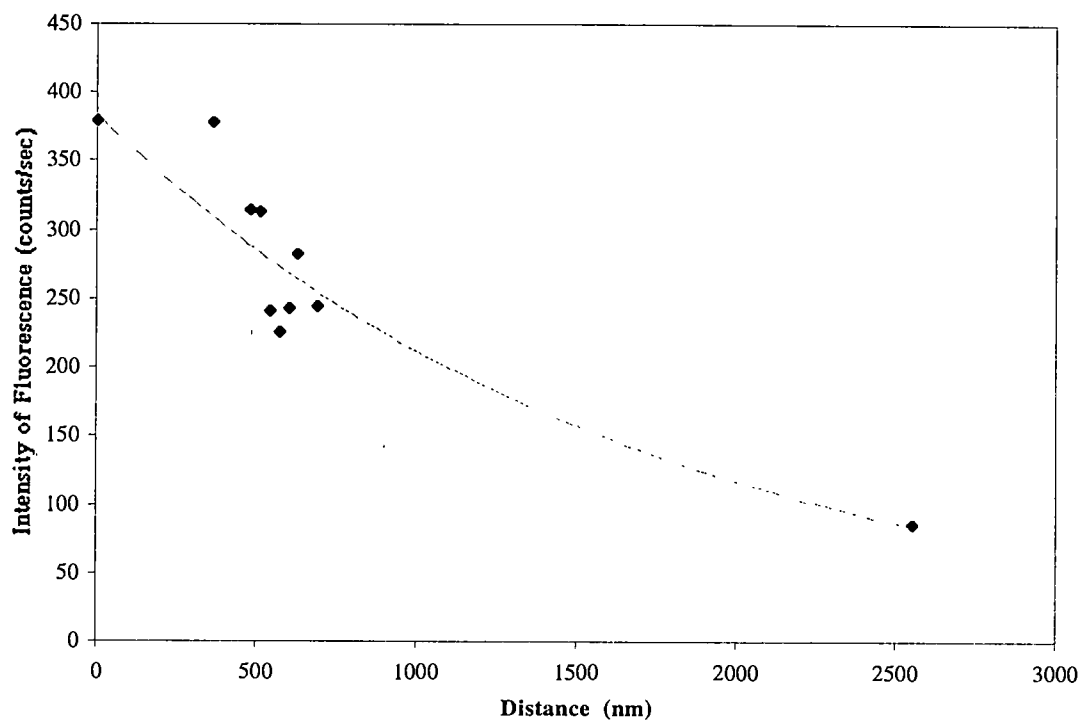


Figure 4.40: Intensity of fluorescence as a function of piezo movement. The tip is being lowered to the surface while the two-photon signal is being monitored. More signal is observed close to the surface but it is not clear if this is due to enhancement or just a closer proximity to the surface. The intensity was set near the point that two-photons would be produced and was probably a little bit above the point so seeing green signal does not have to indicate enhancement.

The following graphs present an experiment that used coated and uncoated fiber probes. The coated probes had a 60 nm layer of gold vacuum evaporated onto their surface while they were rotated. A HeNe laser was used to maintain the distance between the probe tip and the sample. The focus of the Ti:Sapphire laser was adjusted so that fluorescence could be visibly observed at 127 mW pump energy.

The results for an uncoated fiber held at a fixed position in the far field and an uncoated fiber at a fixed position in the near field are presented in Fig. 4.41. The near field was determined by observing the exponential decay of the 632.8 nm laser light. The figure indicates a definite fluorescent signal detection in both cases. The log-log of these results is shown in Fig. 4.42 and has a slope near 2.

The results of coated probes held at various distance from the surface is presented in Fig. 4.43. As the distance to the surface is reduced the observed signal intensity increases. The log-log plot of two of these curves, one from the far field and one from the near field, is presented in Fig. 4.44.

The results show the feasibility of detecting the two-photon fluorescent signal with a coated and uncoated fiber and the last results may even indicate the possibility of signal enhancement due to the metal-coated probe. The results are promising and further research should be conducted once a smoother sample can be found. A smoother sample should allow for a better more consistent sample probe separation distance. Also an absolute distance to the surface measurement would be necessary to know if the tip is close enough to the surface. Finally, an image of the yellow dye on the quartz substrate is presented in Fig.4.45.

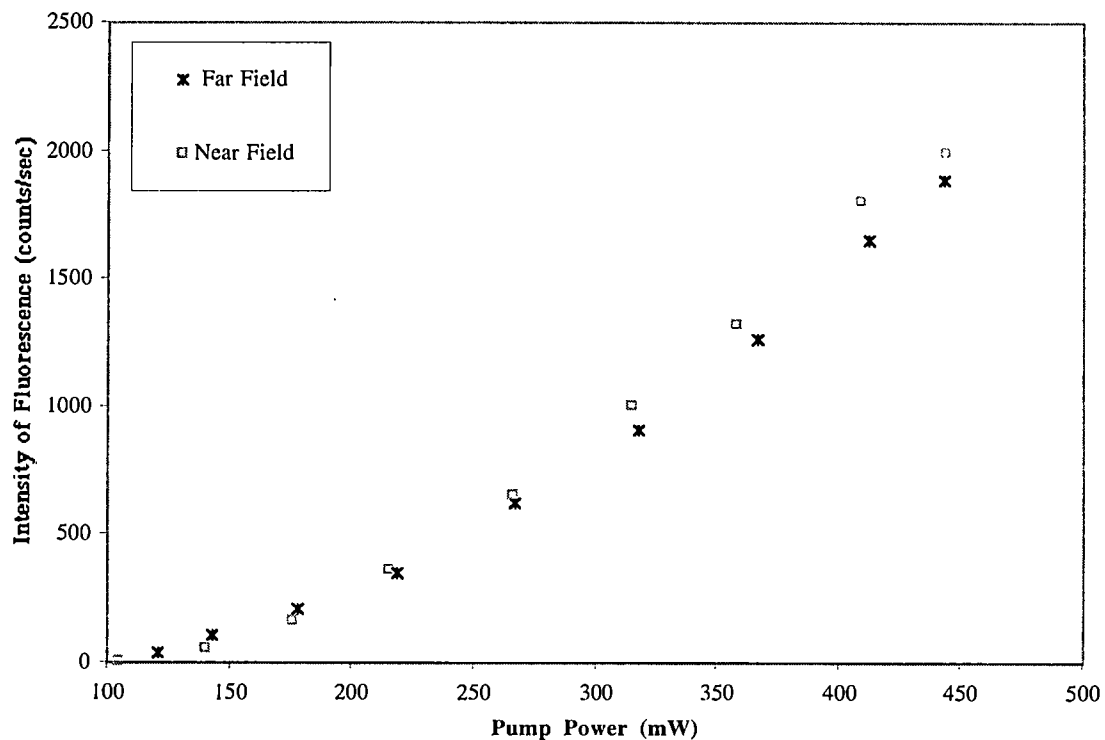


Figure 4.41: This graph shows the intensity of an uncoated fiber near and far to the surface. It plots the intensity of the frequency doubled light as a function of input intensity. The two-photon cutoff should be around 126 mW pump intensity.

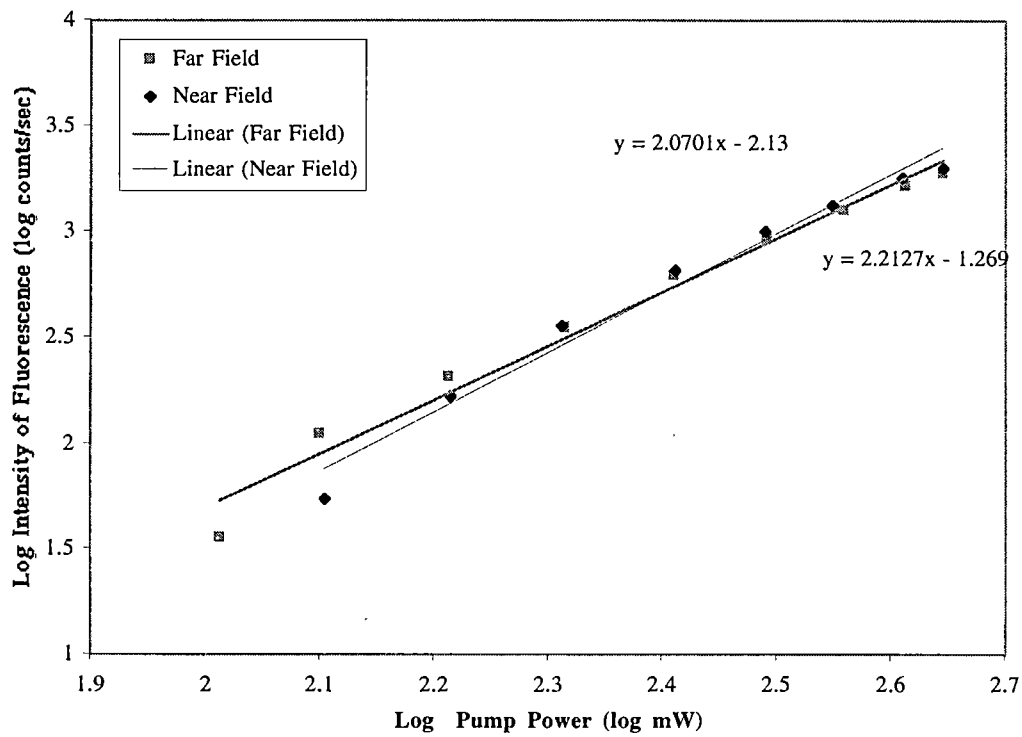


Figure 4.42: Log-Log plots of the uncoated fiber data. Both lines have slopes near 2 which is expected from two-photon processes.

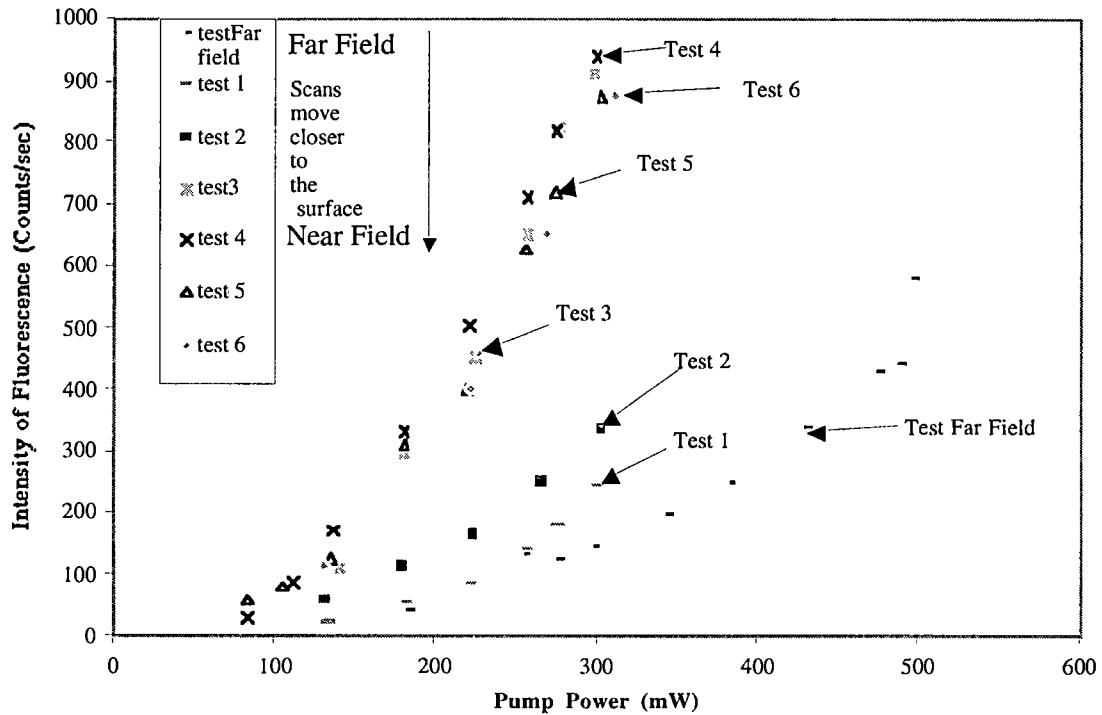


Figure 4.43: Plot of the fluorescent signal for different fixed positions above the sample surface. The cut off point for two-photon excitation should be located near 127 mW. This was set by adjusting the focusing lens.

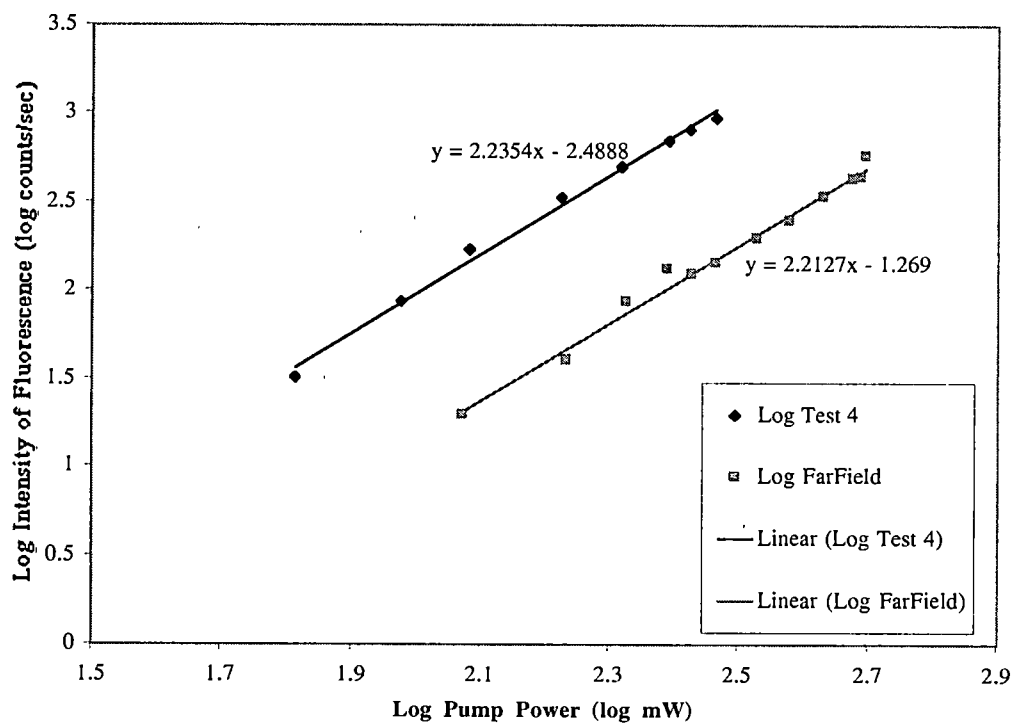


Figure 4.44: Log-Log plot of the Far field signal of a coated fiber and the near field signal. Both have similar slopes. Does the offset show enhancement or just the difference in collection efficiency between a fiber close or far from the surface.

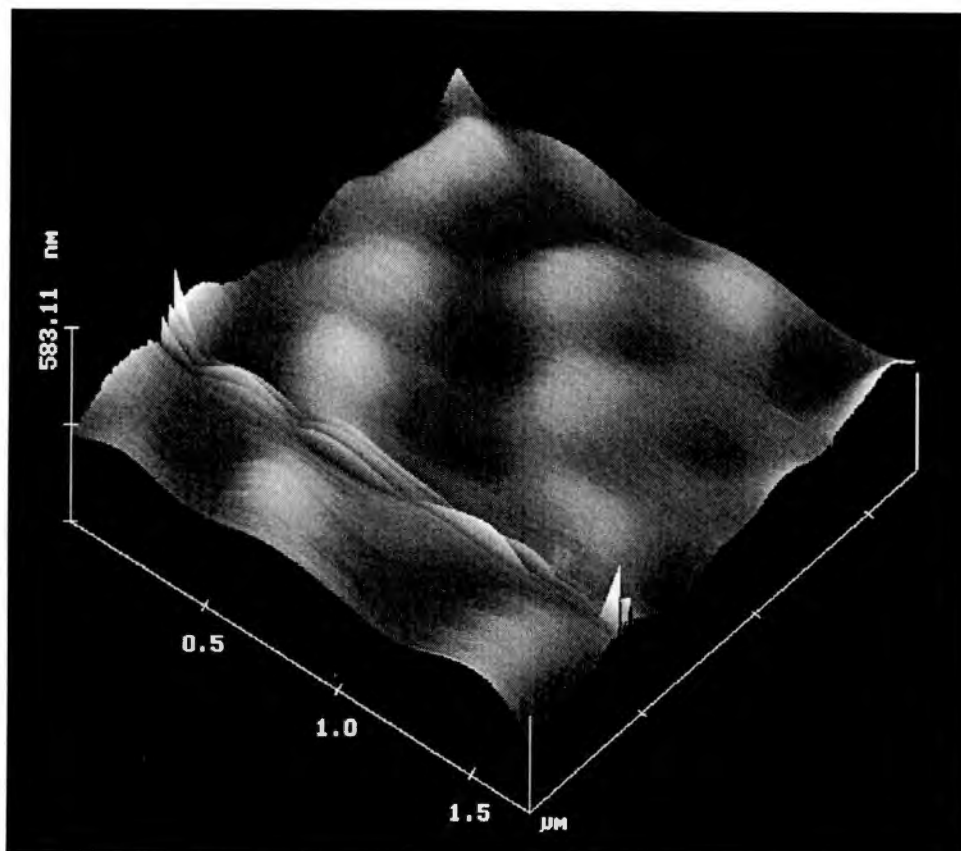


Figure 4.45: Image taken of the surface of the yellow dye with a 632.8 nm laser.

4.5 Distance to Surface

This part of the experiment involved the use of a 632.8 HeNe laser and 544 nm HeNe laser in the standard imaging setup over a clean quartz slide. A split fiber was used to deliver the measured signals to a small spectrometer and a PMT which was used with the Nanoscope IIIa[®] for imaging and sample probe separation.

The truncated cone approximation was used to develop a theory that describes the movement of the piezoelectric tube by monitoring changes in the tunneling light intensities. However, the absolute distance was not obtained because the normalization removes that information. Normalization was needed in order to adjust for the intensity fluctuations in the light sources. In the case presented the intensity measurements were normalized to their highest point to account for differences in the tunneling signal intensity. Fig. 4.46 gives the distance to the surface as calculated from the normalized data shown in Fig. 4.47

The results demonstrate the possibility of monitoring the movement of the probe with the evanescent field. The absolute distance cannot be found yet because of problems of a large difference in wavelengths. Improvement in the future will be made through the use of a better probe tip model and through the use of wavelength that are very close together.

All of the calculations were performed with the 633 and 544 HeNe lasers and the data was normalized to the highest point of the data set where this point should be very close to the surface

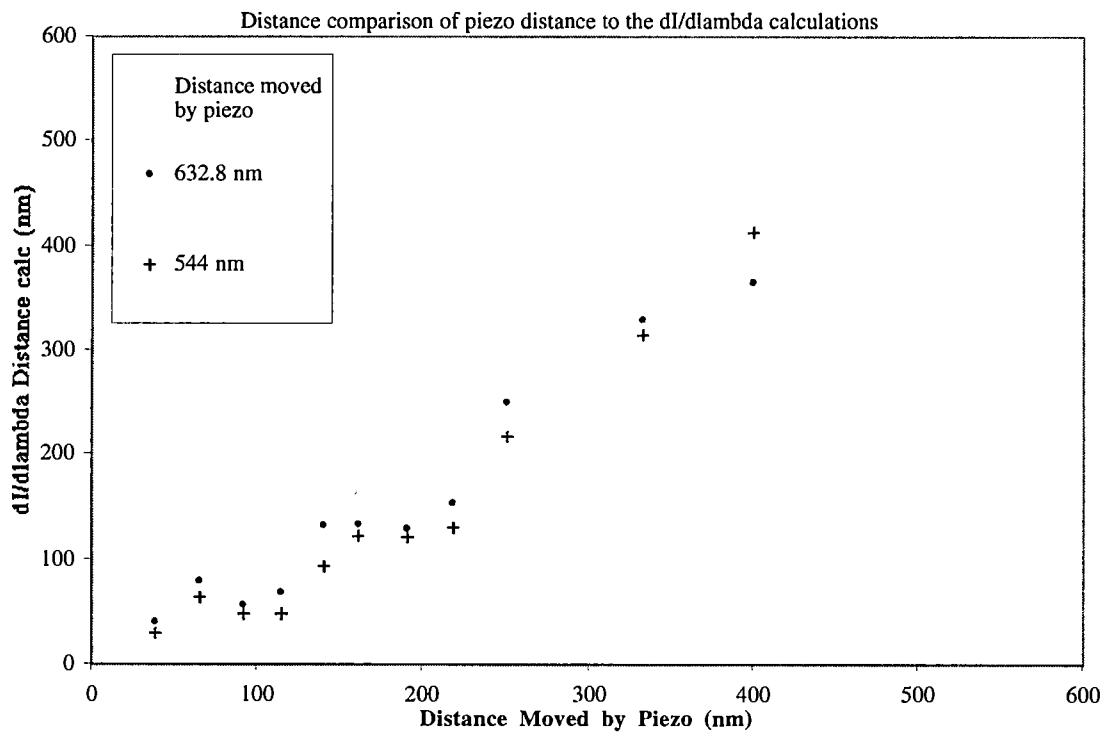


Figure 4.46: Calculated distance to the surface from the distance data set. The solid line is the distance the piezo moved.

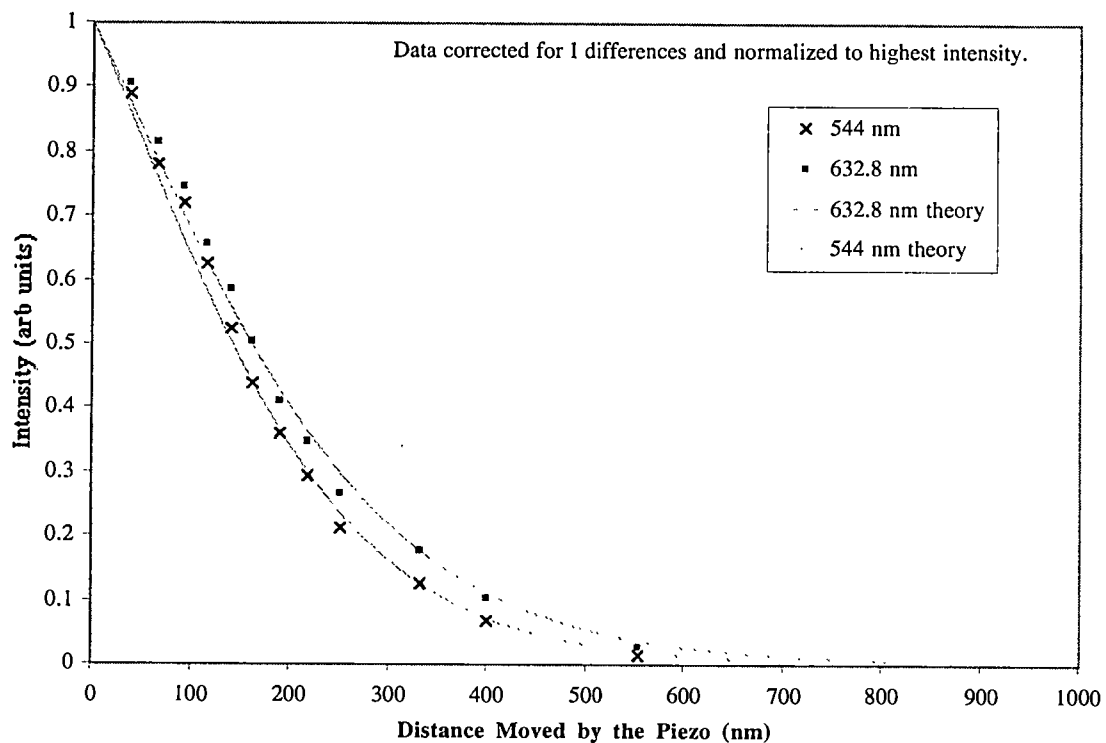


Figure 4.47: Normalized tunneling signal for the distance data set with a theoretical approximation. The theoretical approximation is based on the truncated cone model.

Chapter 5. Conclusions and Future Possibilities

5.1. Conclusions

The results presented show that it is possible to use the PSTM for absorption spectroscopy of closely spaced absorbers and for imaging. Indications that slight differences in absorption as a function of location were obtained but need verification through the use of samples with narrower absorption spectra. The capabilities of the microscope have thus been expanded to contain near-zone absorption spectroscopy. Absorption studies open up a new area of research for the PSTM by expanding the capabilities of the microscope to do spectroscopic work on small sample areas while imaging the surface. Gold Island absorption is important to different types of sensor work. As physics pushes the boundaries of nano-technology the ability to characterize localized surfaces area will play a much greater role. Refinements related to measurements of the distance to surface and changes in tip shape remain to be addressed.

Results presented show that when imaging metal particles the PSTM can function as an electromagnetic field probe to measure the superimposed evanescent and induced dipole fields. These images presented highlight the ability of the microscope to measure and map the electromagnetic topography of a sample and demonstrate resolution possibilities. The dependence of the dipole moment upon frequency determines the intensity of the dipole signal in the near-zone.

Two-photon excitation possibilities have also been demonstrated and results indicate that the PSTM is ideally suited to help in this field of study. The results show

that the detection of the two-photon fluorescence signal is possible in the PSTM with a metal-coated fiber probe. Unfortunately the results do not conclusively demonstrate tip enhancement effects but the ability to detect and monitor the excited fluorescence signal has been demonstrated.

A theory is presented and tested that allows the absolute distance to surface to be measured. Initial distance to the surface measurements are presented and demonstrate the possibility of the method but more stable light sources are needed to improve the accuracy of the measurement.

5.2. Future Possibilities

Future possibilities include the use of the PSTM to conduct absorption and fluorescent spectroscopy on many different samples. A configuration is needed for the PSTM that includes a spectrometer combined with electronics and processing that would allow for imaging to be conducted over a selectable area of the spectrum. In this manner the signal intensity could be increased because the split fiber setup used in this experiment could be replaced with a single fiber. This setup would provide the ability to check the whole spectrum and feedback on a selectable area of the signal while operating the microscope.

Improved lights sources and signal strength measurements would be useful in obtaining intensity changes in white light signals. This would be aided by a more precise ability to determine the distance of the probe to the surface.

Polarization variations and changes in the angle of incidence of the light would also be interesting to observe. Polarization microscopy is well known and there are polarization preserving optical fibers that are suitable.

5.3. Discussion of Technologies

The solutions to the difficulties presented above and available or expected in the future can be addressed based on the results. The intensity and the stability of the signal can be increased by a new configuration. If a hemispherical lens is used in lieu of the plano-convex cylindrical lens, it is possible to use a large number of sources placed circumferentially and aligned by an annular ring mount. If the intensity fluctuations are random, then the use of N sources reduces the fluctuations by a factor of the square root of N . An arrangement of 64 quartz-halogen sources would thus not only produce 64 times greater intensity, but would also produce a signal that is eight times more stable than a single source. The spectroscopic capabilities would be thus improved. As sources are reduced in size and increased in efficiency it may be possible to utilize even larger numbers. In an annular ring of radius 20 cm the circumference is 125.6 cm and 251 sources separated by 0.5 cm could be reasonably mounted resulting in almost a factor of 16 reduction in intensity fluctuations. This configuration also presents a nearly isotropic input. The lowering cost of diode lasers and the development of fluorophores with greatly increased two-photon cross sections may soon permit second-harmonic generation with a considerable improvement in economy relative to high-power lasers.

Works Consulted

Reference

1. From the history of the light microscope written by thjones@utmml.utm.edu
2. *Encyclopedia Britannica*, Micropaedia Vol. VI (Encyclopaedia Britannica, Inc. 1981), p. 120.
1. "Ernst Abbe (1840-1905) discovered that the minimum transverse distance between two object points that can be resolved in the image varies directly as λ and inversely as the Numeric Aperture of the lens." E. Hecht, *Optics 2nd Ed.* (Addison-Wesley, California, 1987) p. 192
4. E. Hecht, *Optics 2nd Ed.* (Addison-Wesley, California, 1987) p. 422
5. W.H. Denk, J.H. Strickler, and W.W. Webb, "2-Photon Laser Scanning Fluorescence Microscopy" *Science*, **248**, 73-76 (1990)
6. J.B. Shear, "Multiphoton-Excited Fluorescence" *Analytical Chemistry News & Features*, 598A-605A, (1999)
7. G. Binning, H. Rohrer, "Scanning Tunneling Microscopy", *Helv. Phys. Acta.*, **55**, 726-735 (1982)
8. E. H. Synge, *Phil. Mag.* **6**, 356 (1928)
9. E. A. Ash, G. Nicholls, "Super resolution aperture scanning microscope.", *Nature* **237**, 510-513 (1972)
10. D. W. Pohl, W. Denk, and M Lanz, *Appl. Phys. Lett.* **44**, 651 (1984)
11. E. Betzig, P.L. Finn, and J.S. Weiner, *Appl. Phys. Lett.* **60**, 2484 (1992)
12. R. C. Reddick, R. J. Warmack, T. L. Ferrell, US Patent 5018865 (Nov. 1986)
13. R. C. Reddick, R. J. Warmack, and T. L. Ferrell, "A new form of scanning optical Microscopy.", *Phys Rev B* **39**, 767-770 (1989)
14. I. Newton, *Opticks* (Dover, New York, 1952)
15. P. J. Leqrgans, A. F. Turner, *J. Opt. Soc. Am.*, **37**, 983(A) (1947), S Zhu, A.W. Yu, D Hawley, R Roy "Frustrated total internal reflection: A demonstration and review." *Am. J. Phys.* **54**(7), (1986)

16. T. L. Ferrell, S. L. Sharp, and R. J. Warmack, "Progress in Photon Scanning-Tunneling Microscopy (PSTM)", *Ultramicroscopy* **42-44**, 408-415 (1992)
17. M. A. Paesler, P. J. Moyer, C. J. Jahncke, C. E. Johnson, R. C. Reddick, R. J. Warmack, and T. L. Ferrell, "Analytical Photon Scanning Tunneling Microscopy", *Phys. Rev. B* **42**(10), 6750-53 (1990)
18. K. Estermann, *Z. Phys. Chem.*, **106**, 403 (1923)
19. K. Estermann, *Z. Phys. Chem*, **33**, 320 (1925)
20. S.W. Kennerly, R.J. Warmack, T.L. Ferrell, "The scattering and absorption of light due to surface resonances on submicron oblate spheroidal particulates.", ORNL internal report
21. J.S. Fritz, G.H. Schenk, *Quantitative Analytical Chemistry 5th ed.* (Allyn and Bacon, Inc. Newton Massachusetts. 1987) p 379
22. T. L. Ferrell, "Surface enhanced raman scattering in Ag-Pyridine Sols", *Phys Rev B* **25**, 2930-32 (1982)
23. J.P. Goudonnet, T. Inagaki, E.T. Arakawa, and T.L. Ferrell, "Angular and Polarization Dependence of Surface-Enhanced Raman Scattering in Attenuated-Total-Reflection Geometry" *Phys Rev B* **36**, 917-21 (1987)
24. J. P. Goudonnet, T. Inagaki, T. L. Ferrel, R.J. Warmack, M.C. Buncick, and E.T. Arakawa, "Enhanced Raman Scattering from Benzoic Acid on Silver and Gold Prolate Spheroids on Large and Transparent Patterned Areas", *Chem. Phys.* **106**, 225-32 (1986)
25. T. L. Ferrell, "New Concepts in Surface-Enhanced Raman Scattering (SERS)", Proceedings of the 1986 US Army Chemical Research, Development, and Engineering Center Scientific Conference on Chemical Defense Research, CRDEC-SP-87008, 363-66 (1987),
26. J. P. Goudonnet, J. L. Bijeon, R. J. Warmack, and T. L. Ferrell "Substrate Effects on the Surface-Enhanced Raman Spectrum of Benzoic Acid Adsorbed on Silver Oblate Microparticles." *Phys Rev B* **43**(6), 4605-12 (1991)
27. E. J. Sanchez, "Near Field Fluorescence Microscopy Based on Two-Photon Excitation with Metal Tips" *Phys. Rev. Lett.* **82**(20) 4014-4017 (1999)

28. H. Wetzel, H. Gerischer, B. Pettinger, "Surface-Enhanced Raman-Scattering from Silver-Cyanide and Silver-Thiocyanate Vibrations and the importance of ADatoms." *Chem. Phys. Lett.* **80**(1) 159-162 (1981)
29. S. L. Sharp, R. J. Warmack, J. P. Goudonnet, I. Lee, and T. L. Ferrell, "Spectroscopy and Imaging Using the Photon Scanning-Tunneling Microscope", *Acc. Chem. Res.* , **26**, 377-382 (1993)
30. D. Kleinfeld, P.P. Mitra, F. Helmchen, W. Denk, *Proc. Natl. Acad. Sci U.S.A.*, **95**, 15741-46 (1998)
31. $\vec{S} = \frac{1}{\mu_0} \vec{E} \times \vec{B}$ "The magnitude of S is the power per unit area crossing a surface whose normal is parallel to S. The formula was named after John Henry Poynting (1852-1914)" E. Hecht, *Optics 2nd Ed.* (Addison-Wesley, California, 1987), p. 43
32. Willebrord Snell (1591-1616) discovered the law of refraction in 1621. The familiar sine formulation, given here, was first published by René Descartes (1596-1650), E. Hecht, *Optics 2nd Ed.* (Addison-Wesley, California, 1987), p. 3
33. J.D. Jackson, *Classical Electrodynamics 2nd Ed.*, New York; John Wiley & Sons, Inc., (1975)
34. J.D. Jackson, *Classical Electrodynamics 2nd Ed.*, New York; John Wiley & Sons, Inc., (1975)
35. O. Heavens, *Optical Properties of thin Solid Films* (Dover, New York, 1965)
36. P. Royer, J. P. Goudonnet, R. J. Warmack, T. L. Ferrell, "Substrate effects on surface-plasmon spectra in metal-island films.", *Phys. Rev. B* **35**(8), 3753-3759 (1987)
37. R. J. Warmack, S. L. Humphrey, "Observation of two surface-plasmon modes on gold particles.", *Phys. Rev. B* **34**(4), 2246-2252 (1986)
38. J. P. Goudonnet, T. Inagaki, E. T. Arakawa, T. L. Ferrell, "Angular and polarization dependence of surface-enhanced Raman scattering in attenuated-total-reflection geometry.", *Phys. Rev. B* **36**(2), 917-921 (1987)
39. S. W. Kennerly, J. W. Little, R. J. Warmack, T.L. Ferrell, "Optical Properties of heated Ag films.", *Phys. Rev. B* **29**(6), 2926 (1984),
40. , J.H. Weaver, C. Krafka, D.W. Lynch, E.E. Koch, *Physics Data, Optical Properties of Metals* (Fachinformationzentrum, Germany, 1981)

41. E. Palik, *Handbook of Optical Constants of Solids*, Academic Press Handbook Series, (Harcourt Brace Jovanovich, Publishers New York, 1985)
42. Mathcad® Plus 6 for Macintosh by Mathsoft® of Cambridge Massachusetts
43. T. Downey, *Gold-Island Thin Film Surface Plasmon Excitation on an Optical Fiber*, Master Thesis at The University of Tennessee, Knoxville (1998)
44. P. Royer, J. P. Goudonnet, R. J. Warmack, and T. L. Ferrell, *Physical Review B*, **35**, 8 (1987) pg.3754)
45. G.L. Richmond, J.M. Robinson, V.L. Shannon, Second Harmonic Generation Studies of Interfacial Structure and Dynamics, *Progress in Surface Science*, **28**(1) pp. 1-70, (1988)
46. E Wachter Personal Correspondence
47. E. Hecht, *Optics 2nd Ed.* (Addison-Wesley, California, 1987)p. 612
48. R. C. Reddik, *Photon Scanning Tunneling Microscopy*, Doctoral Dissertation at The University of Tennessee, Knoxville (1990)
49. <http://www.physikinstrumente.com/tutorial/index.html>, Physik Instrumente
50. C. Julian Chen, *Introduction to Scanning Tunneling Microscopy*, (Oxford University Press, New York, 1993) p. 213
51. G. Binnig, H. Rohrer, *Rev. Mod. Phys.* **56**, 615 (1987)
52. *System manual for the detector controller*, Princeton Instruments Inc., Trenton NJ, p. 2
53. Thorlabs Inc., Newton, NJ
54. *CP-200 Technical Manual*, ISA Jobin Yvon® Longjumeau Cedex, France (1989) p. 18
55. *HR-640 Operators Manual*, ISA Instruments SA, Inc., Longjumeau Cedex, France, p. 3
56. F. Meriaudeau, J. P. Goudonnet, E. Carver, J. Parks Jr., K. B. Jacobson, R. J. Warmack, and Thomas L. Ferrell, "Photon Scanning-Tunneling Microscopy of Unstained Mammalian Cells and Chromosomes", *Appl. Opt.*, **37**(31), 7276-7288 (1998)

Bibliography

PSTM

1. F. Meriaudeau, J. P. Goudonnet, E. Carver, J. Parks Jr., K. B. Jacobson, R. J. Warmack, and Thomas L. Ferrell, "Photon Scanning-Tunneling Microscopy of Unstained Mammalian Cells and Chromosomes", *Appl. Opt.*, **37**(31), 7276-7288 (1998)
2. J. P. Goudonnet, E. Bourillot, P.M. Adam, F. de Fournel, L. Salomon, P. Vincent, M. Nevier, and T.L. Ferrell, "Imaging of Calibrated Quartz Gratings with a Photon Scanning Tunneling Microscope: Experiment and Theory", Abstract, *Journal of the Optical Society of America A: Optics, Image Science, and Vision* **12** (8), 1749-1764 (1995)
3. T. L. Ferrell, "Modulation of Collective Electronic Effects in Foils by the Electron Scanning Tunneling Microscope", *Nucl. Instrum. Methods B* **96**, 483-85 (1995)
4. I. Lee, R. J. Warmack, and T. L. Ferrell, "Laser Lithography by Photon Scanning Tunneling Microscopy", *Proc. Second International Conference on Laser Ablation*, J. C. Miller and D. B. Geohegan, Editors, AIP Press, 544 (1994)
5. S. L. Sharp, R. J. Warmack, J. P. Goudonnet, I. Lee, and T. L. Ferrell, "Spectroscopy and Imaging Using the Photon Scanning-Tunneling Microscope", *Acc. Chem. Res.* , **26**, 377-382 (1993)
6. J. Cites, M.F.M. Sanghadasa, C. C. Sung, R. C. Reddick, R. J. Warmack, and T. L. Ferrell, "Analysis of Photon Scanning Tunneling Microscope Images", *J. App. Phys.* **71**, 7-10 (1992)
7. T. L. Ferrell, S. L. Sharp, and R. J. Warmack, "Progress in Photon Scanning-Tunneling Microscopy (PSTM)", *Ultramicroscopy* **42-44**, 408-415 (1992)
8. J. P. Goudonnet, and T. L. Ferrell, "La Microscopie à Effet Tunnel Photonique", *Spectra 2000* **155**, 39-42 (1991)
9. T. L. Ferrell, J. P. Goudonnet, R. C. Reddick, S. H. Sharp, and R. J. Warmack, "The Photon Scanning Tunneling Microscope", *J. Vac. Sci. Technol. B* **9**(2), 525-530 (1991)
10. M. A. Paesler, P. J. Moyer, C. J. Jahncke, C. E. Johnson, R. C. Reddick, R. J. Warmack, and T. L. Ferrell, "Analytical Photon Scanning Tunneling Microscopy", *Phys. Rev. B* **42**(10), 6750-53 (1990)

11. R. C. Reddick, R. J. Warmack, D. W. Chilcott, S. L. Sharp, and T. L. Ferrell, "Photon Scanning Tunneling Microscopy", *Rev. Sci. Instrum.* **61**(12), 3669-3677 (1990)
12. R. C. Reddick, R. J. Warmack, and T. L. Ferrell, "New form of scanning optical microscopy", *Phys. Rev. B* **39**(1), 767-770 (1989)
13. R. C. Reddick, R. J. Warmack, T. L. Ferrell, *Phys. Rev. B* **39** (1989) 767-770 and US Patent 5018865 (Nov. 1986)
14. P.J. Moyer, C.L. Jahncke, M.A. Paesler, R.C. Reddick, R.J. Warmack, "Spectroscopy in the evanescent field with an analytical photon scanning tunneling microscope.", *Phys. Lett. A* **145**(6,7), 343-347 (1990)
15. J.R. Krenn, W. Gotschy, D. Somitsch, A. Leitner, F. R. Aussenegg, "Investigation of localized surface plasmons with the photon scanning tunneling microscope." *Appl. Phys. A* **61**, 541-545(1995)

Gold Islands

16. P. Royer, J.P. Goudonnet, R.J. Warmack, T. L. Ferrell, "Substrate effects on surface-plasmon spectra in metal-island films.", *Phys. Rev. B* **35**(8), 3753-3759 (1987)
17. R.J. Warmack, S.L. Humphrey, "Observation of two surface-plasmon modes on gold particles.", *Phys. Rev. B* **34**(4), 2246-2252 (1986)
18. J.P. Goudonnet, T. Inagaki, E.T. Arakawa, T.L. Ferrell, "Angular and polarization dependence of surface-enhanced Raman scattering in attenuated-total-reflection geometry.", *Phys. Rev. B* **36**(2), 917-921 (1987)
19. S.W. Kennerly, R.J. Warmack, T.L. Ferrell, "The scattering and absorption of light due to surface resonances on submicron oblate spheroidal particulates.", ORNL internal report
20. S.W. Kennerly, J.W. Little, R.J. Warmack, T.L. Ferrell, "Optical Properties of heated Ag films.", *Phys Rev. B* **29**(6), 2926 (1984)
21. K.Estermann, *Z. Phys. Chem.*, **106**, 403 (1923); *Z Phys.* **33**, 320 (1925); see also, O heavens, *Optical Properties of thin Solid Films* (Dover, New York, 1965)

Tip Enhancement

22. W. Denk, D. W. Pohl, "Near-field optics:Microscopy with nanometer-size fields.", J.Vac. Sci Technol. B **9**(2),510-513 Mar/Apr (1991)
23. L. Novotny, R.X. Bian, X. S. Xie, "Theory of Nanometric Optical Tweezers", Phys Rev Lett, **70**(4), 645-648 (1997)
24. B. G. Levi, "Progress made in Near-Field imaging with light from a sharp tip", Physics Today , p18-20 (July 1999)

Other

25. "spec in evanescent field", Phys. Lett. A **145**, 6-7, (1990)
26. R. Toledo-Crow, P. Yang, Y. Chen, and M. Vaez-Iravani, Appl. Phys. Lett. **60**, 2957 (1992)
27. K. Karrai and R.D. Grober, Appl. Phys. Lett. **66** (14), 1842 (1995)

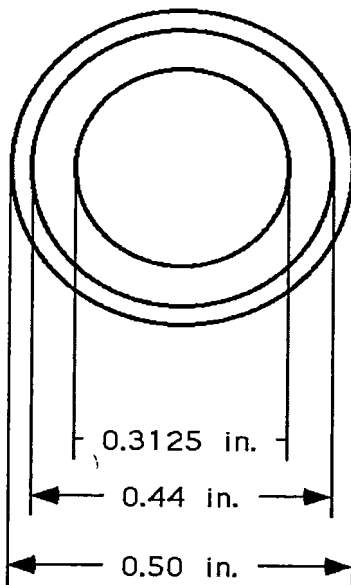
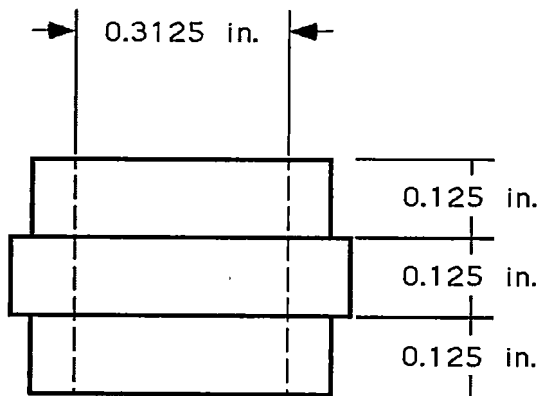
Appendices

Appendix: A. Components of the Piezoelectric Scanning Tube

Center Connector

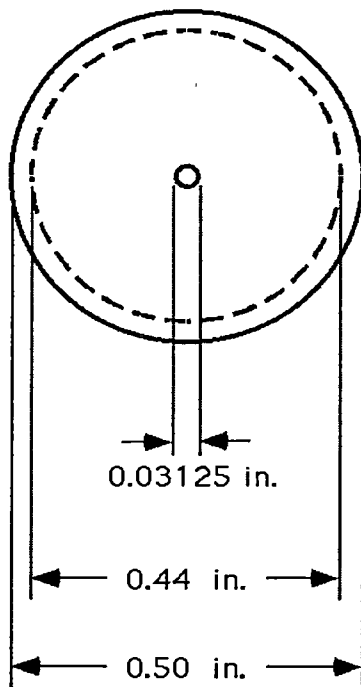
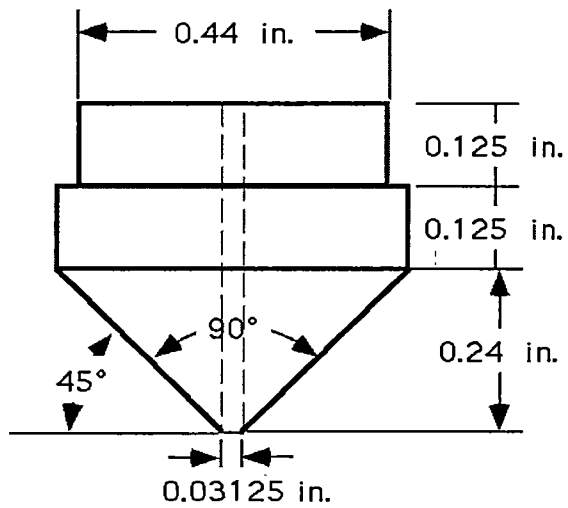
Scale 4:1

Material is Macor.



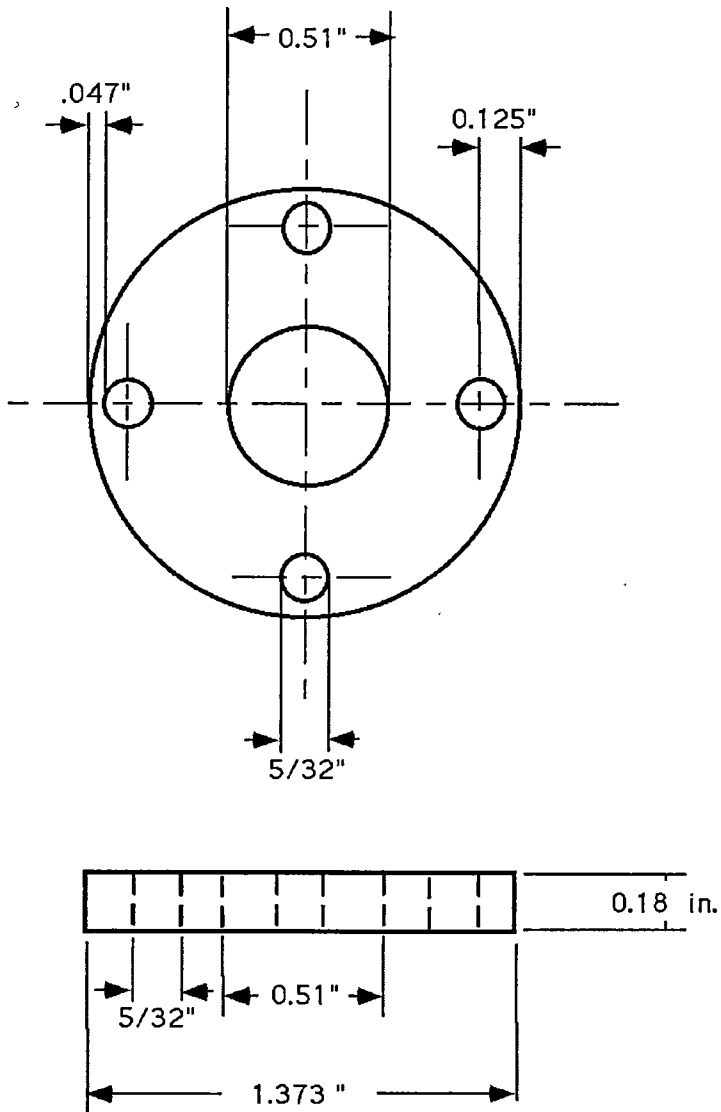
Photometrics Group
Oak Ridge National Laboratory

Nose Cone
Scale 4:1
Material is Macor



Photometrics Group
Oak Ridge National Laboratory

Ring Holder
Scale 2:1
Material is Macor.



Photometrics Group
Oak Ridge National Laboratory

Appendix: B. Mechanical structures

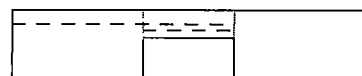
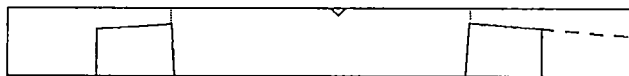
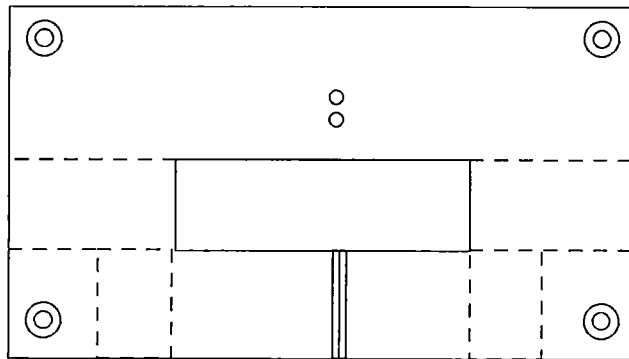
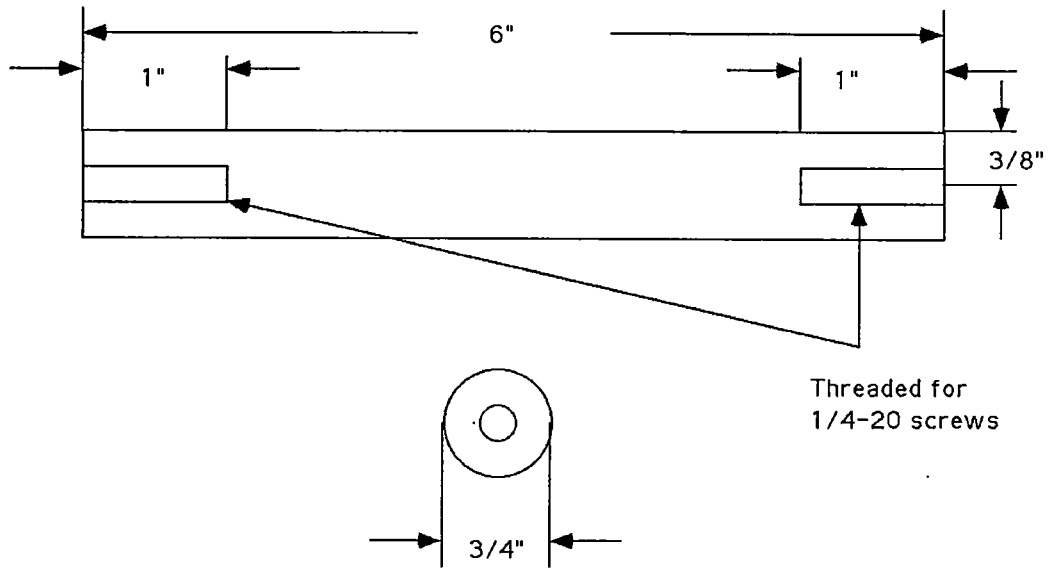


Diagram of the base.

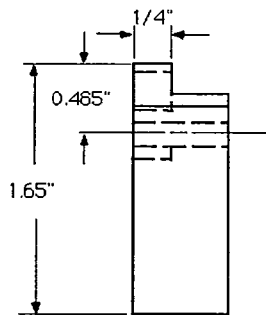
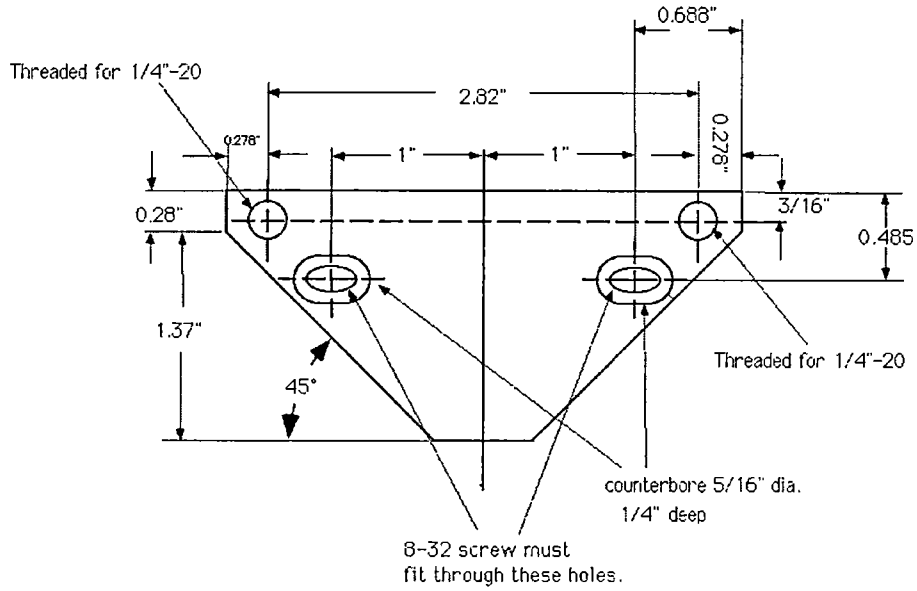
Support Rod

Need 8 of these rods.



Photometrics Group
Oak Ridge National Laboratory

Spacer



Photometrics Group
Oak Ridge National Laboratory

Appendix: C. Scattering of TIR light experiment

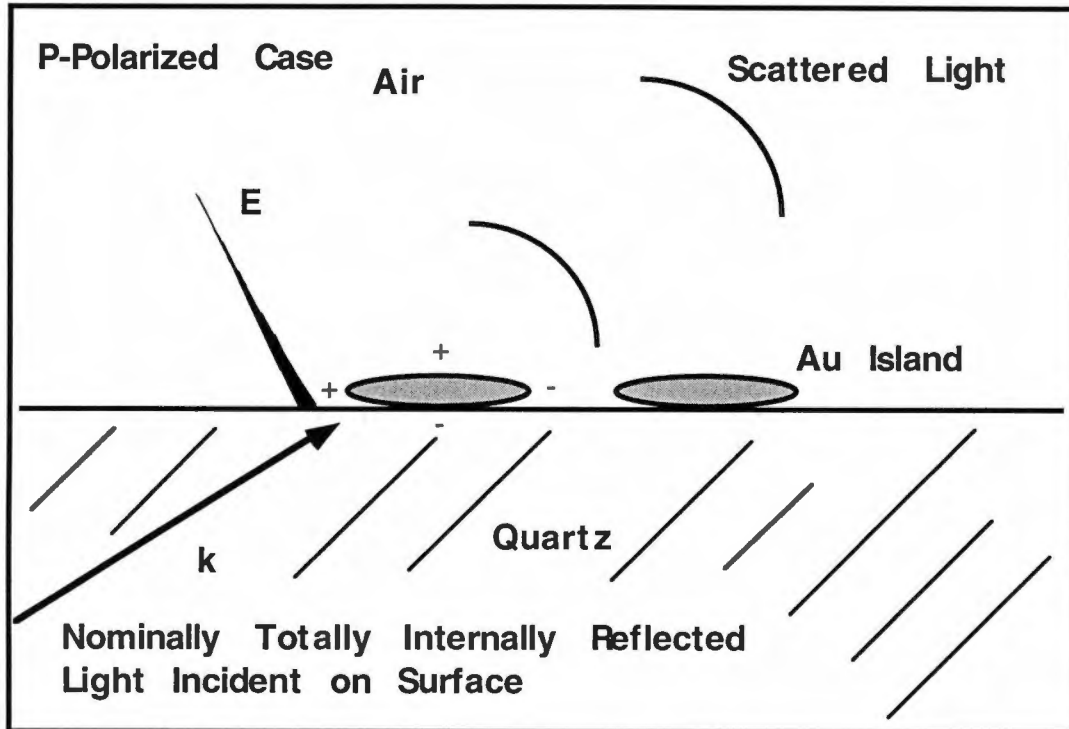
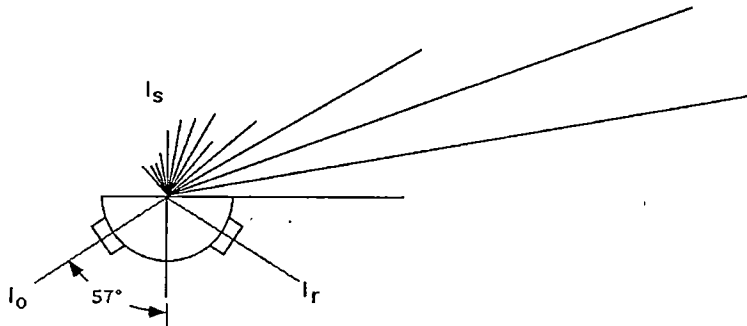


Figure XYZ. Sketch of the Case of P-Polarized Light Incident Under TIR Conditions Upon a Gold-Island Film Residing Upon the TIR Surface (Quartz). The diminishing strength of the electric field vector is indicated by the decreasing thickness shown, but not quantitatively so. The field diminishes exponentially to negligible value within one wavelength of the surface. The particles of the gold-island film are known from modeling of optical absorption data to act approximately as independent oblate spheroids. The polarizability being different along the two axes of the spheroids, the scattered light does not predominantly travel in the direction of the incident light, but the effect is not large. The case of p-polarized light gives considerably less scattering normal to the surface than does the case of s-polarized light.

Scattering on Quartz



Scattered light signal for S polarization. 544nm He Ne laser.

$$I_0 = 0.47 \text{ mW}$$

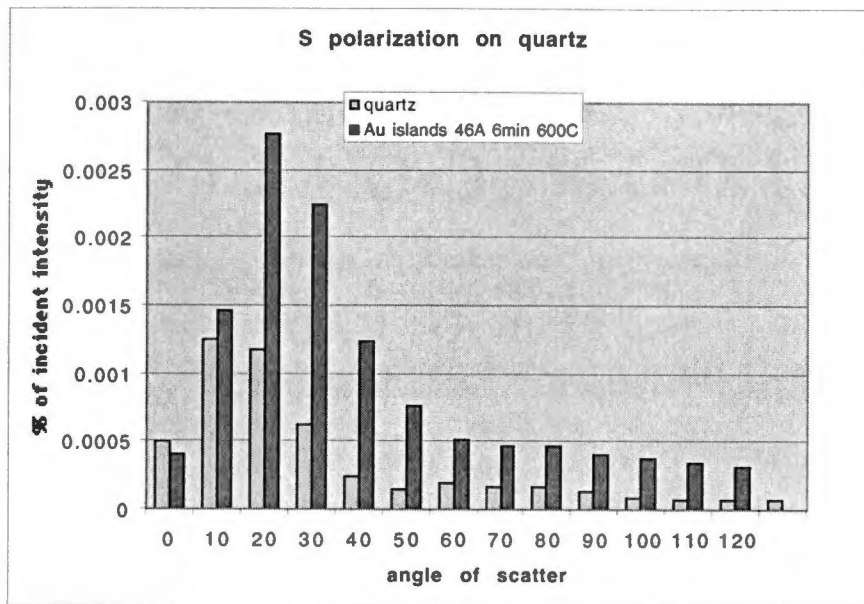
$$I_r = 0.40 \text{ mW}$$

$$I_s = 5.3 \text{ nW for the longest line and } 0.36 \text{ nW for the shortest.}$$

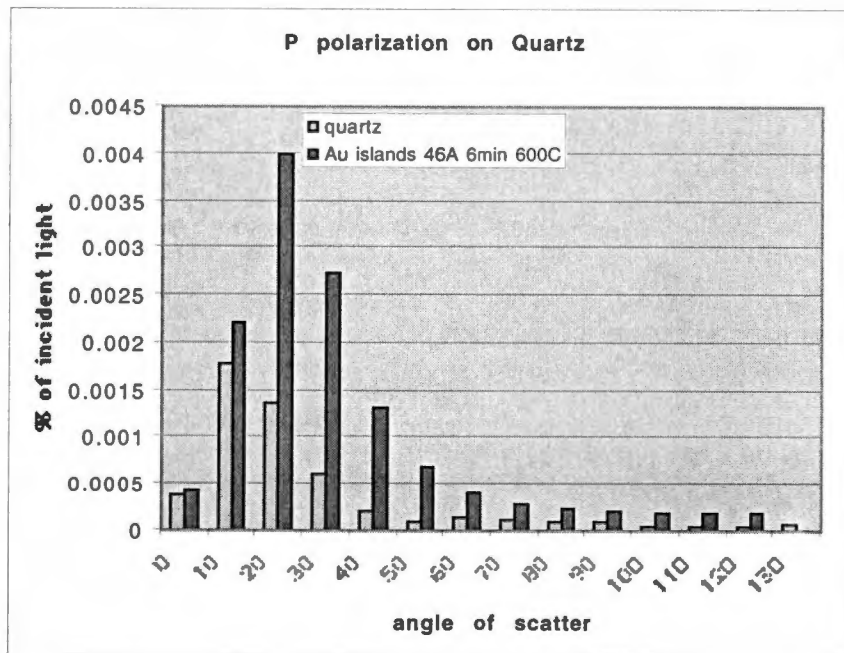
Each line of the scattered signal is proportional to the signal strength in that direction.

Scattered light was measured in 10° increments with a 0.8" lens 3.5" from the scattering center.

Scattered light signal for s-polarization of 544 nm light incident at an angle of 57° onto a quartz air interface. The largest scattering signal is in the 20° direction and is equal to 5.3 nW.

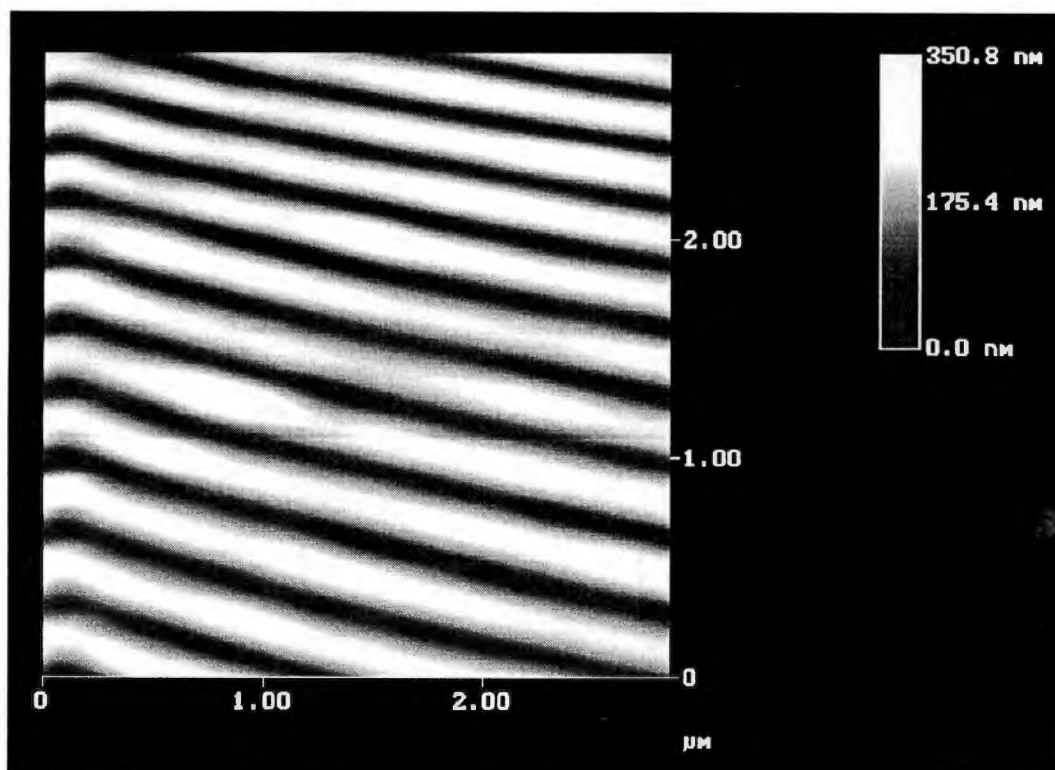


A comparison of the percent of scattered light, as a function of the s-polarized incident intensity, for a given angle for a clean quartz surface and a quartz surface with a metal island film.

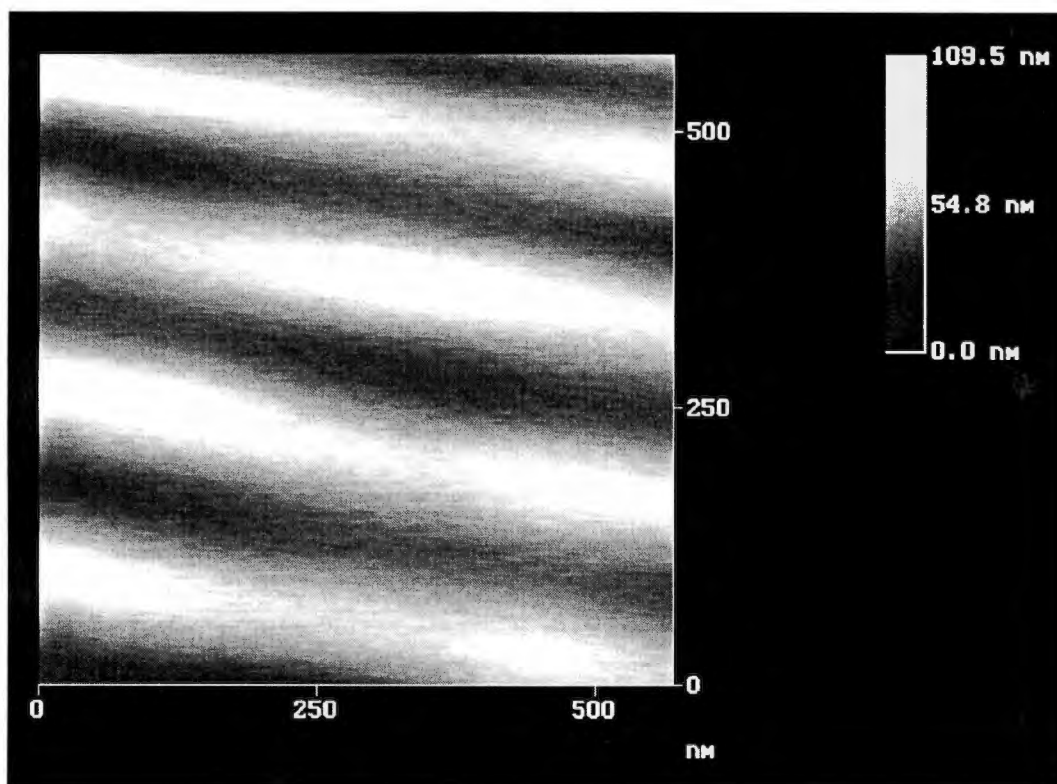


A comparison of the percent of scattered light, as a function of the p-polarized incident intensity, for a given angle for a clean quartz surface and a quartz surface with a metal island film.

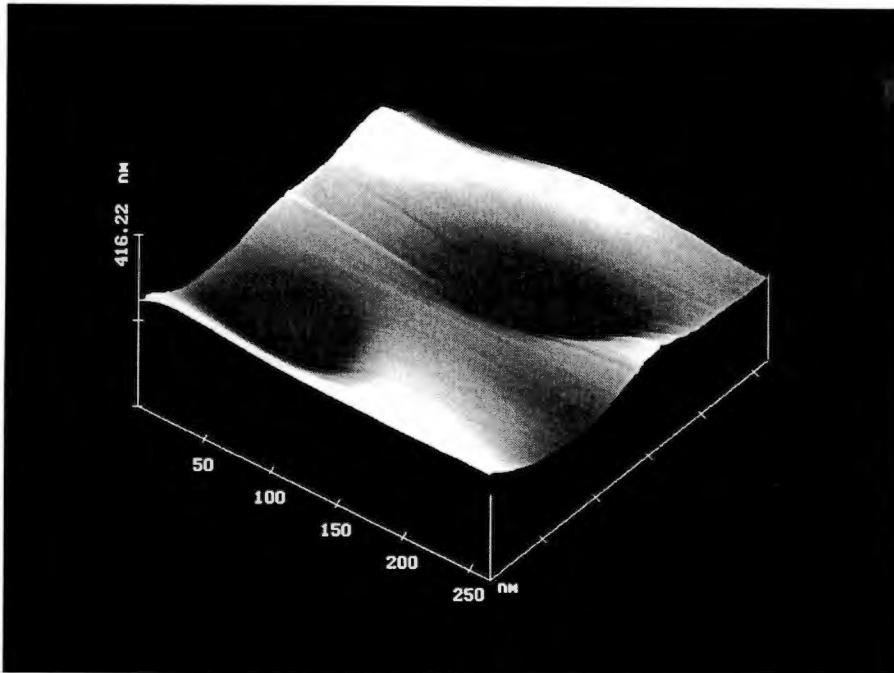
Appendix: D. Images obtained with the PSTM



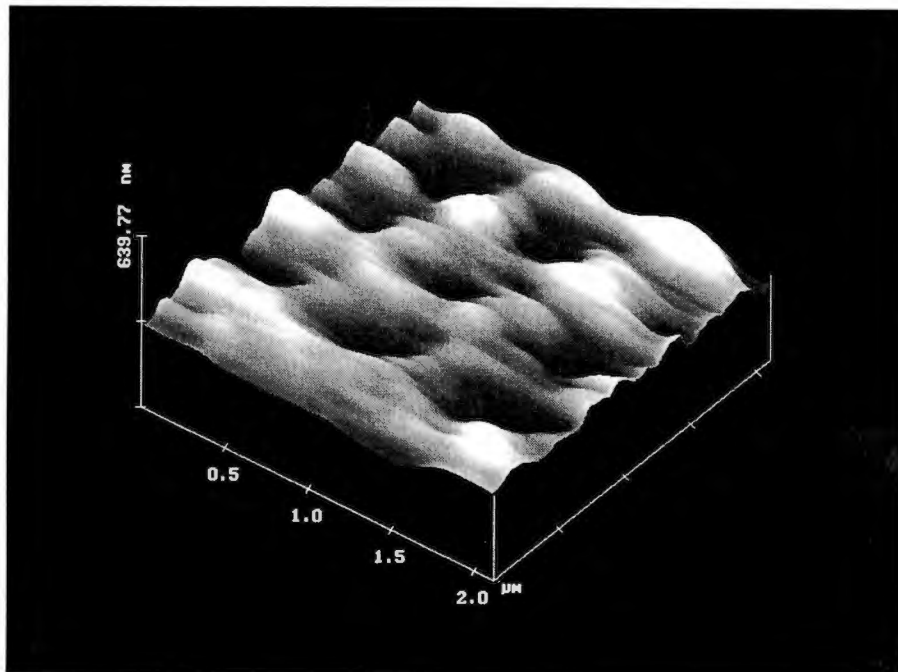
Interference pattern of a 440 nm He Cd laser incident at 44° degrees. Line spacing is 208 nm.



Interference pattern of a 632 nm He Ne laser incident at 44° . Line spacing is 300 nm.

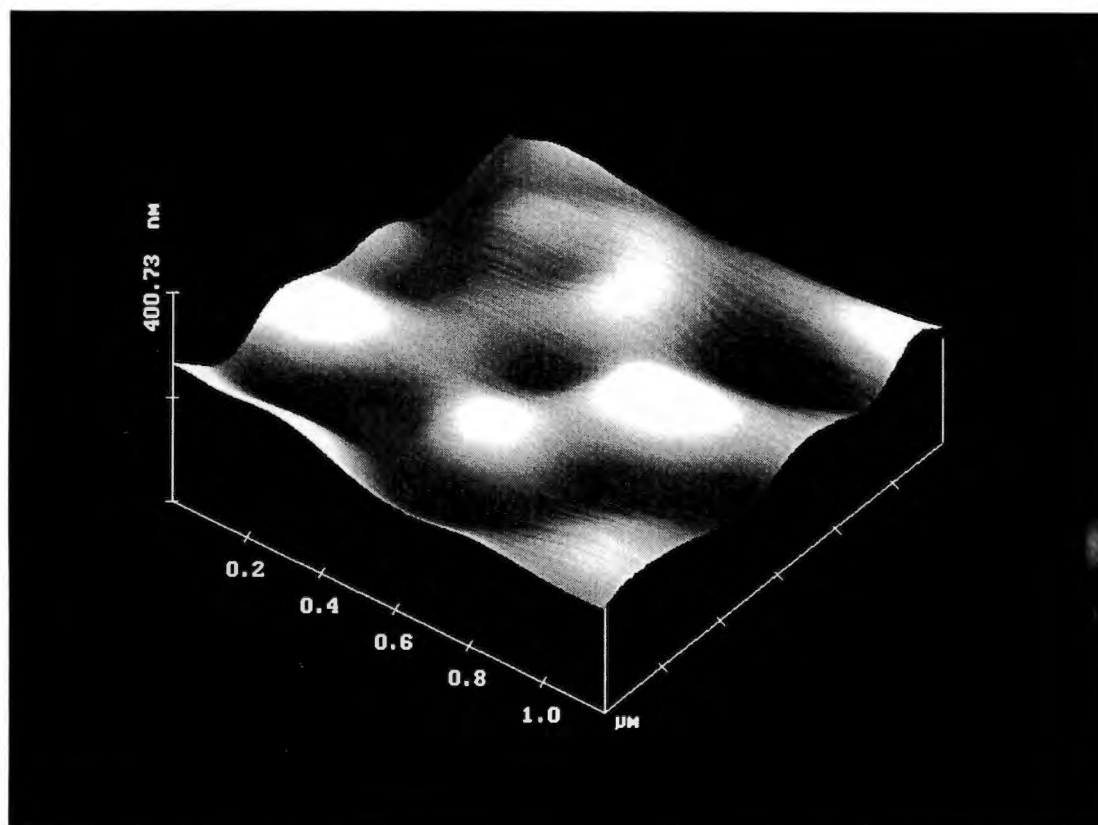


Nucleopore filter with 100 nm holes. Imaged with a 440 nm laser.

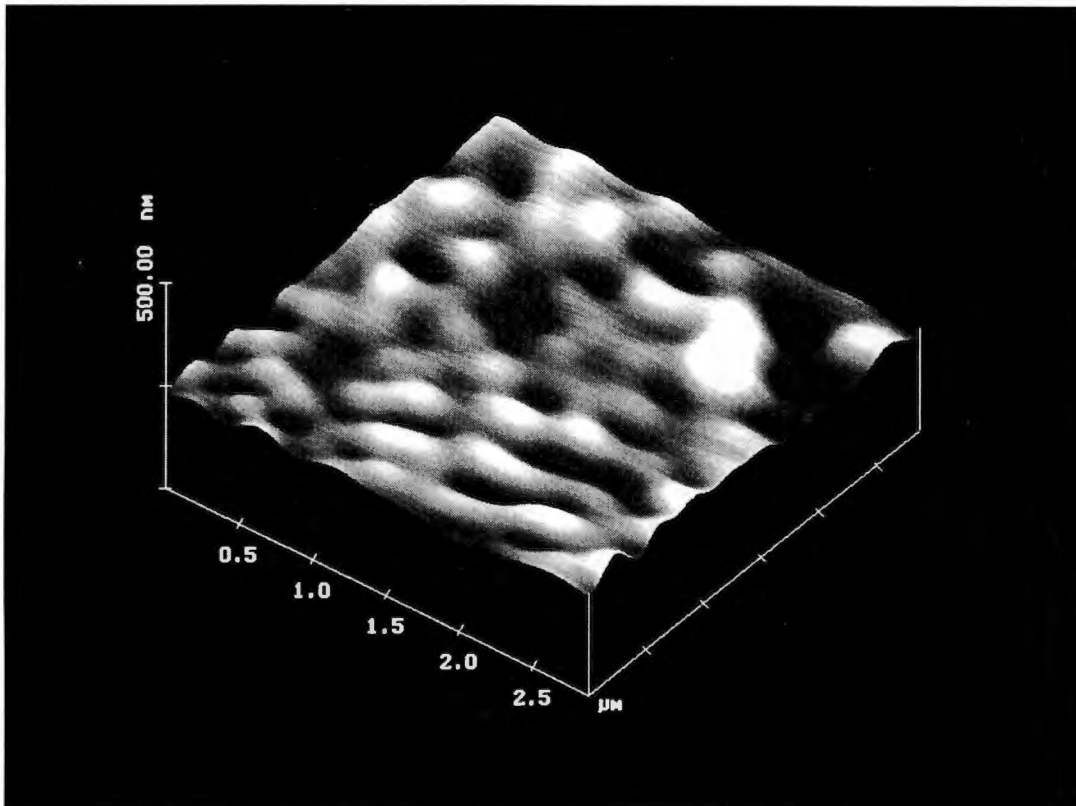


Crossed grating.

Appendix: E. Images of Gold Islands using plasmon field.



632.8 nm light is incident at 46 degrees (Plasmon angle) onto a quartz slide coated with 430 angstroms of gold-140 angstroms of SiO₂-47 angstroms of gold. The sample was heat treated at 550° C for 5 minutes.



632.8 nm light is incident at 46 degrees (Plasmon angle) onto a quartz slide coated with 430 angstroms of gold-140 angstroms of SiO₂-47 angstroms of gold. The sample was heat treated at 550° C for 5 minutes.

Vita

Andrew Wig was born in Hawthorne, California on June 6, 1969. He attended private school at Trinity Lutheran School until grade 8 and then entered the public school system where he graduated from Hawthorne High School in 1989. The following August he entered North Park College in Chicago, Illinois where his love of volleyball quickly became an obsession. He had many wonderful experiences while in Chicago including meeting his future wife while on a mission trip to Ecuador. Upon graduating in 1991 from North Park College with a Bachelor of Science Degree in Physics he relocated to The University of Tennessee, Knoxville. After spending four years playing volleyball and occasionally studying he received his Master of Science Degree in Physics in December of 1995. After much thought and discussion he decided to continue on in the pursuit of his Doctorate in Physics at the University of Tennessee, Knoxville. Because of the intensity of the program and his increasing age his obsession with volleyball had now become a weekend hobby having left behind the innocence of his youth. It was with great pride, satisfaction, and relief that he received his doctoral degree in August 2000.